Universiteit Leiden
The Netherlands

Photothermal circular dichroism studies of single nanoparticles

Späth, P.R.

Citation

Späth, P. R. (2022, March 3). *Photothermal circular dichroism studies of single nanoparticles*. *Casimir PhD Series*. Retrieved from https://hdl.handle.net/1887/3278012

Version:	Publisher's Version
License:	Licence agreement concerning inclusion of doctoral thesis in the Institutional Repository of the University of Leiden
Downloaded from:	https://hdl.handle.net/1887/3278012

Note: To cite this publication please use the final published version (if applicable).

Photothermal Circular Dichroism Studies of Single Nanoparticles

Proefschrift

ter verkrijging van
de graad van doctor aan de Universiteit Leiden,
op gezag van rector magnificus prof. dr. ir. H. Bijl,
volgens besluit van het college voor promoties
te verdedigen op donderdag 3 maart 2022
klokke 10:00 uur

door

Patrick Späth

geboren te Aalen, Germany
in 1990

Promotores:
Prof. dr. M. A. G. J. Orrit
Prof. dr. M. W. Beijersbergen

Promotiecommissie:

Prof. dr. S. Bals	(Universiteit Antwerpen)
Prof. dr. L. Kuipers	(Technical University Delft)
Prof. dr. J. Aarts	
Prof. dr. J. M. van Ruitenbeek	
Dr. W. Löffler	

Universiteit Leiden
The Netherlands

Casimir research school

Nederlandse Organisatie voor Wetenschappelijk Onderzoek

Printed by: Gildeprint

Front & Back: Designed by Ms Pia Stoll

Copyright © 2022 by P. Späth

Casimir PhD Series, Delft-Leiden 2022-04

ISBN 978-90-8593-515-5

An electronic version of this dissertation is available at
`http://openaccess.leidenuniv.nl/`.

Some schematics of optical setups use components adapted from *ComponentLibrary* by Alexander Franzen, which is licensed under a CC BY-NC 3.0 Licence.

The present work is financially supported by the Netherlands Organization for Scientific Research and the Open Technology Program (TTW-OTP, Project No. 16008).

Für Nancy

"The strongest arguments prove nothing so long as the conclusions are not verified by experience. Experimental science is the queen of sciences and the goal of all speculation."
— ROGER BACON

Contents

1 Introduction **1**
1.1 Optical properties of gold nanoparticles . . . 2
1.2 Chirality . . . 2
1.2.1 Optical manifestation of chirality . . . 3
1.2.2 Linear dichroism and circular dichroism . . . 4
1.2.3 Magnetic circular dichroism . . . 4
1.3 Photothermal effect . . . 5
1.4 Outline of this thesis . . . 6
1.5 Contribution . . . 7
References . . . 7

2 Circular dichroism measurement of single metal nanoparticles using photothermal imaging **11**
2.1 Introduction . . . 12
2.2 Method . . . 13
2.3 Results and discussion . . . 16
2.4 Conclusion . . . 21
2.5 Supplementary information . . . 22
2.5.1 Details of the experimental setup . . . 22
2.5.2 Sample design and preparation . . . 22
2.5.3 Numerical simulations . . . 24
2.5.4 Measurement of linear dichroism on gammadions . . . 25
2.5.5 Characterization of nanospheres shape and size . . . 26
2.5.6 Does linear dichroism influence photothermal circular dichroism? . . . 27
2.5.7 More measurements of circular dichroism of gold nanospheres . . . 29
2.5.8 Line profiles of PT and PT CD signal of gold nanospheres . . . 30
2.5.9 Temperature increase due to absorption of the heating and probe beams . . . 31
References . . . 31

3 Photothermal circular dichroism of single nanoparticles rejecting linear dichroism by dual modulation **35**
3.1 Introduction . . . 36
3.2 Results and discussion . . . 39
3.2.1 Simulations . . . 39
3.2.2 Experimental results . . . 40

3.3 Conclusion . . . 46
3.4 Methods and experimental . . . 46
3.4.1 Experimental setup . . . 46
3.4.2 Data analysis . . . 47
3.5 Supplementary information . . . 47
3.5.1 Stokes representation of polarization . . . 47
3.5.2 Experimental alignment procedure . . . 47
3.5.3 Simulations . . . 53
3.5.4 CD of gold nanoparticle dimers . . . 58
3.5.5 CD of a single gold nanoparticle in carvone with LD reference . . . 58
3.5.6 Heat-induced reshaping . . . 59
3.5.7 Nanofabrication of single aluminium nanorods . . . 60
References . . . 60

4 Correlated optical and TEM measurements of quasi achiral and "superchiral" gold nanoparticles 65
4.1 Introduction . . . 66
4.2 Results and discussion . . . 67
4.2.1 Chiral nanorods . . . 67
4.2.2 Nominally achiral nanoparticles . . . 70
4.3 Conclusion . . . 73
4.4 Experimental . . . 73
4.4.1 Sample preparation . . . 73
4.4.2 g-factor analysis of optical measurements . . . 74
4.4.3 Transmission electron microscopy and tomography . . . 74
4.4.4 Quantification of asphericity . . . 74
4.4.5 Hausdorff chirality quantification . . . 74
4.4.6 Boundary element method simulations . . . 75
4.4.7 Quantification of helicity . . . 75
4.5 Supplementary information . . . 77
4.5.1 Ensemble CD spectra of the S-enantiomer of chiral nanorods . . . 77
4.5.2 Effect of defocusing on the CD g-factor . . . 77
References . . . 78

5 Magnetic circular dichroism of superparamagnetic nanoparticles 81
5.1 Introduction . . . 82
5.2 Results and discussion . . . 84
5.3 Conclusion and outlook . . . 87
5.4 Supplementary information . . . 88
5.4.1 Correlated SEM images of nominally 200 nm particles . . . 88
5.4.2 PT of 20 nm magnetite particles . . . 88
5.4.3 Calibration of magnetic field vs distance . . . 90
5.4.4 Magnetic-field-dependent PT-CD curves . . . 92
References . . . 93

6 Conclusion and outlook **97**

Samenvatting **101**

Curriculum Vitæ **103**

List of Publications **105**

Acknowledgements **107**

1

Introduction

The polarization of light has fascinated scientists for more than three centuries. Light polarization is utilized in many fields of science and has found various technical applications in the stress analysis of solids, ellipsometry, photography, display technology and polarized-light microscopy, just to name a few. Also in nature polarization effects are exploited, some animals have developed sophisticated polarization-sensitive eyesight making them able to see and communicate among channels others cannot and therefore puts them in advantage. From a historical perspective it was the study of optical activity, the difference in propagation speed between two perpendicular circular polarization states, that has led to a better understanding of the interaction of polarized light and matter. Circular dichroism (CD), the absorbtive manifestation of optical activity, is the differential absorption of an object with light of opposite handedness. In biochemistry it provides valuable information that cannot be extracted from ordinary absorption measurements alone and it is widely used in the study of the optical properties of crystals, along with linear birefringence and linear dichroism. In the realm of nano-optics and plasmonics, circular dichroism is of special interest as the shape affects the optical properties of a nano-object and it also affects its interaction with polarized light. Although highly sophisticated CD-sensitive techniques exist, they are, to date, mostly limited to measurements of ensembles of molecules or nanoparticles. Moreover, most CD techniques measure in transmission and therefore scattering is also playing a role when studying nanoparticles, in addition to absorption. The ensemble properties of such nanoparticles can often differ strongly from the single-particle properties, because in general the particles in an ensemble are not identical. In addition, when performing ensemble measurements one takes the average signal over all particle orientations. Therefore single-particle CD techniques are necessary to get a better understanding of the optical properties. In this work we investigate how photothermal imaging can be used to study the circular dichroism of individual (gold) nanoparticles and of superparamagnetic magnetite particles.

1.1. Optical properties of gold nanoparticles

Throughout this thesis we will mostly perform investigations on gold nanoparticles. Although other materials exhibit similar optical properties the choice often falls on gold due its chemical inertness. The optical properties of gold nanoparticles in the visible and near infrared can be well understood by the collective response of their quasi-free conduction electrons. An external electromagnetic plane wave with frequency ω causes the conduction electrons of a metal to oscillate. Their response is captured in the dielectric function $\epsilon(\omega) = \epsilon'(\omega) + i\epsilon''(\omega)$, which is related to the complex refractive index via $n^2 = \epsilon(\omega)$. Gustav Mie derived an analytical solution for the scattering problem of an electromagnetic wave incident on a spherical object. Mie's solution of Maxwell's equation is, in principle, valid for arbitrary sizes of the object. When dealing with small nanoparticles we often employ a dipolar approximation where we can neglect retardation effects. This holds true for particles much smaller than the wavelength. In this limit we can write the polarizability of a spherical nanoparticle as:

$$\alpha = 3V\frac{\epsilon - \epsilon_m}{\epsilon + 2\epsilon_m}, \tag{1.1}$$

where V is the particle's volume and ϵ and ϵ_m are the respective permeabilities of gold and of the surrounding medium [1]. The scattering and the absorption cross sections can be expressed as

$$\sigma_{sc} = \frac{k^4}{6\pi}|\alpha|^2 \quad and \quad \sigma_{abs} = k\,\mathrm{Im}(\alpha), \tag{1.2}$$

respectively [2], and $k = \omega n_m/c$ is the wavevector of the light in the surrounding medium. Equations 1.1 and 1.2 allow us to extract the most important optical properties of metal nanoparticles. Firstly, we find a resonance condition when the real part of $\epsilon + 2\epsilon_m$ approaches 0 - this is also known as plasmon resonance [3]. Another important quantity that can directly be extracted from equation 1.2, by invoking the optical theorem, is the extinction cross section, which writes: $\sigma_{ext} = \sigma_{abs} + \sigma_{sc}$. Furthermore, we find that the scattering term scales with the square of α whereas the extinction term scales linearly. This has important physical implications, namely, that at small sizes scattering can be neglected and the extinction becomes equivalent to the absorption, whereas for larger sizes the scattering term dominates. In a spherical nanoparticle we have three degenerate plasmon resonances due to the spherical symmetry. If the particle has other shapes e.g. a rod-like shape, one of these plasmon resonances is shifted to longer wavelengths [1, 4]. By tuning the length-to-diameter ratio of a nanorod one can tune its resonance. The resonance along the long axis is typically called *longitudinal plasmon* and the two-fold degenerate plasmon along the short axes is called *transverse plasmon*. Notably, the longitudinal plasmon can be shifted to far longer wavelength whereas the transverse plasmon usually does not shift much. One important implication of this lifted degeneracy is that the response of the nanorod not only depends on the size but also on the direction along we excite it and therefore on the polarization of light.

1.2. Chirality

Chirality - the absence of mirror symmetry of an object is a property found in a broad length scale ranging from nanosized objects like single molecules to macroscopic objects like our

hands. The basic building blocks of life are chiral and therefore the biochemistry that takes place in our bodies is strongly dependent on the specific interactions between those chiral objects and usually on their *handedness*. This strong interplay between form and function has led to a great importance of chirality in biochemistry. For drug molecules one particular handedness can be the cure while the other one is harmful [5]. CD has proven to be particularly useful in the study of the secondary structure of biomolecules [6–8]. However, chirality is not only relevant for chemical or biological considerations. Throughout this dissertation, in fact, we will mainly focus on the chirality of metal nanoparticles, which are usually much larger than most biomolecules. By the emergence of sophisticated chemical synthesis and nanofabrication methods, chiral nano-sized particles and structures can now be crafted with various unique optical properties which are related to their chiral geometry [7, 9–13].

1.2.1. Optical manifestation of chirality

The handedness of a chiral object affects how it interacts with other chiral objects. When we shake hands for example we will immediately know whether we shake a left or a right hand, likewise a right-handed screw requires opposite turning than a left-handed one to drive it into wood. On the nanoscale such distinctions turn out to be more difficult. Although modern microscopy methods such as AFM imaging or electron microscopy have superb spatial resolution, so far they have limited application for the study of chiral nanoparticles (with some exceptions [9, 14]). Far-field optical microscopy is limited by diffraction to $\sim 200\,\mathrm{nm}$ (depending on the wavelength) and therefore cannot resolve the geometry of a nanoparticle, and yet it can discriminate the two enantiomers of chiral nanoparticles or even enantiopure ensembles of molecules. Polarized light can be chiral - with left and right circularly polarized light being of opposite handedness. Chiral objects have an important quality, they interact differently with light of opposite handedness [15]. This property is called circular dichroism for absorption and circular birefringence for retardation (complex and real part of the polarizability) and can be exploited to discriminate and study chiral objects.[1] In general for an object to exhibit circular dichroism it requires two ingredients. First, it requires a geometry that breaks mirror symmetry, a simple example would be a helix, and second, the object's size should be large enough compared to the wavelength of light so that retardation effects become relevant. The reason why many biomolecules often exhibit weak CD in the visible range, is because their "helical pitch" is much smaller than the pitch of the electric field of circularly polarized light [15].

A typical circular dichroism spectrometer is based on a transmission geometry and probes the differential extinction, containing an absorption and a scattering contribution, of left and right handed circularly polarized light of an analyte. When light of opposite handedness is transmitted through a cuvette containing a chiral analyte and if the analyte absorbs or scatters at the light wavelength, its transmission will depend on the handedness of polarization. Small changes in transmission can be translated into differential extinction, which can be detected with high accuracy via lock-in amplification. Modern spectropolarimeters are based on the design developed by Jellison [16] and can measure differences in extinction down to 10^{-5} [8, 17], however, this accuracy can only be achieved in an en-

[1] Circular birefringence is considered less often although it carries the same physical information as it is linked to circular dichroism via a Kramers-Kroning relationship [5].

semble measurement, thereby averaging the response of many molecules or particles.

1.2.2. Linear dichroism and circular dichroism

We have just established that CD is the difference of absorption between left and right circularly polarized light. CD appears when an object has a broken symmetry (lack of mirror symmetry) and requires a true 3D spatial arrangement. A related effect to CD is linear dichroism (LD), the difference in absorption of two orthogonal *linear* polarization states. We have discussed in paragraph 1.1 that a nanorod's resonance wavelength depends on the axis we excite it at. If we compare the nanorod's absorption with linearly polarized light at the longitudinal plasmon resonance wavelength, we find a strong absorption along the long axis but weak absorption along the short axis. The two different plasmon conditions lead to LD. However, if we perform the same measurement in a 45° rotated axis, for example, we find zero difference in absorption, as in both cases the driving field causes the same excitation in the nanorod.

Although throughout this thesis we are mainly interested in the measurement of the CD of a given object, we must also take into account its LD, for the simple reason that a real measurement never is perfect. An ideal way to measure CD is to measure the differential absorption of two orthogonal circular polarization states by performing a square-wave modulation of the polarization. In a real experiment such a square-wave modulation is not feasible and therefore elliptic polarization states will be involved that can give rise to leakage of an LD signal into the CD signal.

LD is often magnitudes stronger than CD and therefore, when not carefully subtracting LD components from our CD signal, we might draw the wrong conclusions. In chapter 3 we will see in detail how to subtract LD components to leak into the CD signal.

1.2.3. Magnetic circular dichroism

In 1846 Michael Faraday discovered that heavy glass, when subject to a strong magnetic field, can rotate the plane of polarization of linearly polarized light [18]. This effect, also known as Faraday rotation, showed the interaction of light with (electro) magnetic fields inside matter. Shortly after Faraday, John Kerr found, by reflecting polarized light from a polished and strongly magnetized iron surface, that the plane of polarization of the reflected beam was rotated with respect to that of the incoming beam [19]. Faraday's and Kerr's experiments have marked the advent of magneto-optics which is still a vivid field of research and led to important technological developments as for example magnetic data storage or optical isolators (Faraday rotator). Both experiments measured a birefringence effect, which is related to the real part of the refractive index. The absorptive counterpart of this effect is called magnetic circular dichroism (MCD). Magnetic circular dichroism, like geometric circular dichroism (circular dichroism due to a lack of mirror symmetry) is the difference of absorption of left and right circularly polarized light. The most important difference between geometric CD (chirality) and MCD is that the former requires geometric features in a spatial arrangement that have helical handedness. In contrast, MCD can be found in all (magnetic) matter, independently of the spatial arrangement as long as a net magnetization is present [20]. It results from a magnetic perturbation of the electronic states involved in

optical transitions in absorption bands [21]. In the case if the magneto-optic Kerr effect it is the interplay of magnetic moments and spin-orbit coupling that leads to a differential absorption of left and right circularly polarizer light [22]. A detailed mathematical treatment of the effect is presented in the works of Oppeneer [23] and Argyres [24].

1.3. Photothermal effect

We have introduced circular dichroism as an optically measurable quantity of chirality. We have also seen that CD is typically probed in a transmission geometry where a cuvette contains a solution of the sample of interest. Measurements in a transmission geometry probe extinction and therefore entail not only an absorption but also a scattering contribution of the sample. Although the scattering component can be often neglected, when for example studying molecules (due to their small size), if one wants to study the circular dichroism of objects such as plasmonic nanoparticles, one can no longer neglect the scattering contributions to the CD signal [6, 25]. The study of the "true" circular dichroism of such particles therefore requires an optical technique that is only sensitive to absorption. Additionally, ensemble measurements averages the CD signal over all possible particle orientations, whereas single particle measurements measures the CD of a single orientation. In this section we introduce photothermal microscopy as an optical technique that is exclusively sensitive to absorption and therefore is well-suited to study the circular dichroism of individual nanoparticles.

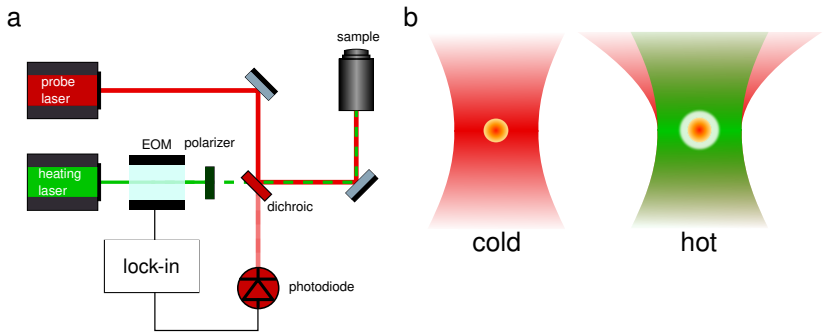

Figure 1.1: (a) Schematic photothermal setup in a reflective geometry. A red probe laser is combined with a green heating laser by means of a dichroic element. The dichroic also serves to filter out the green light on the detection path. The intensity of the heating laser is modulated via a combination of EOM and polarizer. (b) Photothermal effect of a nanoparticle immersed in a liquid. When a heating beam heats the particle a thermal lens forms that changes the probe beam's propagation. This causes a small difference in light collection. Those small differences can be detected by means of lock-in amplification with high sensitivity. The deviation of the probe beam upon thermal lens formation is exaggerated.

We have established in section 1.1 that small gold nanoparticles strongly absorb light. The absorbed energy decays mostly nonradiatively and, as a consequence, heat is produced. The heat is subsequently released into the surrounding environment, thereby changing its refractive index close to the particle. We call this local refractive index gradient a *thermal lens* [26]. The thermal lens can be probed by a second laser, that we shall name probe beam and whose wavelength is chosen far away from the absorption resonance of the particle to prevent further heating. In PT microscopy we measure the change in scattering of the *probe*

beam upon the formation of a thermal lens $\partial\sigma_{sc}/\partial P_{heat}$ that is created by the absorption of a *heating beam*. Therefore, we separate the residual heating photons from the collected probe photons by means of a long pass filter. In first approximation and for small particles, the change of collected probe photons upon heating depends linearly on the thermorefractive coefficient $\partial n/\partial T$ [27] of the surrounding medium. In general, the effect of the thermal lens is quite small as the heat-induced refractive index change is typically on the order of 10^{-4}/K for most liquids [28]. To make up for this small change, in PT imaging we do not employ a CW heating scheme, but we modulate the heating beam intensity, typically at frequencies between $50\,\mathrm{kHz}$ and $1\,\mathrm{MHz}$. This leads to a periodic variation of the thermal lens at the modulation frequency. If we employ lock-in amplification, we can extract the signal at that heating beam modulation frequency, thereby removing most of the 1/*f* noise and achieve shot-noise-limited detection [29]. A simple version of such a PT setup, in a reflection geometry, is depicted in figure 1.1(a). The heating beam is intensity-modulated by a electro-optic modulator and a subsequent polarizer. The probe beam and the heating beam are combined by a dichroic mirror and sent to the objective. A gold particle is residing close to the focus of the probe beam. When the particle is illuminated by the heating beam, heat is created and a thermal lens forms which affects the probe beam propagation and therefore the probe beam collection. The collected probe beam is separated from the heating beam by a dichroic mirror (or long pass filter) and sent to a photodiode. A lock-in amplifier referenced to the driving frequency of the EOM extracts the minute changes of the scattered probe beam. The choice of the probe wavelength far away from the absorption resonance allows for using large probe powers and accordingly for lowering photon noise. When measuring the absorption of gold nanoparticles we typically use $532\,\mathrm{nm}$ for the heating beam, as it is close to the plasmon resonance of gold nanoparticles [30], and a probe beam far enough red-shifted to neglect absorption effects (typically $\sim$780 nm). This leads to a very low background and allows for detecting gold particles down to $1.4\,\mathrm{nm}$ in size [31] or even single molecules [32]. The strength of PT imaging for studying circular dichroism is that, in first approximation, it depends on the absorbed heating beam causing a temperature gradient and therefore is only sensitive to absorption. We will see in chapter 2 how we can exploit photothermal microscopy, combined with polarization modulation, to study and measure circular dichroism.

1.4. Outline of this thesis

The first two chapters of this thesis (chapters 2 and 3), focus on the development of a technique that is sensitive to differential absorption of light of opposite handedness. The technique has been developed in two steps.

In **chapter 2** we examine how PT microscopy paired with polarization modulation can be employed to perform diffraction-limited circular dichroism measurements at the single-particle level. We discuss how to build a setup geometry in reflective mode and how to avoid polarization artefacts induced by optical components and strongly focused light.

Chapter 3 presents a refined version of the technique introduced in chapter 2; we further discuss artefacts inherent to the technique and how dual modulation of polarization is a viable remedy. Furthermore we show that we can measure all absorptive properties of a nanoparticle and that the technique can be extended to perform spectral analysis.

In **chapter 4** we investigate, by correlated TEM and optical absorption imaging, on geometric features responsible for the circular dichroism of two nanoparticle systems. We investigated quasi achiral spherical nanoparticles and tailor-made "superchiral" plasmonic nanoparticles.

Finally, we will see in **chapter 5** that circular dichroism does not necessarily requires chiral geometry as soon as magnetic moments are involved. By studying superparamagnetic magnetite particles under a variable external magnetic field we show that PT CD can be used to study the magnetic moments of nanoparticles.

1.5. Contribution

Part of the experimental work and data analysis, shown in this manuscript, has been obtained in collaboration with colleagues in Leiden and research groups in Delft and Antwerpen. Therefore it is befitting to clarify the author's contribution to each chapter: In **chapter 2** the author designed and built the setup and performed the optical measurements. The measurements, simulations and data analysis in **chapter 3** have been entirely performed by the author, with exception of the measurements in figure S3.7 and figure S3.5. In **chapter 4** the author has performed the optical measurements. In **chapter 5** the measurements and data analysis have been entirely done by the author, with exception of the measurements in figure S5.2 and figure S5.1.

References

[1] Myroshnychenko, V.; Rodriguez-Fernandez, J.; Pastoriza-Santos, I.; Funston, A. M.; Novo, C.; Mulvaney, P.; Liz-Marzan, L. M.; De Abajo, F. J. G. Modelling the Optical Response of Gold Nanoparticles. *Chemical Society Reviews* **2008**, *37*, 1792–1805.

[2] Bohren, C.; Huffman, D. R. *Absorption and Scattering of Light by Small Particles*; Wiley Science Paperback Series: New Jersey, 1998.

[3] Ritchie, R. H. Plasma Losses by Dast Wlectrons in Thin Films. *Physical review* **1957**, *106*, 874.

[4] Kreibig, U.; Vollmer, M. *Optical Properties of Metal Clusters*; Springer Science & Business Media, 2013; Vol. 25.

[5] Fasman, G. D. *Circular Dichroism and the Conformational Analysis of Biomolecules*; Springer, Boston, MA, 1996; Vol. 1.

[6] Bustamante, C.; Tinoco, I.; Maestre, M. F. Circular Differential Scattering can be an Important Part of the Circular Dichroism of Macromolecules. *Proceedings of the National Academy of Sciences* **1983**, *80*, 3568–3572.

[7] Micsonai, A.; Wien, F.; Kernya, L.; Lee, Y.-H.; Goto, Y.; Réfrégiers, M.; Kardos, J. Accurate Secondary Structure Prediction and Fold Recognition for Circular Dichroism Spectroscopy. *Proceedings of the National Academy of Sciences* **2015**, *112*, E3095–E3103.

[8] Freedman, T. B.; Cao, X.; Dukor, R. K.; Nafie, L. A. Absolute Configuration Determination of Chiral Molecules in the Solution State Using Vibrational Circular Dichroism. *Chirality* **2003**, *15*, 743–758.

[9] González-Rubio, G.; Mosquera, J.; Kumar, V.; Pedrazo-Tardajos, A.; Llombart, P.; Solís, D. M.; Lobato, I.; Noya, E. G.; Guerrero-Martínez, A.; Taboada, J. M., et al. Micelle-directed Chiral Seeded Growth on Anisotropic Gold Nanocrystals. *Science* **2020**, *368*, 1472–1477.

[10] Arteaga, O.; Sancho-Parramon, J.; Nichols, S.; Maoz, B. M.; Canillas, A.; Bosch, S.; Markovich, G.; Kahr, B. Relation Between 2D/3D Chirality and the Appearance of Chiroptical Effects in Real Nanostructures. *Optics express* **2016**, *24*, 2242–2252.

[11] Vinegrad, E.; Vestler, D.; Ben-Moshe, A.; Barnea, A. R.; Markovich, G.; Cheshnovsky, O. Circular Dichroism of Single Particles. *ACS Photonics* **2018**, *5*, 2151–2159.

[12] Kosters, D.; De Hoogh, A.; Zeijlemaker, H.; Acar, H.; Rotenberg, N.; Kuipers, L. Core–Shell Plasmonic Nanohelices. *ACS Photonics* **2017**, *4*, 1858–1863.

[13] Coles, R.; Price, D.; Dixon, J.; Royall, B.; Clarke, E.; Kok, P.; Skolnick, M.; Fox, A.; Makhonin, M. Chirality of Nanophotonic Waveguide with Wmbedded Quantum Emitter for Unidirectional Spin Transfer. *Nature Communications* **2016**, *7*, 1–7.

[14] Zhao, Y.; Saleh, A. A.; Van De Haar, M. A.; Baum, B.; Briggs, J. A.; Lay, A.; Reyes-Becerra, O. A.; Dionne, J. A. Nanoscopic Control and Quantification of Enantioselective Optical Forces. *Nature nanotechnology* **2017**, *12*, 1055–1059.

[15] Tang, Y.; Cohen, A. E. Optical Chirality and its Interaction with Matter. *Physical Review Letters* **2010**, *104*, 163901.

[16] Jellison, G. E.; Griffiths, C. O.; Holcomb, D. E.; Rouleau, C. M. Transmission Two-Modulator Generalized Ellipsometry Measurements. *Appl. Opt.* **2002**, *41*, 6555–6566.

[17] Nafie, L. A.; Keiderling, T.; Stephens, P. Vibrational Circular Dichroism. *Journal of the American Chemical Society* **1976**, *98*, 2715–2723.

[18] Faraday, M. *Experimental Researches in Electricity*; Dover Publications: Mineola, N.Y, 2004.

[19] Kerr, J. L. XL. A New Relation Between Electricity and Light: Dielectrified Media Birefringent. *The London Philosophical Magazine and Journal of Science* **1875**, *50*, 337–348.

[20] Mason, W. *A Practical Guide to Magnetic Circular Dichroism Spectroscopy*; Wiley-Interscience: Hoboken, N.J, 2007.

[21] Pershan, P. Magneto-Optical Effects. *Journal of Applied Physics* **1967**, *38*, 1482–1490.

[22] Coey, J. M. D. *Magnetism and Magnetic Materials*; Cambridge University Press: Cambridge, 2010; Chapter 5.

[23] Oppeneer, P. M. Theory of the Magneto-Optical Kerr Effect in Ferromagnetic Compounds. Habilitation, Technische Universität Dresden.

[24] Argyres, P. N. Theory of the Faraday and Kerr Effects in Ferromagnetics. *Physical Review* **1955**, *97*, 334.

[25] Wang, L.-Y.; Smith, K. W.; Dominguez-Medina, S.; Moody, N.; Olson, J. M.; Zhang, H.; Chang, W.-S.; Kotov, N.; Link, S. Circular Differential Scattering of Single Chiral Self-Assembled Gold Nanorod Dimers. *ACS Photonics* **2015**, *2*, 1602–1610.

[26] Uchiyama, K.; Hibara, A.; Kimura, H.; Sawada, T.; Kitamori, T. Thermal Lens Microscope. *Japanese Journal of Applied Physics* **2000**, *39*, 5316.

[27] Selmke, M. Photothermal Single Particle Detection in Theory & Experiments. Ph.D. thesis, Universität Leipzig, 2013.

[28] Bialkowski, S. Parameters for Common Solvents Used in Photothermal and Photoacoustic Spectrometry. 2021; `http://ion.chem.usu.edu/~sbialkow/book.html`.

[29] Gaiduk, A.; Ruijgrok, P. V.; Yorulmaz, M.; Orrit, M. Detection Limits in Photothermal Microscopy. *Chemical Science* **2010**, *1*, 343–350.

[30] Baffou, G. *Thermoplasmonics : Heating Metal Nanoparticles Using Light*; Cambridge University Press: Cambridge, 2018.

[31] van Dijk, M. A.; Tchebotareva, A. L.; Orrit, M.; Lippitz, M.; Berciaud, S.; Lasne, D.; Cognet, L.; Lounis, B. Absorption and Scattering Microscopy of Single Metal Nanoparticles. *Physical Chemistry Chemical Physics* **2006**, *8*, 3486–3495.

[32] Gaiduk, A.; Yorulmaz, M.; Ruijgrok, P.; Orrit, M. Room-temperature Detection of a Single Molecule's Absorption by Photothermal Contrast. *Science* **2010**, *330*, 353–356.

2

Circular dichroism measurement of single metal nanoparticles using photothermal imaging

Circular dichroism (CD) spectroscopy is a powerful optical technique for the study of chiral materials and molecules. It gives access to an enantioselective signal based on the differential absorption of right and left circularly polarized light, usually obtained through polarization analysis of the light transmitted through a sample of interest. CD is routinely used to determine the secondary structure of proteins and their conformational state. However, CD signals are weak, limiting the use of this powerful technique to ensembles of many molecules. Here, we experimentally realize the concept of photothermal circular dichroism, a technique that combines the enantioselective signal from circular dichroism with the high sensitivity of photothermal microscopy, achieving a superior signal-to-noise ratio to detect chiral nano-objects. As a proof of principle, we studied the chiral response of single plasmonic nanostructures with CD in the visible range, demonstrating a signal-to-noise ratio better than 40 with only $30\,\mathrm{ms}$ *integration time for these nanostructures. The high signal-to-noise ratio allows us to quantify the CD signal for individual nanoparticles. We show that we can distinguish relative absorption differences for right circularly and left circularly polarized light as small as* $g_{min} = 4 \times 10^{-3}$ *for a* $30\,\mathrm{ms}$ *integration time with our current experimental settings. The enhanced sensitivity of our technique extends CD studies to individual nano-objects and opens CD spectroscopy to numbers of molecules much lower than those in conventional experiments.*

This chapter is based on the publication in Nano Letters **19**, 12 (2019).

2.1. Introduction

An object is chiral when its mirror image cannot be superimposed with the original object [1, 2]. The most prominent examples of chirality are found at all scales in life, from whole organisms to biomolecules such as DNA, most sugars as well as amino-acids, which often occur only in one handedness [3, 4]. Chirality at the molecular level arises from the relative spatial arrangement of the constituent atoms in a molecule; the two mirror-symmetric isomers of a chiral molecule are called enantiomers. Despite their identical chemical composition, enantiomers can have dramatically different biological activities, metabolism rates and toxicities [5]. Therefore, methods for detecting molecular chirality and separating enantiomers are highly relevant for drug development. The standard optical technique to study chirality of biomolecules and biomacromolecules is circular dichroism (CD) spectroscopy [5–7], which gives access to the handedness of a molecule and also provides insight into the secondary structure and the conformational state of proteins [8, 9]. Circular dichroism measurements amount to detecting the differential absorption cross section of the object under study for left and right circularly polarized light,

$$\Delta\sigma = \sigma_L - \sigma_R, \tag{2.1}$$

where σ_L, σ_R represent the absorption cross sections for LCP and RCP, respectively. The dissymmetry factor g, defined as

$$g = 2\frac{\sigma_L - \sigma_R}{\sigma_L + \sigma_R}\,, \tag{2.2}$$

gives a measure of the differential circular absorption cross section normalized by the average absorption cross section. Equation 2.1 together with basic symmetry arguments shows that the mirror image of a chiral object presents the same absolute CD signal with the opposite sign. CD measurement as a function of light wavelength gives rise to a CD spectrum. Note that, even though the cross sections for right and left circularly polarized light may be large, the difference is generally very small for molecules, i.e., typically $g \leq 10^{-3}$ [5]. Therefore, CD studies on molecules are carried out by measuring the signal from a large number of molecules in ensemble-averaged experiments [9]. Because of the broad applicability of CD spectroscopy in biochemistry, it is highly desirable to improve its sensitivity, so as to analyse much smaller numbers of molecules, thereby reducing the amounts needed for chirality studies of newly synthesized compounds or for monitoring the conformational states of proteins.

To the chemist, chirality is a property of 3D objects which survives averaging over the random orientations of a macroscopic solution, as happens for chiral molecules. In microscopy or nanophotonics, however, we often deal with surfaces and nanostructures [10, 11] written by nano-lithography. Although they may be chiral in 2D (i.e., such a structure does not coincide with its 2D image in a reflection with respect to a line in its plane), they are not necessarily chiral in 3D because, at least in first approximation, they obviously present reflection symmetry in their own plane. In this case, dissymmetry in absorption of LCP and RCP light can arise from many different sources. The sample material itself can be chiral, either because of its structure, or because of defects induced by the fabrication process. The 2D-chiral shape of the structures, while not a source of 3D-chirality by itself, can combine

with front-back asymmetry to produce 3D-chirality. As discussed by Arteaga et al. [12], mirror symmetry of a 2D-chiral structure can be broken by the different refractive indices on either side of the interface, by inevitable surface roughness in sputtered or evaporated structures, or by the illumination process itself, as incident light usually comes from only one side of the sample. We use the term circular dichroism in this work, irrespective of the origin of the observed dissymmetry. Here, we present our experimental approach to image circular dichroism of single nanostructures, based on the differential detection of absorption by the photothermal effect rather than by the conventional extinction method, thus obtaining a photothermal circular dichroism (PT CD) image. Therefore, the plasmonic nanostructures in the present work are models of CD-active objects and are not used to enhance optical chirality signals, as proposed and realized by other groups [13, 14]. A similar approach, based on thermal lens spectroscopy, was used on solutions by Kitamori's group [15], and very recently has been proposed theoretically for the study of chiral nanoparticles [16]. The photothermal version of circular dichroism achieves an improved sensitivity in the detection of individual chiral nanostructures, as shown below, while relaxing experimental requirements needed for polarization control on the experimental setup.

2.2. Method

Figure 2.1 shows a conceptual scheme of the technique. For clarity we show the scheme for normal photothermal microscopy on the left-hand side and for PT CD on the right-hand side. We illuminate the sample with a heating beam (represented in green/dark green in the figure) that is absorbed by the nano-object under study, for example, a (2D) chiral plasmonic nanostructure, here represented as a left hand. We periodically modulate the polarization state of this heating beam between LCP and RCP at a frequency f_m (figure 2.1 (b)). As the chiral object presents different absorption cross sections for each handedness, the amount of absorbed energy differs for LCP and RCP light. The absorbed energy released as heat through non-radiative channels will thus increase the temperature of the nanostructure and create a non-uniform temperature distribution in the surrounding medium that will have slightly different amplitudes for LCP and RCP, as illustrated in figure 2.1 (b,f). This local temperature increase creates a time- and space-dependent change in the refractive index $\Delta n(\vec{r}, t)$ through the thermorefractive coefficient $\partial n/\partial T$ [17–19] of the surrounding medium [1], which is often called a thermal lens [20]. A second beam, the probe (represented in red in figure 2.1 (a) and (b)), is used to detect the strength of the thermal lens through interference between the reflection at the substrate-medium interface and the light back-scattered by the thermal lens [18]. The small difference in back-scattered light is detected by a lock-in amplifier at the polarization modulation frequency f_m. As the only difference upon modulation is the circular polarization state, the amplified signal will be proportional to the difference between LCP and RCP absorption, which is exactly the circular dichroism signal we seek. Non-chiral particles, having no difference in circular absorption cross sections, will not give rise to any PT CD signal.

Photothermal circular dichroism builds on the well established photothermal microscopy

[1] In the case of large metallic nanostructures, the temperature increase can modify the structure's optical response, for example by shifting its plasmon resonance. Therefore, large structures themselves can significantly contribute to the photothermal signal.

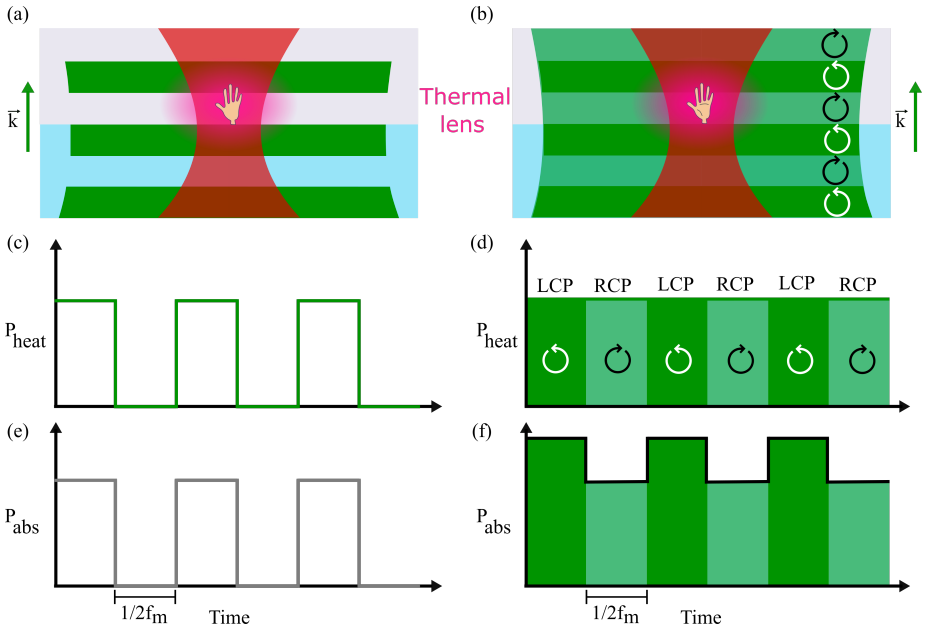

Figure 2.1: **Photothermal and photothermal circular dichroism concept**. (a) Scheme of the wide-field-heating photothermal detection of a chiral structure (illustrated as a hand) on a glass substrate. The heating beam is wide (green) and the probe beam (red) is focused to the diffraction limit. The heating beam intensity is modulated between on and off states at a frequency f_m. Part of the absorbed power will be released as heat to the environment, creating a thermal lens (in purple) around the absorbing object. The wavevector direction ($\vec{k}$) for both beams is shown. (b) Scheme for photothermal circular dichroism (PT CD), where we modulate the polarization state of the heating beam between left and right circularly polarized light (dark and light green, respectively). The thermal lens is also created in this case (in purple). The wavevector direction ($\vec{k}$) for both beams is shown on the right. (c) Time evolution of the heating power for the intensity-modulated photothermal microscopy, following the intensity modulation pattern at f_m. (d) Time evolution of the heating power for the polarization-modulated photothermal microscopy. In this case the heating power is *constant* and the only change is the polarization state. (e) Time evolution of the absorbed power by the nanostructure under study for the intensity-modulated photothermal case. Naturally, when the heating power is zero, the absorbed power is null. (f) Time evolution of the absorbed power by the nanostructure under study for the polarization-modulated photothermal case. Since it is a chiral structure, the absorbed powers for LCP and RCP are different.

to detect absorbing nanoscale objects such as plasmonic nanoparticles [17, 20–22], single conjugated polymer molecules [23] and even single small absorbing molecules at room temperature [24], and combines it with the enantioselective signal provided by circular dichroism.

Experimental setup. Sensing circular dichroism requires precise control of the polarization state. For that reason, great care must be taken with the illumination scheme and the choice of optical components. We implemented the concept of photothermal circular dichroism on a home-made optical microscope using a wide-field heating beam at a wavelength of $532\,\mathrm{nm}$ and a tightly focused probe beam at $780\,\mathrm{nm}$. In this way, we still obtain diffraction-limited spatial resolution through the tightly focused probe beam, whereas the polarization of the heating beam is easily controlled thanks to its low numerical aperture

($NA \sim 0.025$, corresponding to a spot diameter of $10\,\mu\mathrm{m}$).

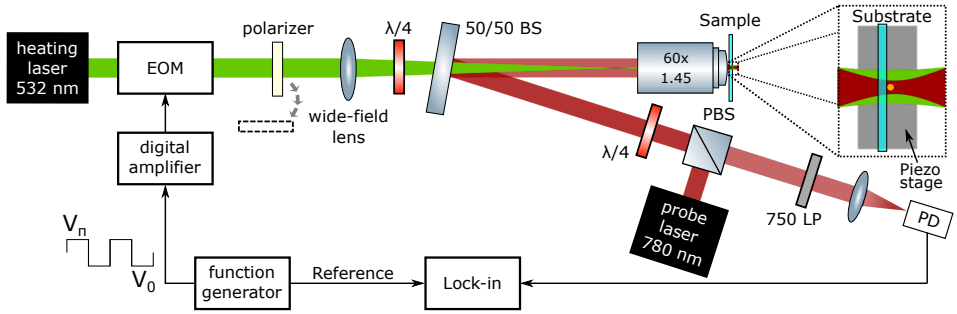

Figure 2.2: **Photothermal circular dichroism setup**. Implementation of the PT CD microscope using a $532\,\mathrm{nm}$-wide-field heating beam and a tightly focused probe beam at $780\,\mathrm{nm}$. The polarization modulation is achieved using an electro-optical modulator (EOM), leading to an alternatingly vertical and horizontal linear polarization state (the EOM acts as a zero and half-wave plate at 45 degrees with respect to the incoming polarization). A quarter-wave plate ($\lambda/4$) transforms these states into LCP and RCP light. The removable polarizer is added to achieve intensity modulation, i.e. conventional photothermal imaging. The wide-field lens focuses the heating beam in the back-focal plane of the objective to obtain wide-field illumination of the sample. The probe beam from a Ti:Sapphire laser is combined with the heating beam using a 50/50 beam splitter tilted by a small angle ($5°$). The detector (PD) is a fast photodiode with variable amplification. A long-pass filter (750LP) prevents direct detection of the heating beam. The generated signal is filtered by the lock-in amplifier set to the modulation frequency f_m created in the function generator and amplified to feed the EOM.

Figure 2.2 depicts a schematic representation of the microscope. The wide-field heating ensures a high-quality circular polarization state reaching the sample. This configuration is also less sensitive to possible lateral shifts in the heating beam due to mechanical drifts, thus improving stability. The heating and probe beams are combined via a non-polarizing beam splitter that is placed at a small angle (about $5°$) with respect to the heating beam to minimize the incidence angle's effect on the polarization state of the heating beam. We implemented a backward-detection for photothermal imaging, where the backscattered probe beam is sent to a fast photodetector (PD), and we suppressed noise efficiently with a lock-in amplifier. We used the an optical configuration, consisting of a polarization beam splitter and a quarter-wave plate to maximize the collection of photons scattered at the thermal lens [19]. We want to emphasize here that, despite the wide-field illumination of the heating beam, this technique is still confocal since the probe beam is focused tightly on the sample. To obtain an image, we scan the sample with a translation stage while the overlap of the two beams remains constant.

To implement photothermal circular dichroism, we need to modulate the heating beam's polarization between RCP and LCP. To this end, we use an electro-optical modulator (EOM) to rotate the incoming linear horizontal polarization by 90 degrees, at frequencies $\sim 100\,\mathrm{kHz}$. We set the EOM principal axis at 45 degrees with respect to the horizontal and we apply a square modulation of the EOM voltage between the zero-wave plate (V_0) and half-waveplate (V_π) values. Thus, after the EOM we have an alternating vertical (V) - horizontal (H) polarization state. Down the beam path, we use a quarter-wave plate with its axis at 45 degrees to transform these two orthogonal linear states into LCP and RCP, respectively. Additionally, we can add a linear polarizer directly after the EOM to perform conventional, intensity-

modulated photothermal imaging. More details about the experimental setup can be found in the Supporting Information of this chapter.

2.3. Results and discussion

As a model system for photothermal circular dichroism on single particles we prepared a sample containing 2D nano-structures of either handedness, presenting circular dichroism resonances in the visible range. The sample consists of an array of 2D-chiral gold nanostructures on a glass substrate in the form of gammadions, which present a strong chiral response in the visible due to the presence of plasmonic resonances [25, 26]. These structures are convenient to test circular dichroism measurements because their fourfold symmetry (C_4) implies that the linear dichroism ideally vanishes, provided the axis of rotational symmetry is oriented along the optical axis (as is the case presented here). Additionally, they can be easily fabricated in (2D) right- and left-handed versions. Note again that the design is based on the two-dimensional chiral character of the gammadions and that several effects can contribute to the circular dichroism signal, as discussed above [12, 27]. As an extra check, we also fabricated achiral structures with a similar shape.

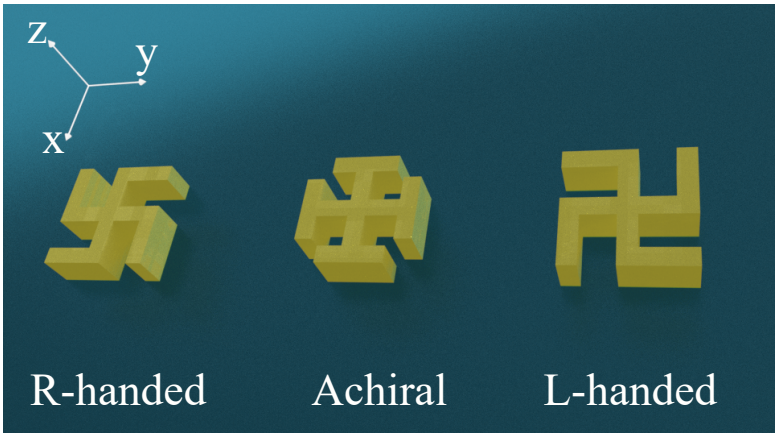

Figure 2.3: **Handedness of gammadions**. Definition of the L- and R-handed structures based on their geometrical shape. The structures are supported by a glass substrate. We also show the coordinate system used for clarity.

We name our structures based on the geometrical properties: we call a gammadion "right-handed" if its arms point clockwise and "left-handed" if they point counter-clockwise, when we look at them from the top, which is defined such that the structures sit on top of the glass substrate. In figure 2.3 we show a scheme of the structures on the glass substrate, seen from the air side (above). This is a perspective view from the same side as used for the SEM images (see figure 2.4 (a) and (b)), but note that in the optical measurements we illuminate the structures from the bottom (from the glass substrate). For the wavelengths and structures used in this experiment, the left-handed enantiomer leads to a positive CD signal, as shown in figure 2.1[2].

[2]It is also important to note the convention used to define our polarization state. We follow the convention used

We fabricated an array of alternating right-handed, achiral and left-handed structures, as shown in the scanning electron microscopy images in figure 2.4 (a) and (b). In the Supporting Information we provide more details about the geometrical design of each type of structure and their locations in the array. With this array, we can measure the three types of structures in the same optical image and thus in the same experimental conditions. We embedded the structures in toluene to have a strong photothermal response (thanks to the high thermorefractive coefficient of toluene).

Figures 2.4 (c), (d) show conventional photothermal images of the whole array of structures under intensity modulation of the heating beam (c) and a higher-resolution image of the bottom right part of the array, (d). The intensity in these images is normalized to both the heating and pump intensities, deduced from powers and beam areas (A_h $78\,\mu\mathrm{m}^2$ and A_p $\sim 0.196\,\mu\mathrm{m}^2$, respectively), to allow for comparison of images recorded under different conditions. Photothermal images taken with circularly polarized light show different intensities from different structures due to the two different absorption cross sections of the three type of structures, chiral (right- or left-handed) or achiral, at the heating wavelength $532\,\mathrm{nm}$. Figures 2.4 (e) and (f) depict the photothermal circular dichroism images of the same areas as (c) and (d), where we clearly observe contrast for the right- and left-handed structures, with opposite signs, and hardly any signal from the achiral structures, demonstrating the desired enantioselectivity of the technique. We note that the signal-to-noise ratio (SNR) for the PT CD images is excellent, in the order of 40 with only $30\,\mathrm{ms}$ integration time in the lock-in amplifier and with moderate intensities used for imaging. For example, when we take the signal of the top left structure of figure 2.4 (f) and we average the pixels corresponding to the size of the point-spread function we obtain a signal $S_{stru} = -(1.53 \pm 0.01)10^{-2}\ \mathrm{mV\,mW^{-2}}$, while the standard deviation with the same number of pixels outside any structure gives $N = (3.8 \pm 0.1)10^{-4}\ \mathrm{mV\,mW^{-2}}$, so the signal-to-noise ratio for this specific structure is $S_{stru}/N = SNR \sim 45$. We note that the value for the noise mentioned above is similar to the value we measured when we turned off the heating laser and performed an image only with the probe laser. This is a significant improvement in sensitivity for detecting circular dichroism of individual chiral nanostructures with respect to the extinction-based detection schemes, in which a $SNR \sim 10$ is typically obtained when using a $1\,\mathrm{s}$ integration time on the resonance of similar gold nanostructures [26].

It is important to note that the imaging conditions for this sample are not optimized. First, the heating beam at $532\,\mathrm{nm}$ is not in resonance with the strongest CD resonance of the structure in the visible range, located at $\sim 700\,\mathrm{nm}$ according to our numerical simulations. Second, due to the non-negligible absorption at that wavelength, the probe laser intensity at $780\,\mathrm{nm}$ had to be kept low ($I_p = 0.76$ mW/$\mu\mathrm{m}^2$) to avoid boiling the surrounding liquid, and reshaping of the structures at still higher powers. For the numerically calculated absorption spectra and g-factor, please refer to the Supporting Information. The photothermal circular dichroism images in figure 2.4 (e) and (f) are proportional to the numerator of the dissymmetry factor g (defined in equation 2.2), while the photothermal images (c) and (d) are proportional to σ_L, since we used an intensity-modulated heating beam with left circular polarization to take those photothermal images. Thus, we can use the signals from

by Jackson [28], where an observer facing the incoming plane wave with left circularly polarized state sees a counter-clockwise rotation. This corresponds to the tip of the electric field vector tracing out a left-handed helix (positive helicity).

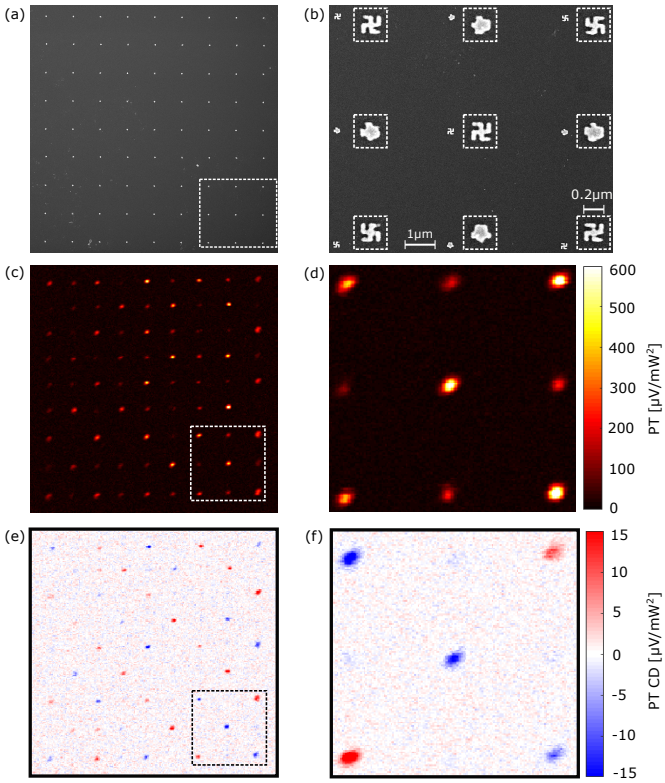

Figure 2.4: **Chirality-sensitive photothermal imaging**. (a) Scanning electron microscope (SEM) image of a 9×9 nano-gammadions array. From the 81 nanostructures, 20 are left-handed, 21 right-handed and 40 achiral. The distance between the individual nanostructures is $4\,\mu\mathrm{m}$ in both directions. (b) Higher resolution SEM image of the bottom right part of the array (the dashed rectangle in (a) shows the area for this image). Detailed images of the structures are shown in the dashed boxes, right of each structure. The scale bars are to show the average distance between two gammadions and the average size of the individual gammadions. (c) Photothermal (PT) image of the complete array, displaying the signal of each structure. We normalized the image with the heating power ($P_h \sim 9\,\mathrm{mW}$) and the probe power ($P_{probe} \sim 150\,\mu\mathrm{W}$). (d) Higher resolution photothermal image of the area shown in (b). (e), (f) Photothermal circular dichroism (PT CD) images of the areas in (a) and (b), respectively. We also normalized the images using the heating and probe powers. These images show a clear change of sign in the signal, following the chirality of the nanostructures. As expected, the nominally achiral structures show nearly zero signal. Note that the optical and SEM images cannot be overlapped because they are observed from different sides of the interface.

these images to calculate g for every structure fabricated. For this, we averaged the signal from 3×3 pixels centred at the maximum signal of each bright spot on figure 2.4 (c) and (e). Since we have correlated optical and geometrical information of our structures, we can distinguish structures with the same handedness: right-handed, left-handed and achiral (the top right, top left and top centre structure in figure 2.4 (b), respectively), and analyze their PT CD signals.

Figure 2.5 (a) shows the results for the g-factor of the 81 structures in the array correlated with their respective photothermal signals, using different colors and symbols for the three

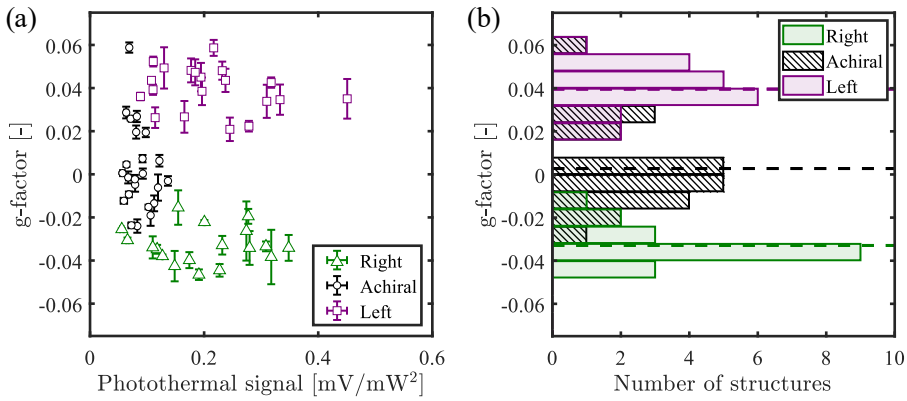

Figure 2.5: **Chirality-sensitive signal analysis.** (a) Dissymmetry factor g vs. photothermal signal for the 81 nanostructures, separated by groups according to the handedness. The inserts show the corresponding handedness for each group. We observe that the data for each group are clustered together and present some dispersion, presumably due to fabrication imperfections. (b) Histograms of g-factors for the three types of structures. We can clearly see different distributions, showing our ability to distinguish chiral and non-chiral structures. The mean g-factor for each group of nanostructures is shown in the figure as dashed horizontal lines. We assign the width of these distributions mainly to fabrication imperfections.

groups. We observe a clear separation of these groups according to their signals: we obtain positive values for left-handed structures (violet squares), negative values for the right-handed structures (green triangles) and values close to zero for most achiral structures (black dots). Every structure may have its particular fabrication imperfections which give rise to the observed distribution of g-factors, in addition to, but without clear correlation with, the size and shape variations responsible for the dispersion in photothermal signals. The histograms for g-factors are shown on figure 2.5 (b). The mean values of these distributions correspond to $g_L = (3.9 \pm 0.2) \times 10^{-2}$, $g_a = (3 \pm 3) \times 10^{-3}$ and $g_R = -(3.3 \pm 0.2) \times 10^{-2}$ for left, right and achiral structures, respectively. Despite the fabrication fluctuations, the obtained mean values for the distributions are as expected from the handedness of the structures. Moreover, they are in agreement within a factor of 2 with the values obtained using numerical simulations for the ideal gammadions, which give $g_L \sim 0.061$ at $532\,\mathrm{nm}$ for the left-handed structure. The Supporting Information (section 2.5) provides the full spectra and more details on the numerical simulations. The difference between simulated and measured data may be attributed to fabrication imperfections of the structures. In addition to measuring circular dichroism, we can easily modify our experimental setup to measure linear dichroism (LD) in any desired frame of two orthogonal axes. It suffices to exchange the quarter-wave plate for a half-wave plate to rotate the vertical and horizontal polarization states after the electro-optical modulator to the desired axis. We call this photothermal linear dichroism (PT LD). It is well known that LD is usually much stronger than CD. We thus performed a set of LD measurements on the same gammadions shown in figure 2.4 (b) in two different directions: $0, 90$ degrees (modulation V-H, i.e. without any waveplate after the EOM) and $45, 135$ degrees. Although both signals should vanish for perfect gammadions, we observed non-zero LD. We attribute this LD to the imperfections in the nanofabrication.

For the detailed experimental results, refer to the Supporting Information.

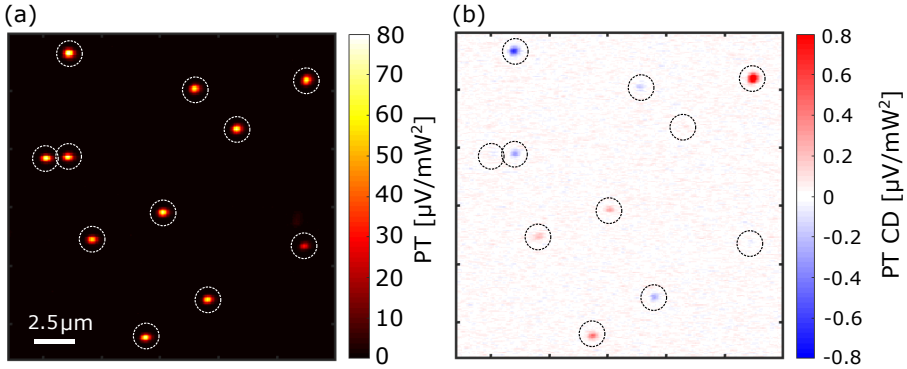

Figure 2.6: **Circular dichroism of individual nanospheres.** (a) Photothermal (PT) image showing several gold nanoparticles, diameter $100\,\mathrm{nm}$, on glass. Note the high uniformity of the spots in shape and intensity. (b) Photothermal circular dichroism (PT CD) image of the area shown in (a). Although most particles show low chirality signals, two particles have high negative (upper left corner) or positive (upper right corner) chiral signals. The g values for them are -0.83% and 1.82%, respectively. Dashed circles are guides to the eye.

As a next step, we prepared a sample with gold nanospheres of $100\,\mathrm{nm}$ diameter dispersed on a glass substrate and again we immersed this sample in toluene. Figure 2.6 (a) shows a photothermal image and (b) the corresponding photothermal circular dichroism image. In this case, as the plasmonic resonance of the spheres is around $550\,\mathrm{nm}$, the imaging conditions are close to optimal: we used a high intensity of the heating beam (heating power $P_H = 16\,\mathrm{mW}$) that is efficiently absorbed, and at the same time we increased the probe intensity to $I_p = 5000\,\mathrm{kW/cm^2}$. Because of the low absorption of the nanospheres at $780\,\mathrm{nm}$, this larger probe intensity did not lead to significant heating. The calculated temperature increase at the probe power is $16\,\mathrm{K}$. Therefore, we were more sensitive to chirality in these experimental conditions than in the experiments on gammadions.

We observe that many particles show a dim signal, close to zero, as expected for achiral structures such as spheres. However, some particles show a strong signal, either positive or negative (see two examples in Fig. 2.6 (b)). We also performed High-Angle Annular Dark-Field Scanning Transmission Electron Microscope (HAADF-STEM) imaging of gold nanospheres to obtain information about morphology and the crystalline structure of the particles. We found that some particles show defects in their crystalline structure and are non-spherical in shape (see Supporting Information for the images and more details). We therefore assign the chirality signals to the non-spherical shape and defects of nanospheres. We cannot assign the strong chirality signals to residual aggregates of nanospheres, as the photothermal signals of all particles are very uniform, indicating single nanospheres of very similar dimensions and ruling out dimers or higher aggregates. A correlation plot of photothermal signals and g-factors and the histograms of photothermal signals and g-factors for many single gold nanospheres are shown in the Supporting Information (figure S2.9).

To further test the influence of linear dichroism in the sample on our PT CD signal, we measure both PT CD and PT LD on the sample of gold nanospheres. We observed a LD signal approximately 10 times bigger than the CD signal with no clear correlation showing

that the cross talk of LD into our signal is smaller than 10%. More details about this set of measurements can be found in the Supporting Information.

2.4. Conclusion

In summary, we presented an optical method, photothermal circular dichroism, that enables us to measure the chirality of absorbing nanostructures with unprecedented signal-to-noise ratio. We experimentally showed the enantioselective character of the signal by imaging right- and left-handed plasmonic structures with quantifying dissymmetry factors $g \sim 0.04$, measured with a signal-to-noise ratio of up to 40. From estimated errors in the factors measured, we believe we could measure dissymmetry factors as small as $g_{min} = 0.004$, which approaches the orders of magnitude needed to study biological molecules in small quantities.

Photothermal circular dichroism extends the capabilities of circular dichroism due to the increased sensitivity, extending the applications of the technique to smaller quantities of analytes or shorter experiment times. Our results demonstrate several advantages of photothermal circular dichroism. First, as our detection scheme relies on measuring the local temperature increase of the nanostructure under study due to the absorption of heating photons of a controlled polarization, the polarization state of the probe light scattered by the thermal lens is irrelevant. We only need to control the polarization state of the heating beam carefully. This is in contrast to the extinction [26] or scattering-based [29, 30] detection of circular dichroism, where the polarization state of the complete beam path has to be carefully controlled. Second, since we are imaging with a photothermal-based technique, our signal can be optimized as reported earlier for photothermal signals [19]. With available tunable laser sources for the heating beam, photothermal circular dichroism can also be extended to circular dichroism spectroscopy.

2.5. Supplementary information

2.5.1. Details of the experimental setup

The schematic of our photothermal circular dichroism setup is shown in figure 2.2. Here, we explain all the components in detail. We used a Coherent Verdi laser (Model: V10-A0366, wavelength of $532\,\mathrm{nm}$) as a heating beam which was passed through an electro-optical modulator (EOM) from Qioptiq (Model: LM0202) for modulating between two orthogonal linear polarizations. The modulation frequency was set by a function generator (from Tektronix, Model: AFG3102) which sends the signals to a digital amplifier (from Qioptiq, Model: DIV20) to amplify the signal before sending it to the EOM. The function generator sends the same signal also to the lock-in amplifier (from Stanford Research Systems, Model: SR844) as a reference signal. For Koehler-like illumination a lens with focal length of $50\,\mathrm{cm}$ was used to focus the heating beam at the back focal plane of an oil-immersion objective (from Olympus, PLAPON, 60X, NA = 1.45) and to illuminate the back focal plane of the objective with low numerical aperture (NA ≈ 0.025 which corresponds to a diffraction-limited spot of $10\,\mu\mathrm{m}$ diameter). A quarter-wave plate (Thorlabs) was used to convert the linear polarization to circular and thus, we modulated the heating beam between left and right circular polarization to measure photothermal circular dichroism. The polarization state of light was analysed using a polarization analyser (Schaeffter and Kirchhoff SK010PA-VIS).

A non-polarizing $50/50$ beam splitter (Thorlabs) was used to transmit the heating beam and to reflect the probe beam. The collimated probe beam (Ti-Sapphire laser from Spectra-Physics, wavelength $780\,\mathrm{nm}$, Model: 3900S) was focused by the objective in the focal plane. To detect the back-scattered probe beam signal efficiently, we used a combination of polarizing beam splitter (PBS) and quarter-wave plate. The back-scattered probe signal was then filtered out from the heating beam by using a long-pass (750 LP) filter and focused into a photodiode (PD) from Femto (Model: DHPCA-100-F, with an amplification of 10^6) using a lens of focal length $7.5\,\mathrm{cm}$. We note that the reported laser powers are measured just before the oil-immersion objective. The photodiode signal was then sent to the lock-in amplifier as an input signal. A flippable polarizer was used to switch between normal photothermal and photothermal circular dichroism measurements. For normal photothermal microscopy, we inserted a polarizer after the EOM to achieve intensity modulation and for the photothermal circular dichroism, we removed the polarizer to keep the modulation between left and right circular polarizations. To obtain an image, we scan the sample by translating the sample stage using a piezo stage (PI P.611.3.5 Nanocube) while keeping the overlap between the heating and probe beams constant.

2.5.2. Sample design and preparation

We designed a sample that contains an array of alternating structures following the pattern showed in figure S2.1 (left). We have three types of structures: left (L), right (R) and achiral (A). The individual designs and dimensions of these structures are shown in figure S2.1 (right); all the structures have a height of $70\,\mathrm{nm}$.

The sample with the array of nanostructures was prepared using e-beam lithography and

lift-off. First, glass coverslides were cleaned by sonication in acetone and then in isopropanol for 5 minutes. Next, the coverslides were coated with PMMA e-beam resist in the following steps: 1) Dehydration of the glass slide surface by baking on a hot plate at 180 °C for 5 minutes, 2) Spin coating PMMA 950K, dilution 6% in anisole at 4000 rpm, which results in 300 nm layer thickness, 3) Baking the glass slide for 5 min at 180 °C. After spin-coating, the samples were coated with 15 nm of Cr using Temescal FC-2000 e-beam evaporator. This sacrificial layer of Cr serves to prevent charging effects on glass during e-beam patterning. The pattern was written using e-beam (Raith EBPG 5000+) with a beam step size of 1 nm and a dose of 2000 $\mu\mathrm{C/cm^2}$, which was found to be optimal through a dose test. Following the exposure, the Cr layer was stripped by wet etch in TechniEtch Cr01 (MicroChem) for 25 s and the sample was rinsed with deionized water. The pattern was developed by submerging the sample for 1 minute in a mixture of MIBK (methylisobutylketone) and IPA (isopropanol) (1:3 v/v) and further submerging into IPA for 1 minute. Finally, 70 nm of gold was evaporated onto the sample using a Temescal FC-2000 and followed by a lift-off procedure (10 minutes in n-methylpyrrolidone at 80 °C). The sample was then rinsed with acetone and IPA and spin-dried at 2000 rpm. After nanofabrication we prepared the sample for the optical measurements. We sandwiched the sample with a second cavity glass slide (Menzel number 1.5) to provide space for a liquid. We chose toluene as a liquid medium because it provides a high thermorefractive coefficient ($\partial n/\partial T = -5.68 \times 10^{-4}\ \mathrm{K}^{-1}$) which is essential for PT imaging [19]. After optical imaging, the sample was sputtered with 5 nm of platinum to make it conductive for proper imaging under a scanning electron microscope (SEM). SEM images are shown in figure S2.4

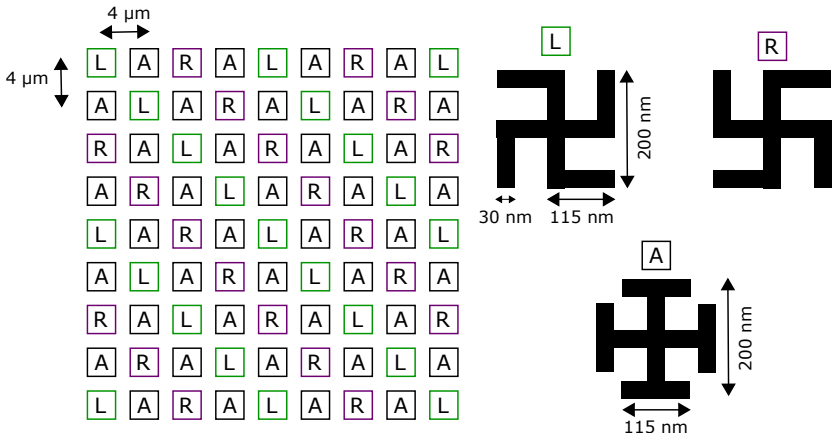

Figure 2.1: **Design of the checkerboard sample**. (Left) Array design, showing the alternation of the three types of structure: left (L), right (R) and achiral (A). (Right) Detail of the design of each type of structure. The height of the structures is 70 nm.

2.5.3. Numerical simulations

We performed numerical simulations to calculate the absorbed power for right and left circularly polarized light by the idealized gammadions structures on a glass substrate embedded in toluene. The dimensions used for the simulations are the ones depicted in figure S2.1 on the right, with a height of 70 nm. We used the commercial FDTD software Lumerical with a total-field scattered-field source [31] to simulate the plane wave heating laser and we calculated the absorbed power by the structures as

$$P_{abs} = -\frac{1}{2}\omega|\mathbf{E}|^2\Im(\epsilon)\,, \tag{2.3}$$

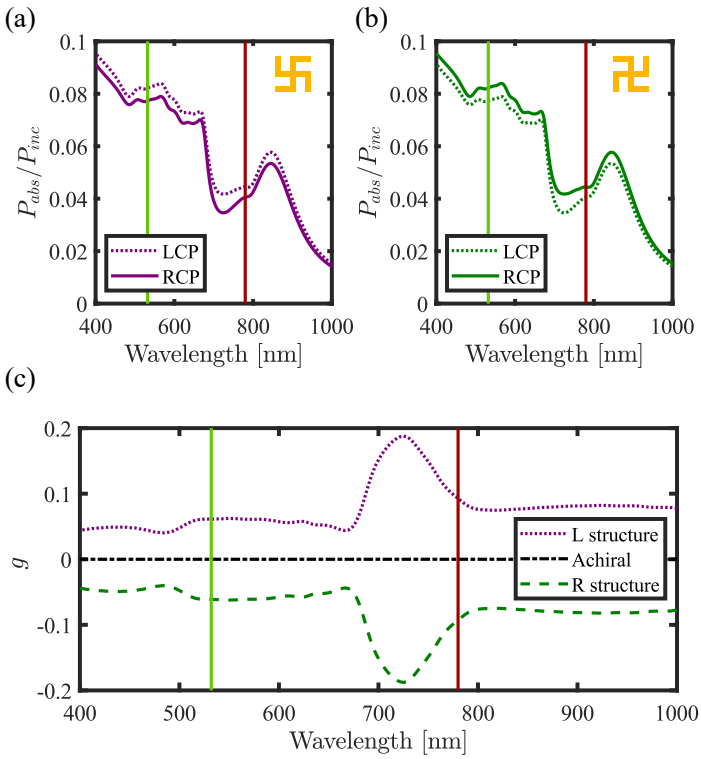

Figure S2.2: **Absorption and g-factor numerical results for ideal gammadions**. (a) Normalized absorbed power for a single left-handed gammadion structure (shown in the inset) on a glass substrate embedded in toluene. Note that the structure is now seen from the glass side and corresponds to the definition of figure 2.3 as left-handed. The absorption for LCP is higher than for RCP. (b) Normalized absorbed power for the right-handed gammadion structure (shown in the inset) on a glass substrate embedded in toluene. For this right-handed structure, the absorption for RCP is higher than for LCP. (c) Dissymmetry factor g as defined in equation 2.2 for both structures. Additionally we show the achiral structure, showing null chirality, as expected from symmetry arguments. The vertical lines in the plots correspond to the heating wavelength, 532 nm (in green), and the probe wavelength, 780 nm (in red). The absolute value of g at the heating wavelength is ~ 0.061.

where ω is the frequency of the incoming wave, $\mathbf{E}$ is the electric field in the structure and $\Im(\epsilon)$ represents the imaginary part of the permittivity [32]. Note that this is calculated for every voxel in the simulation and then integrated over a $800\,\mathrm{nm}\times800\,\mathrm{nm}\times800\,\mathrm{nm}$ volume to calculate the total absorbed power for each illumination conditions. We also calculated the absorption cross section of the gammadions at $532\,\mathrm{nm}$, obtaining $2.2\times10^4\,\mathrm{nm}^2$. In the simulation, we place the R or L gammadions made of gold on a glass substrate. For the gold structure we took the dielectric function built in the software (Gold (Au) - CRC) [33] and the one of glass from Palik [34]. The refractive index of toluene was taken from the work by Kedenburg et al. [35].

We excite the structure with a plane wave coming from the substrate side, using left and right circularly polarized light (equivalently to what we do experimentally) and for each case we calculate the absorbed power normalized by the incident power P_{abs}/P_{inc}. Figure S2.2 (a) shows the obtained spectra for both circular polarizations states for the left-handed structure and figure S2.2 (b) for the right-handed structure. Note that the former absorbs more when excited with LCP and the opposite situation holds for the latter. The vertical lines show the locations of the heating beam (green) and the probe beam (red), for reference.

Figure S2.2 (c) shows the dissymmetry factor spectra $g(\lambda)$ for both structures. Naturally, they only differ in the sign, being positive for the L structure and negative for the R structure in the studied range. For completeness we also simulated the achiral ideal structures, that exhibit null dissymmetry factor. Note that the calculated value for the dissymetry at the heating wavelength is $g\sim0.061$. We also checked that the g-factor values flip sign when we repeat the simulation with an exciting wave coming from the solvent side (we changed the wavevector from $\vec{k}\propto+\hat{z}$ to $\vec{k}\propto-\hat{z}$). This is the expected behaviour since the gammadions seen from the opposite side will have the opposite handedness.

2.5.4. Measurement of linear dichroism on gammadions

Linear dichroism is defined as the differential absorption between two orthogonal linear polarizations states:

$$LD_{\hat{\vec{n}}}=\sigma_{\parallel}-\sigma_{\perp}, \tag{2.4}$$

where $\sigma_{\parallel}$ and $\sigma_{\perp}$ represent the absorption cross section for a polarization state parallel and perpendicular to a direction given by the vector $\hat{\vec{n}}$, respectively. We performed different measurements of photothermal LD in the horizontal direction, by modulating the incoming polarization state of the heating beam between linear horizontal and vertical polarization states. To achieve this we removed the quarter-wave plate from the setup. We also measured with respect to the diagonal state (rotated $45°$), obtained by adding a half-wave plate. The reason for doing these two types of polarization modulations is to obtain full information about the linear dichroism signals. Figure S2.3 shows the photothermal LD images of the same gammadion structures as shown in figure 2.4(b). We clearly see non-zero linear dichroism signals, of similar order but stronger than circular dichroism signals. We attribute this to the fabrication imperfections in the sample, which break the symmetry of the structures. As figure S2.3 (d) shows, there is no obvious correlation between LD and CD.

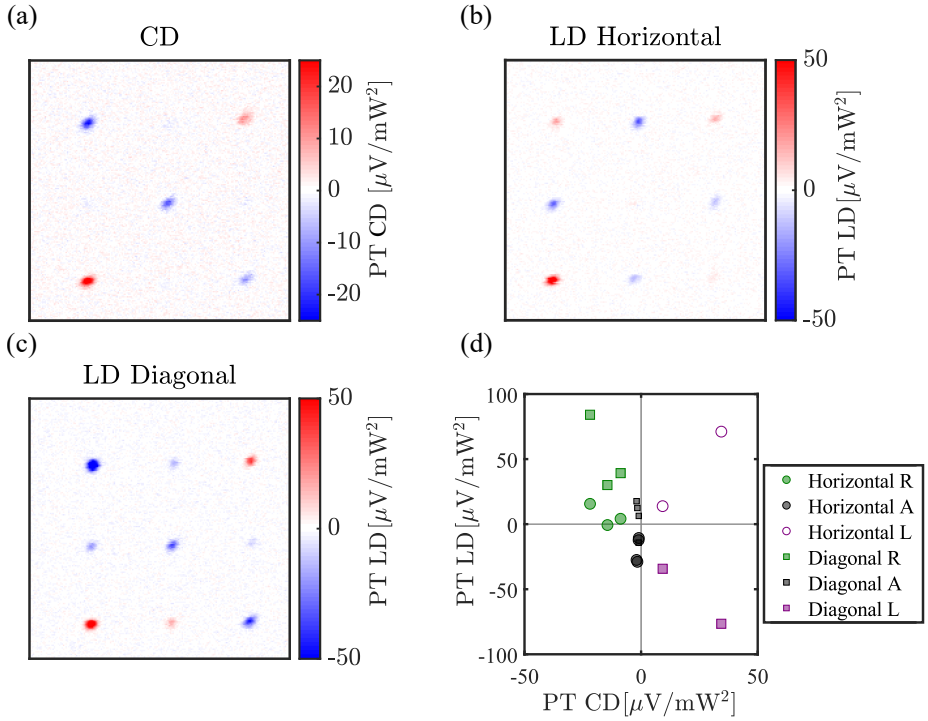

Figure S2.3: **Linear dichroism measurements of the gammadion sample**. (a) Photothermal circular dichroism image of 9 gammadions (the same as shown in figure 2.3 (b) and (d)). (b) Photothermal linear dichroism image of the same area as (a), with horizontal-vertical modulation (90° and 0°). (c) Photothermal linear dichroism in the diagonal direction, i.e. polarization modulation between 45° and −45°. (d) Correlation plot of the PT CD and PT LD.

2.5.5. Characterization of nanospheres shape and size

We studied in detail the morphological characteristics of the nanospheres used for the optical imaging by performing High-Angle Annular Dark-Field Scanning Transmission Electron Microscope (HAADF-STEM) imaging on a dispersion of such nanoparticles. The HAADF-STEM images were acquired using a Thermo Fisher Scientific Tecnai Osiris microscope operated at 200 kV with a 50 pA beam current and a frame time of 6 s. All tomography series were acquired by taking projection images over an angular range of ±75° with a tilt increment of 3° with a frame time of 6 s. After alignment of the projection images by using a cross correlation, the stacks of aligned projection images served as inputs for 20 iterations of the expectation maximization reconstruction implemented in the ASTRA toolbox [36]. Figure S2.4 shows representative HAADF-STEM images of gold nanospheres from the same synthesis batch at different resolutions. In figure S2.4 (a) we present a zoom on the remarkably non-spherical particles, marked with an arrow. In figure S2.4 (b) we zoom in further and again present in the rectangles a closer image of a few non-spherical particles. Figures S2.4 (c) and (d) depict higher resolution images where the facets of some of the nanoparticles im-

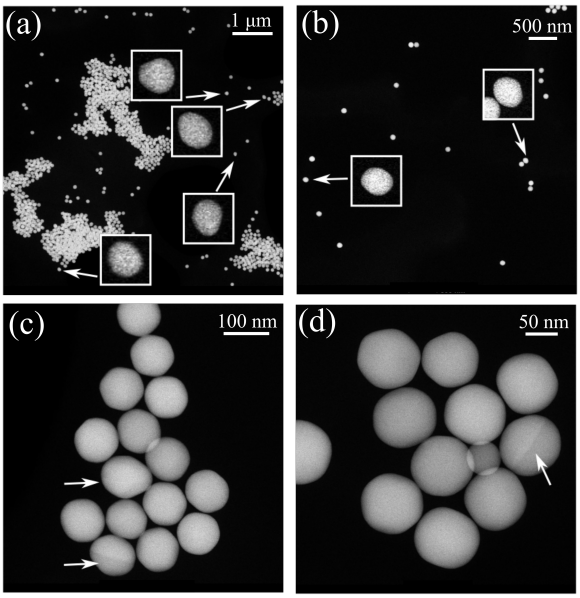

Figure S2.4: **HAADF-STEM images of gold nanospheres**. (a) Large area scan to provide an overview of many nanoparticles. The rectangles contain a zoomed image on the particles marked with arrows, where non-spherical shape is clearly observed. (b) Image of a different area of the sample, with higher magnification than in (a). Again, we show in the rectangles a zoom on the particles marked with arrows. (c) Higher resolution image of a cluster of nanoparticles. The arrows depict the particles with the strongest deviation from spherical shape. (d) Closer look on another cluster of particles, where the arrow now depicts a particle with defects in the crystalline structure. Most particles exhibit faceted spherical-like shapes. However, a fraction of the nanospheres are anisotropic and/or exhibit crystal defects as evident from the contrast difference. Examples of such particles are marked by arrows in the images. The scale bars are shown in each panel.

aged can be clearly appreciated. The arrows point to the non-spherical shaped nanoparticles we found. In addition, the arrow in figure S2.4 (d) shows a particle with defect in the crystalline structure. From the 2D images it can be observed that most nanospheres are isotropic. However, some nanospheres display lattice defects or are anisotropic. The defects are most likely twin boundaries as evident from the contrast difference in the HAADF-STEM images for such particles. Because the displayed images are only 2D projections of the real 3D object, we also performed electron tomography to obtain the 3D shape of a characteristic nanosphere. In addition, we quantified the size distribution of our sample of nanoparticles by extracting the measured the radius from STEM images. The obtained histogram is depicted in figure S2.5. While the nominal radius given by the manufacturer (Nanocomposix) is $100\,\mathrm{nm}$ we measured an average value of $94\,\mathrm{nm}$.

2.5.6. Does linear dichroism influence photothermal circular dichroism?

In order to characterize the crosstalk in our photothermal circular dichroism signal with linear dichroism, we measured both circular dichroism and linear dichroism of the same nanoparticles, characterized in the previous section. Figure S2.6 shows photothermal, pho-

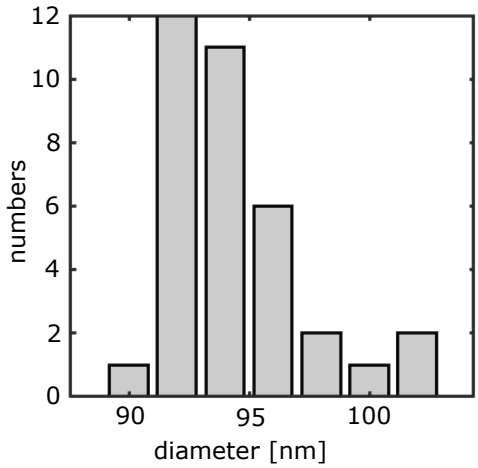

Figure S2.5: **Size distribution of the nanoparticles from HAADF-STEM**. The particle sizes are calculated from 35 single particles from the images shown in figure S2.4 (b). The average particle size is 94 nm with a size dispersion of 3%.

tothermal circular dichroism and photothermal linear dichroism signals of single 100 nm gold nanospheres. The value of the nanosphere size is 100 nm provided by the manufacturer, however the average particle size calculated from STEM image is rather 94 nm (see

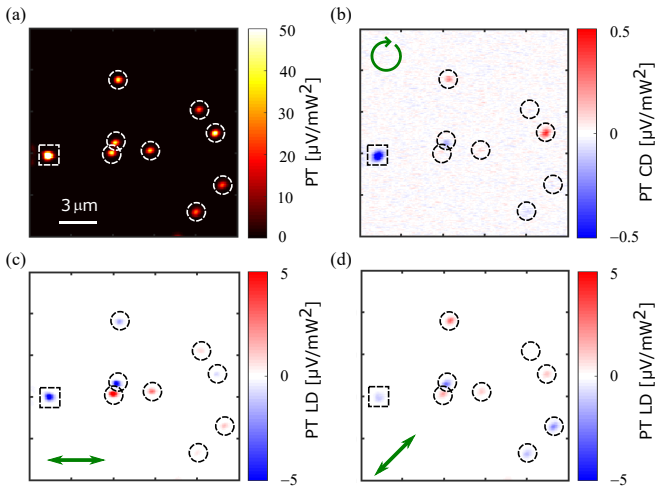

Figure S2.6: **Circular dichroism and linear dichroism measurements of gold nanospheres**. (a) Photothermal (PT), (b) photothermal circular dichroism (PT CD), (c) photothermal linear dichroism (PT LD) with 90° and 0° (horizontal-vertical) polarization modulation and (d) photothermal linear dichroism (PT LD) with −45° and 45° (diagonals) polarization modulation. Dashed circles are drawn to show single particle spots. The left-most particle is probably an aggregate and marked with a dashed square box. The arrows show the direction $\vec{n}$ for the LD.

figure S2.5). Note that the colour scale in photothermal circular dichroism and photothermal linear dichroism images are 100 times and 10 times smaller than PT image, respectively. Most particles show weak circular dichroism but strong linear dichroism signal. This indicates that there is little crosstalk between the photothermal circular dichroism signal and linear dichroism. We attribute the linear dichroism signal of nanospheres to shape and crystallinity imperfections of individual nanoparticles. All the images of PT CD and PT LD of gammadions and gold nanospheres are X channel signals of lock-in to show phase information. We chose X channel signal instead of Y channel because at our measurement modulation frequency, most nanostructures or nanoparticles show in-phase signals.

2.5.7. More measurements of circular dichroism of gold nanospheres

We measured photothermal (PT) and photothermal circular dichroism (PT CD) of single 100 nm gold nanospheres deposited on a glass substrate. The images for two different areas in both imaging modes are shown in figure S2.7. Most particles show weak photothermal circular dichroism signals and are distributed between positive and negative PT CD signals.

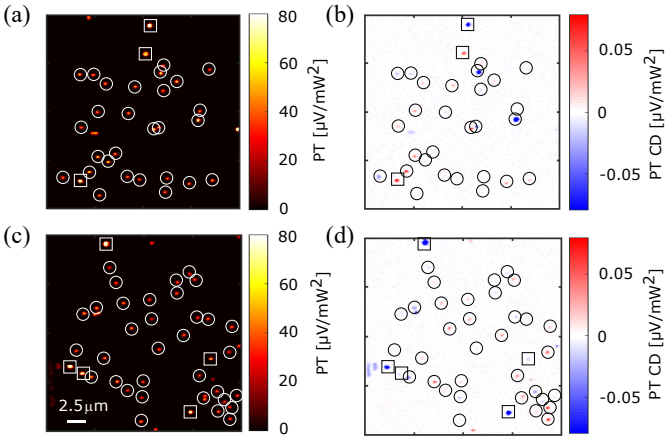

Figure S2.7: **Circular dichroism measurements of gold nanospheres on glass**. (a) Photothermal (PT) image of an area showing many nanospheres. Note the small dispersion in PT intensities, showing a remarkably small dispersion in size for the nanoparticles. (b) Photothermal circular dichroism (PT CD) of the same area as (a). (c) Photothermal (PT) image of a different area of the sample, showing more nanospheres. (d) Photothermal circular dichroism (PT CD) of the same area as (c). The solid circles are drawn to show correlative image spots between PT and PT CD images and to show which particles are considered for the correlation and histogram analyses. Extremely bright particles (marked with solid square boxes) in the photothermal image are probably aggregates and were ignored for the analysis. We also ignored the particles which are on the edge of the scan for the analysis.

We calculated the g-factor by averaging the signal of 3×3 pixels at the maximum intensity for each spot in the images, excluding exceptionally bright spots in both photothermal and photothermal circular dichroism images, which are assigned to clusters of nanoparticles. We used equation 2.2 for the g-factor definition. A correlation plot of g-factor and photothermal signal of 59 single gold nanospheres is shown in figure S2.8 along with corresponding histogram of g-factors. Most particles show g-factors less than 1% and normally distributed

between positive and negative signals, with a small mean value of 0.16% (which may be the experimental bias). For a perfect spherical particle, photothermal circular dichroism is

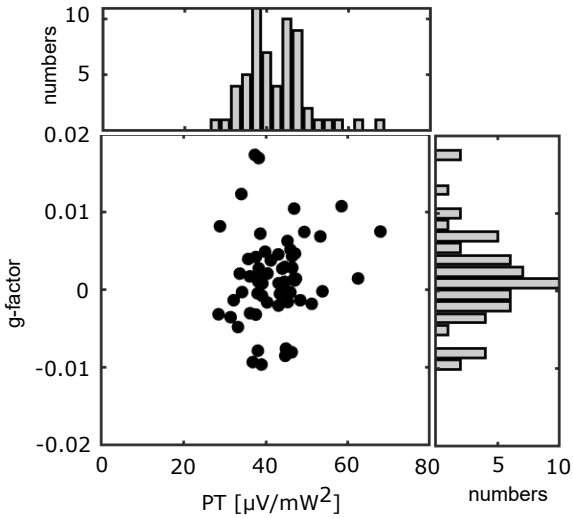

Figure S2.8: **Histogram of PT and PT CD of gold nanospheres on glass**. Correlation plot of measured g-factor and photothermal signal and histograms of photothermal signal and g-factor. The histogram of photothermal signal looks narrow, which is consistent with the histogram of particle sizes shown in figure S2.5. The dispersion in particle size is 3% and the dispersion in photothermal signal is 18%. The distribution of photothermal signals follows from the distribution of particle sizes, and from the dispersion in orientations and shapes of the nanoparticles (as we see in figure S2.4). Most particles show g-factors less than 1%. The mean value of g-factor is 0.0016.

expected to be null. However, a fraction of particles in our measurements are non-spherical in shape and have defects in their crystal structure as we see from the STEM images in figure S2.4. We therefore attribute the observed photothermal circular dichroism signal to the particle's shape and defects. To understand in detail how the particle shape and defects play role in the photothermal circular dichroism signal, a careful correlated optical and TEM-tomography should be performed, which is outside the scope of this work.

2.5.8. Line profiles of PT and PT CD signal of gold nanospheres

To further characterize our PT-CD microscope, we present here representative cross sections from our optical images when the object imaged is smaller than the diffraction limit, i.e. we show a linear profile of the point-spread-function (PSF) of our microscope. The line profiles of PT and PT CD signals of two gold nanospheres are shown in figure S2.9. The point-spread functions of both PT and PT CD signal look similar except for some wrinkles appearing as side bands in PT CD profile. These wrinkles are attributed to low signal-to-noise ratio in PT CD signal.

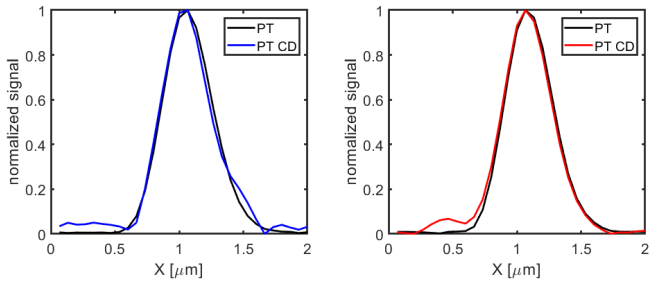

Figure S2.9: **Line profiles of PT and PT CD of gold nanospheres**. Line profiles of PT and PT CD signal of two gold nanospheres. (Left) the line profiles of the top left particle in figure 2.6 (a), (b) and (right) the line profiles of the top right particle in figure 2.6 (a), (b). Please note the color of the PT CD line profiles (same color as in figure 2.6 (b)). For the particle with negative PT CD signal, the line profile is shown with absolute values. All line profiles are normalized by the maximum peak signals.

2.5.9. Temperature increase due to absorption of the heating and probe beams

The (local) increase in temperature of a nanostructure due to light absorption in the steady state case for a sphere can be calculated as

$$\Delta T = \frac{P_{disp}}{4\pi\kappa R}\,, \tag{2.5}$$

where P_{disp} is the power dissipated by the nanosphere, κ is the average thermal conductivity of the medium and the glass substrate ($\kappa = (\kappa_{medium} + \kappa_{glass})/2$) and R is the radius of the nanosphere [37]. With our experimental parameters, we obtained ΔT_{sphere} of $8\,\mathrm{K}$ and $16\,\mathrm{K}$ at the heating and probe powers, respectively.

When the structure is not spherical in shape, as it is for our gammadions, there is no simple expression to calculate the temperature increase. However, a common approach for other nanostructure shapes is to use equation 2.5 replacing the radius R with a fictitious radius R_L that can be calculated for different geometries [37]. Thus, we used $R_L = 200\,\mathrm{nm}$ in this equation to approximate the increase in temperature, obtaining $11.7\,\mathrm{K}$ and $97.5\,\mathrm{K}$ at the heating and probe powers, respectively. The boiling temperature of toluene ($393\,\mathrm{K}$, or $120\,^{\circ}\mathrm{C}$, taking surface tension into account) provides an upper bound for the maximum temperature reached by the gammadion.

References

[1] Kelvin, W. T. B. *Baltimore lectures on molecular dynamics and the wave theory of light*; CJ Clay and Sons, 1904.

[2] Schäferling, M. *Chiral Nanophotonics*; Springer, 2017; p 159.

[3] Alberts, B.; Johnson, A.; Lewis, J.; Raff, M.; Roberts, K.; Walter, P. *Molecular biology of the cell*, 6th ed.; Garland Science: New York, 2010.

[4] Siegel, J. S. Biochemistry: Single-handed cooperation. *Nature* **2001**, *409*, 777.

[5] Fasman, G. D. *Circular dichroism and the conformational analysis of biomolecules*; Springer Science & Business Media, 2013.

[6] Beychok, S. Circular dichroism of biological macromolecules. *Science* **1966**, *154*, 1288–1299.

[7] Berova, N.; Nakanishi, K.; Woody, R. W. *Circular dichroism: principles and applications*; John Wiley & Sons, 2000.

[8] Johnson Jr, W. C. Secondary structure of proteins through circular dichroism spectroscopy. *Annual review of biophysics and biophysical chemistry* **1988**, *17*, 145–166.

[9] Greenfield, N. J. Using circular dichroism spectra to estimate protein secondary structure. *Nature protocols* **2006**, *1*, 2876.

[10] Schnoering, G.; Poulikakos, L. V.; Rosales-Cabara, Y.; Canaguier-Durand, A.; Norris, D. J.; Genet, C. Three-Dimensional Enantiomeric Recognition of Optically Trapped Single Chiral Nanoparticles. *Phys. Rev. Lett.* **2018**, *121*, 023902.

[11] Narushima, T.; Okamoto, H. Circular dichroism nano-imaging of two-dimensional chiral metal nanostructures. *Phys. Chem. Chem. Phys.* **2013**, *15*, 13805–13809.

[12] Arteaga, O.; Sancho-Parramon, J.; Nichols, S.; Maoz, B. M.; Canillas, A.; Bosch, S.; Markovich, G.; Kahr, B. Relation between 2D/3D chirality and the appearance of chiroptical effects in real nanostructures. *Optics Express* **2016**, *24*, 2242–2252.

[13] García-Etxarri, A.; Dionne, J. A. Surface-enhanced circular dichroism spectroscopy mediated by nonchiral nanoantennas. *Physical Review B* **2013**, *87*, 235409.

[14] Kramer, C.; Schäferling, M.; Weiss, T.; Giessen, H.; Brixner, T. Analytic optimization of near-field optical chirality enhancement. *ACS photonics* **2017**, *4*, 396–406.

[15] Yamauchi, M.; Mawatari, K.; Hibara, A.; Tokeshi, M.; Kitamori, T. Circular dichroism thermal lens microscope for sensitive chiral analysis on microchip. *Analytical chemistry* **2006**, *78*, 2646–2650.

[16] Kong, X.-T.; Khosravi Khorashad, L.; Wang, Z.; Govorov, A. O. Photothermal Circular Dichroism Induced by Plasmon Resonances in Chiral Metamaterial Absorbers and Bolometers. *Nano Letters* **2018**, 2001–2008.

[17] Boyer, D.; Tamarat, P.; Maali, A.; Lounis, B.; Orrit, M. Photothermal imaging of nanometer-sized metal particles among scatterers. *Science* **2002**, *297*, 1160–1163.

[18] Berciaud, S.; Lasne, D.; Blab, G. A.; Cognet, L.; Lounis, B. Photothermal heterodyne imaging of individual metallic nanoparticles: Theory versus experiment. *Physical Review B* **2006**, *73*, 045424.

[19] Gaiduk, A.; Ruijgrok, P. V.; Yorulmaz, M.; Orrit, M. Detection limits in photothermal microscopy. *Chemical Science* **2010**, *1*, 343.

[20] Selmke, M.; Braun, M.; Cichos, F. Photothermal single-particle microscopy: detection of a nanolens. *ACS Nano* **2012**, *6*, 2741–2749.

[21] Yorulmaz, M.; Khatua, S.; Zijlstra, P.; Gaiduk, A.; Orrit, M. Luminescence quantum yield of single gold nanorods. *Nano Letters* **2012**, *12*, 4385–4391.

[22] Yorulmaz, M.; Nizzero, S.; Hoggard, A.; Wang, L.-Y.; Cai, Y.-Y.; Su, M.-N.; Chang, W.-S.; Link, S. Single-Particle Absorption Spectroscopy by Photothermal Contrast. *Nano Letters* **2015**, *15*, 3041–3047.

[23] Hou, L.; Adhikari, S.; Tian, Y.; Scheblykin, I. G.; Orrit, M. Absorption and quantum yield of single conjugated polymer poly [2-methoxy-5-(2-ethylhexyloxy)-1, 4-phenylenevinylene](MEH-PPV) molecules. *Nano Letters* **2017**, *17*, 1575–1581.

[24] Gaiduk, A.; Yorulmaz, M.; Ruijgrok, P. V.; Orrit, M. Room-Temperature Detection of a Single Molecule's Absorption by Photothermal Contrast. *Science* **2010**, *330*, 353–356.

[25] Kuwata-Gonokami, M.; Saito, N.; Ino, Y.; Kauranen, M.; Jefimovs, K.; Vallius, T.; Turunen, J.; Svirko, Y. Giant optical activity in quasi-two-dimensional planar nanostructures. *Physical Review Letters* **2005**, *95*, 227401.

[26] Vinegrad, E.; Vestler, D.; Ben-Moshe, A.; Barnea, A. R.; Markovich, G.; Cheshnovsky, O. Circular Dichroism of Single Particles. *ACS Photonics* **2018**, *5*, 2151–2159.

[27] Nechayev, S.; Barczyk, R.; Mick, U.; Banzer, P. Substrate-Induced Chirality in an Individual Nanostructure. *ACS Photonics* **2019**, *6*, 1876–1881.

[28] Jackson, J. D. *Classical electrodynamics*, 3rd ed.; John Wiley & Sons: New York, 1998.

[29] Karst, J.; Karst, J.; Cho, N. H.; Kim, H.; Lee, H.-E.; Nam, K. T.; Giessen, H.; Hentschel, M. Chiral Scatterometry on Chemically Synthesized Single Plasmonic Nanoparticles. *ACS Nano* **2019**, *13*, 8659–8668.

[30] Wang, L.-Y.; Smith, K. W.; Dominguez-Medina, S.; Moody, N.; Olson, J. M.; Zhang, H.; Chang, W.-S.; Kotov, N.; Link, S. Circular Differential Scattering of Single Chiral Self-Assembled Gold Nanorod Dimers. *ACS Photonics* **2015**, *2*, 1602–1610.

[31] Lumerical: Sources - TFSF. `https://kb.lumerical.com/ref_sim_obj_sources_tfsf.html`, Accessed: 2010-09-11.

[32] Lumerical: advanced spatial absorption. `https://kb.lumerical.com/layout_analysis_pabs_adv.html`, Accessed: 2010-08-16.

[33] Lumerical: Material Database. `https://kb.lumerical.com/materials_material_database_optical.html`, Accessed: 2010-09-11.

[34] Palik, E. D. *Handbook of optical constants of solids*; Academic press, 1998; Vol. 3.

[35] Kedenburg, S.; Vieweg, M.; Gissibl, T.; Giessen, H. Linear refractive index and absorption measurements of nonlinear optical liquids in the visible and near-infrared spectral region. *Optical Materials Express* **2012**, *2*, 1588–1611.

[36] van Aarle, W.; Palenstijn, W. J.; Beenhouwer, J. D.; Altantzis, T.; Bals, S.; Batenburg, K. J.; Sijbers, J. The ASTRA Toolbox: A platform for advanced algorithm development in electron tomography. *Ultramicroscopy* **2015**, *157*, 35 – 47.

[37] Baffou, G.; Berto, P.; Bermúdez Ureña, E.; Quidant, R.; Monneret, S.; Polleux, J.; Rigneault, H. Photoinduced heating of nanoparticle arrays. *Acs Nano* **2013**, *7*, 6478–6488.

3

Photothermal circular dichroism of single nanoparticles rejecting linear dichroism by dual modulation

Circular dichroism (CD) is the property of chiral nanoobjects to absorb circularly polarized light of either handedness to different extents. Photothermal microscopy enables the detection of CD signals with high sensitivity and provides a direct absorptive response of the samples under study. To achieve CD measurements at the single-particle level one must reduce such artefacts as leakage of linear dichroism (LD) and residual intensity modulation. We have simulated our setup with a simple model, which allows us to tune modulation parameters to obtain a CD signal virtually free from artefacts. We demonstrate the sensitivity of our setup by measuring the very weak inherent CD signals of single gold nanospheres. We furthermore demonstrate that our method can be extended to obtain spectra of the full absorptive properties of single nanoparticles, including isotropic absorption, linear dichroism and circular dichroism. We then investigate nominally achiral gold nanoparticles immersed in a chiral liquid. Carefully taking into account the intrinsic chirality of the particles and its change due to heat-induced reshaping, we find that the chiral liquid carvone surrounding the particle has no measurable effect on the particles' chirality, down to g-factors of 3×10^{-4}.

This chapter is based on the publication in ACS Nano **15**, 10 (2021).

3.1. Introduction

Circular dichroism (CD) is exhibited by chiral molecules or structures that display different absorption for circular polarized light of either handedness. This absorptive property provides valuable structural information about the molecules or the objects under study. The dispersive counterpart of CD is called circular birefringence (CB) and is considered less often, although the CB and CD spectra, being related by a Kramers-Kronig relation [1, 2], have the same physical content. Several other groups have specifically designed plasmonic and dielectric structures to enhance the weak light-molecule interaction [3–9], either by enhancing the local field or by enhancing the helicity of the field. Both chirality enhancement approaches lead to an increased differential absorption (g-factor). The ultimate goal of both approaches, field or helicity enhancement, is to eventually sense chirality (CD and CB) at the single-molecule level. However, this very ambitious goal is still extremely remote. Here, we propose to improve the sensitivity of pure CD measurements of single nanoparticles in an optical microscope. CD is typically measured on large ensembles of the analytes of interest, in transmission through a solution. The light polarization is modulated at high frequencies and the polarization-dependent transmission is analyzed with a lock-in amplifier. Modern CD spectro-polarimeters operate according to a dual-polarization modulation scheme, described by Jellison et al. [10, 11]. This scheme facilitates the simultaneous measurement of multiple optical properties. This method is a standard way to obtain CD spectra of drugs and biomolecules including proteins, providing a sensitivity to differential absorptions as low as 10^{-5}. However, due to their requirement of large volumes of analyte, these spectro-polarimeters naturally lack spatial resolution and therefore are not suitable to perform CD measurements on single nanoparticles or even on minute quantities of biomolecules. In bulk measurements on solutions, the linear dichroism (LD), i.e., the differential absorption of individual molecules or particles for light polarized linearly in different directions naturally vanishes in the orientational average, unlike their CD. At the single-particle level, however, LD can be very strong, e.g., because of shape-dependent plasmon resonances. Therefore, conventional CD spectroscopy is difficult to apply to single LD-active particles or to small ensembles thereof, because of cross talk between LD and CD signals, hereafter referred to as LD-to-CD leakage.

An extinction-based approach to CD measurements of single nanoparticles was proposed by Markovich and coworkers [12]. In their scheme, the probing beam must fulfill very strict polarization requirements, not only on the excitation path but also on the detection path. A single-laser method that aims at high spatial resolution requires strongly focused light and thereby large-NA objectives. Under these tight focusing conditions, the polarization distribution in the focus plane is complex [13], due to contributions of the large span of angles necessary to produce a diffraction-limited focus. Moreover, the high NA renders the technique prone to artefacts owed to tiny imperfections of the beam alignment [14]. Any offset of the beam from the center of the objective will lead to a difference in the intensity distribution in the focus for different polarizations. This difference can easily be as large as 10^{-2} in relative intensity units, even for small beam deviations. Thus, these artefacts can easily dominate typical CD values.

Recently, we proposed a photothermal microscopic technique to image CD [15] which, thanks to its two-color scheme, separates the two conflicting requirements of polarization

purity and high spatial resolution. As the heating beam is only weakly focused, due to Koehler illumination, there are no large angles in the focus plane, which greatly facilitates high polarization purity in the focus. At the same time, the strongly focused probe beam that only senses heating effects ensures a high spatial resolution. Additionally, because it relies on the photothermal effect, the technique provides the direct absorptive response of the sample, free from scattering and birefringence contributions. Our first demonstration experiment [15], despite its high sensitivity, was prone to a number of artefacts due to the single, square-wave modulation scheme of the polarization of the heating beam. Herein, we propose a series of improvements to remedy these defects.

A first artefact that must be eliminated is residual intensity modulation of the probe or pump beam that possibly occurs at the measurement frequency of CD. We utilize a dual-modulation method similar to the one described by Jellison et al. [11] using two sinusoidally driven polarization modulators, a photo-elastic modulator (PEM) and an electro-optical modulator (EOM) and demodulate the signal at their sum frequency, here $\omega_1 + \omega_2$. The choice of at least one EOM is convenient to fulfill the requirement of a tunable bias retardation, whose importance is explained in the Supporting Information (SI). The mechanical oscillation of the piezoelectric actuators of the PEM can cause tiny vibrations at the PEM modulation frequency and lead to residual modulation of the collected probe light intensity and to a background signal. Likewise, the electro-optic modulator exhibits a slight residual intensity modulation on top of the polarization modulation, due to photoelastic scattering. This effect, also referred to as residual amplitude modulation [16, 17] leads to undesired intensity modulation of the heating beam at the driving frequency of the EOM modulator. Both the PEM's and the EOM's intensity modulations will cause artefact CD signals for any absorbing sample if CD is measured directly at the driving frequency of the individual modulators.

A second artefact that has to be taken care of is the possible cross talk between LD and CD effects [11, 18–21]. This artefact is mainly induced by static linear birefringence of the optical components, and in the special case of quarter-wave plates (QWP) by deviations from the perfect $\pi/2$ retardation. When performing measurements of ensembles of isotropically distributed molecules or particles in solution, linear dichroic effects can be neglected thanks to ensemble averaging. When performing CD studies of individual plasmonic particles, it is crucial to avoid this cross talk as the LD of plasmonic particles can easily exceed their CD by some orders of magnitude. Any sample exhibiting LD can cause an artefact signal in a CD measurement. When LD-to-CD leakage is not carefully removed, it can lead to erroneous interpretations of the results. The reverse effect, CD-to-LD leakage, although present in principle, can be neglected as long as CD is much weaker than LD.

To solve all problems of residual intensity modulation and of the cross-talk between CD and LD, we apply a purely sinusoidal modulation scheme based on the design of Jellison et al. [11]. We insert an additional quarter-wave plate (QWP) on the heating beam path. This QWP shifts the CD signal to the sum $\omega_2 + \omega_1$ and the difference $\omega_2 - \omega_1$ frequencies of the two modulators. We perform lock-in detection at one of these two frequencies. We have chosen the sum frequency, because we expect less 1/f noise at higher frequencies. More importantly, at these combination frequencies the small residual intensity modulations of the two modulators become second-order effects which can be safely neglected. Furthermore, if we choose the first modulator to be the EOM, we find that the cross talk of LD into CD

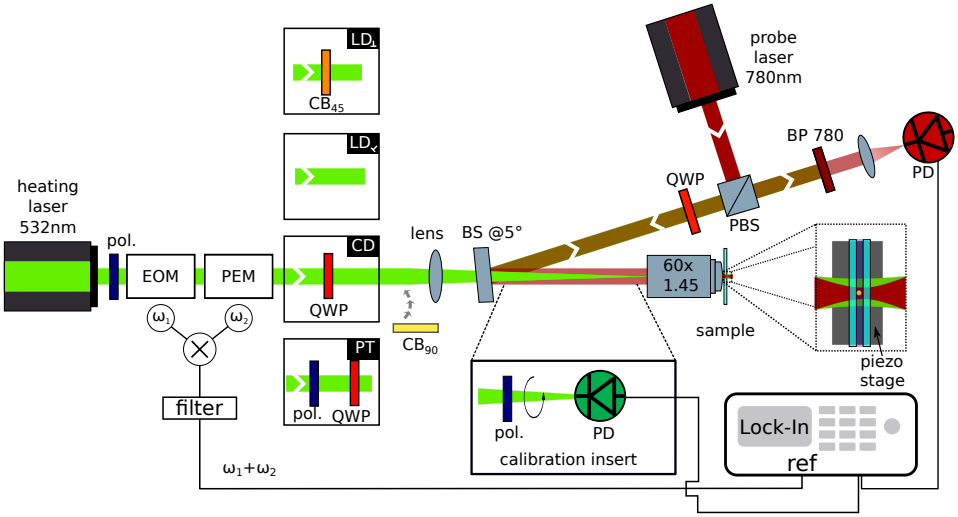

Figure 3.1: Schematic representation of the dual modulation PTCD setup with the additional calibration insert, where a rotatable calibration polarizer and photodiode (PD) can be inserted into the heating beam path. By flipping a set of different polarization components, i.e. circular birefringence plates and polarizer, we are able to measure all absorptive properties CD, $LD_{\perp}$, $LD_{\swarrow}$, as well as the isotropic absorption of the sample. The $532\,\mathrm{nm}$ heating laser is passed through a polarizer and two polarization modulators, the electro-optic modulator (EOM) and the photoelastic modulator (PEM). To measure PT, CD and both LDs, we insert different sets of polarization components (polarizer, quarter-wave plate (QWP) and circular birefringent plate CB_{45} which rotates the linear polarization by $45°$). The circular birefringent plate CB_{90} which rotates any linear polarization by $90°$ is used to check the leakage of LD into CD. The heating laser is focused at the back focal plane of the objective by means of a wide-field lens (focal length $50\,\mathrm{cm}$) in a Koehler scheme, to illuminate a sample area of about $20\,\mu\mathrm{m}^2$. The $780\,\mathrm{nm}$ CW probe laser is used in a configuration combining a polarizing beam-splitter (PBS) and a QWP. The probe laser is reflected at a 50/50 beam-splitter (BS) at an angle of $5°$ and focused in the sample plane using a high-NA oil-immersion objective (60X, NA=1.45). The sample is scanned using a piezo stage. The reflected probe beam at the glass-oil interface interferes with the probe beam scattered by the thermal lens. The interference signal is filtered from the heating laser using a band-pass filter (BP 780) and focused onto a photodiode connected with a lock-in amplifier. A frequency mixer is used to mix two frequencies used for modulation of the two modulators and sent to the lock-in as a reference frequency.

induced by imperfections of the optical components, such as residual static birefringence exhibited by EOM, PEM or QWP, can be compensated in a straightforward manner by combining a slight rotation of the QWP with tuning of the bias voltage of the EOM. Figure 3.1 illustrates our imaging photothermal microscope with dual polarization modulation. The setup is not only capable of measuring circular dichroism but furthermore has the capability to measure linear dichroism and the full absorption of one of the circular polarizations. Together with CD, this measurement provides the isotropic absorption that could be measured in an unpolarized photothermal experiment. It is important to stress here that, to fully retrieve the LD information, at least two measurements have to be performed, one in the [0°; 90°] basis and one in the [+45°;-45°] basis. We abbreviate the former with $LD_{\perp}$ and the latter with $LD_{\swarrow}$. The heating beam ($532\,\mathrm{nm}$) is polarization-modulated by the EOM and the PEM in series. It then passes a variable set of polarization optics that define the

operation mode of the setup: i) $LD_{\diagup}$ -sensitive without any additional polarization element, ii) $LD_{\perp}$-sensitive with a 45°-circular birefringent plate (or 45°-polarization rotator), iii) CD-sensitive with QWP alone, iv) photothermal absorption-sensitive (PT) with a linear polarizer (0°) and QWP. The QWP placed after the polarizer practically provides the isotropic absorption signal in the usual case of particles with very weak CD. Illumination with this intensity-modulated, circularly-polarized heating beam provides us with a signal which is very close to the regular photothermal signal, and therefore allows us to normalize the CD and LD signals to the isotropic absorption of the particle. In this manner, we calculate the g-factor of a sample by simply dividing the CD or LD measurement with the respective PT measurement

$$g_{CD(LD)} = \frac{CD(LD)}{PT}. \tag{3.1}$$

The respective FFT spectra of signals in the different measurement modes are shown in figures S3.2-S3.4. For objects with strong LD signals, a 90°-circular birefringent plate can be added [22], to further improve the cancellation of LD-to-CD leakage and other LD-related artefacts. The heating beam is weakly focused on the sample ($5\,\mu\mathrm{m}$ in the focal plane, corresponding to an effective NA of ∼0.07), whereas the probe beam (at $780\,\mathrm{nm}$) is tightly focused to retain a high spatial resolution. The reflected probe beam is then cleaned up by removing any residual heating light by means of a long-pass filter and sent to a photodiode for detection. A more detailed description of the setup and the purpose of the 90°-circular birefringent plate can be found in the SI.

3.2. Results and discussion

3.2.1. Simulations

To optimize its performance, we modeled our setup by means of Jones matrix calculus and performed simulations to choose the optimal modulation parameters and to estimate the setup's sensitivity to misalignment and imperfections of its optical components. We want to point out here that there is no need to perform a full Mueller matrix analysis as the weakly focused heating beam (∼$5\,\mu\mathrm{m}$) is free from the various depolarizing effects that can occur in tightly focused beams and in transmission methods [20]. In an ideal setup, i.e. if we were only sensitive to CD, we expect zero modulation depth at the sum (or difference) frequency when looking at purely linear dichroic samples. Due to imperfections of the optical elements, however, we have to anticipate cross talk between CD and LD. To quantify this cross talk, we calculate the rejection ratio $R_{ext} =\mid LD(\omega_1 + \omega_2) \mid / \mid CD(\omega_1 + \omega_2) \mid$ that we define as the ratio of the absolute value of the LD, divided by the absolute value of the spurious CD signal measured in the CD channel for a nanoparticle with pure LD absorption, without any intrinsic CD. We calculate that ratio at the sum frequency of the two modulators and under the assumption that the absorption asymmetry (g-factor) is the same for 3 ideal samples showing pure $LD_{\perp}$, $LD_{\diagup}$, and CD. Unlike other dual modulation approaches [11, 23] we keep the amplitudes of the phase modulation of the two modulators fixed (both $\pi/2$) and explore the effect of changing the EOM bias retardation and the QWP's fast axis orientation on the rejection ratio of $LD_{\perp}$ and $LD_{\diagup}$. Our goal is to find a set of modulation parameters that optimizes this rejection ratio and thereby reduces the cross talk between

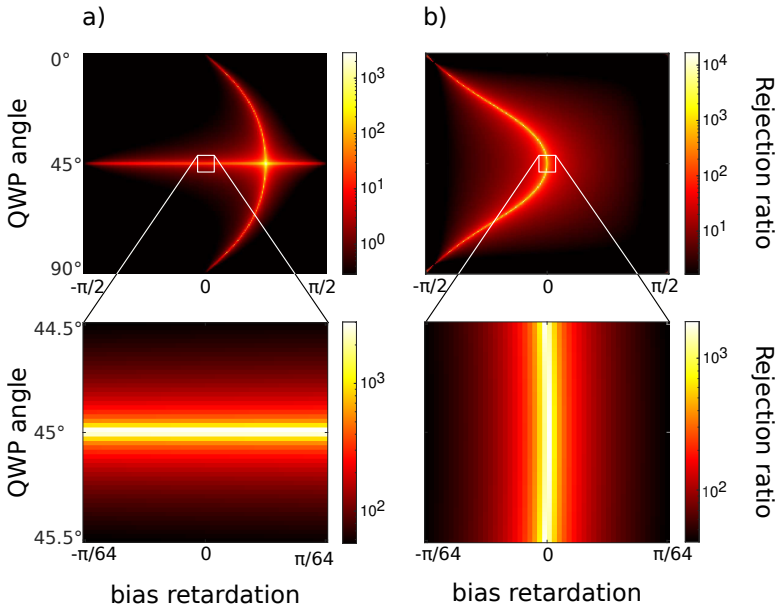

Figure 3.2: Calculated rejection ratio of (a) $LD_{\perp}$ and (b) $LD_{\swarrow}$ as a function of EOM bias retardation and QWP orientation. The zoom-in in the lower panel shows that in the region where $LD_{\perp}$ and $LD_{\swarrow}$ are both large, the rejection ratio is only dependent on one parameter, either bias voltage for $LD_{\perp}$ or QWP orientation for $LD_{\swarrow}$.

$LD_{\perp}$ or $LD_{\swarrow}$ and CD. In our model we take into account imperfections of all retarding elements, including the QWP and the bias and amplitude of retardation by the PEM and the EOM. The detailed mathematical representation is discussed in the SI.

Figure 3.2 shows a map of the calculated rejection ratio in our dual-modulation configuration as a function of EOM bias retardation (static linear birefringence) and QWP's orientation. Large rejection ratios for both $LD_{\perp}$ and $LD_{\swarrow}$ are important, especially when measuring anisotropic plasmonic particles, e.g. quasi-spherical nanoparticles (NPs) and nanorods (NRs), that can exhibit linear dichroism which is up to two orders of magnitude stronger than their circular dichroism. The lower left panel of figure 3.2 shows that the $LD_{\perp}$ rejection ratio is strongly dependent on the QWP rotation but nearly independent of the bias retardation while the lower right panel shows that $LD_{\swarrow}$ is almost independent of the QWP rotation but strongly dependent on the bias retardation. This result indicates that bias retardation and QWP rotation can be used to tune the rejection ratio of $LD_{\perp}$ and $LD_{\swarrow}$ independently.

3.2.2. Experimental results

The experimental calibration scheme of the rejection ratio is illustrated in figure 3.1. By inserting the calibration insert we can quantify and tune the setup's experimental rejection ratio of LD as described in the SI (figure S3.1). Using the calibration insert we find that our setup has a LD rejection ratio of at least 200 at all angles of the polarizer, which for

most samples we work with is a good enough value to exclude any artefacts induced by LD. It means that if the object we want to study exhibits LD that is 200 times stronger than its CD, then the artefact signal generated by the cross talk would be as large as the intrinsic CD signal. Our calibration experiments yielded a rejection ratio roughly one order of magnitude worse than the rejection ratios we find in our simulations ($\sim 10^3$). We attribute this discrepancy to the finite beam aperture of the heating laser beam and the thereby resulting spatially inhomogeneous phase retardation of the heating beam in the EOM. In later PT measurements with Koehler illumination, however, as we only use the center of the heating beam to excite the small nanoparticle, the real rejection ratio is expected to be be significantly better than the rejection ratio found upon calibration.

Aluminium nanorods

To demonstrate the strength of our technique, especially regarding the distinction between CD and LD, we have performed measurements on a purpose-tailored sample. The sample consists of nano-fabricated aluminium nanorods, designed such that they absorb the $532\,\mathrm{nm}$ pump laser strongly along their long axis, but weakly along the short axis [24], thereby exhibiting a strong LD. Aluminium NRs have higher LD g-factors than gold ones at our heating wavelength of $532\,\mathrm{nm}$ because the UV interband transitions of aluminium do not damp the visible plasmon resonance, in contrast to the case of gold [25]. The rods are immersed in toluene to provide high PT contrast. The measurement results are shown in

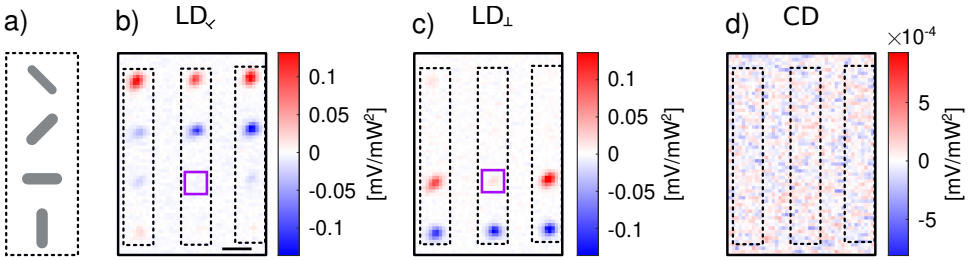

Figure 3.3: LD and CD scans of 12 aluminium NRs (size $100\times40\,\mathrm{nm}^2$, thickness $60\,\mathrm{nm}$) exhibiting strong linear dichroism. (a) illustrates the spatial orientation of the rods. (b-d) show $\mathrm{LD}_{\swarrow}$, $\mathrm{LD}_{\perp}$ and CD scans, respectively. The phase-sensitive detection enables the determination of the NRs absolute orientation via the amplitudes' sign. The absence of any observable signal in the CD measurement (d) proves the strong rejection of LD signals. The weaker residual signals in the $\mathrm{LD}_{\swarrow}$ and $\mathrm{LD}_{\perp}$ scans are due to a slight misalignment of the sample with respect to the polarization modulator axes. The square box indicates a nanorod with a reduced absorption due to a fabrication fault. The scale bar is $2\,\mu\mathrm{m}$. The probe beam intensity was $2\,\mathrm{mW}$ and the heating beam intensity was $11\,\mathrm{mW}$, measured at the entrance of the objective.

figure 3.3. We find that the NRs exhibit the expected large $\mathrm{LD}_{\perp}$ and $\mathrm{LD}_{\swarrow}$ amplitudes and that the CD signal amplitude, if there is any, is buried below the noise. This result proves that our method can discriminate the effect of CD and LD with virtually no cross talk and thereby facilitates the artefact-free measurement of samples with very weak CD. We find a rejection ratio of 313 ±9 for $\mathrm{LD}_{\perp}$ and 340 ±11 for $\mathrm{LD}_{\swarrow}$, respectively. As mentioned above, these values are significantly higher than the one found upon calibration (200), and are consistent with our calibration measurement using the entire beam aperture, whereas the nanoparticle measurement only makes use of the very center of the beam, with presumably smaller polarization imperfections. Here we assume that the NRs are perfectly achiral ob-

jects. Although this assumption holds true for ideal nanorods, fabrication errors could give rise to residual CD. In our CD measurements we do not find any measurable CD signal. Based on the SNR we can therefore give an upper bound of 3×10^{-3} for the g-factor of these rods.

CD and LD measurements at three different wavelengths

So far we have shown CD measurements only at a single wavelength. To retrieve useful structural information of a sample of interest one should record its full CD spectrum. As we had no access to a tunable heating laser with the required power, we instead used three lasers at different wavelengths, $450\,\mathrm{nm}$, $532\,\mathrm{nm}$ and $660\,\mathrm{nm}$, to show that our technique is compatible with spectral measurements. Although the EOM's retardance is strongly dependent on the beam parameters (width and pointing angles), we found our alignment method robust enough to overlap the different laser beams by means of flippable mirrors, while still keeping excellent rejection ratios. Figure 3.4 shows measurements of 100-nm-diameter quasi-spherical gold nanoparticles at three different wavelengths. For each wavelength we performed a full analysis of the absorption of the nanoparticles including isotropic absorption, linear dichroism and circular dichroism. The scans shown in figure 3.4 contain measurements of two single particles and one small cluster of particles. At a heating beam

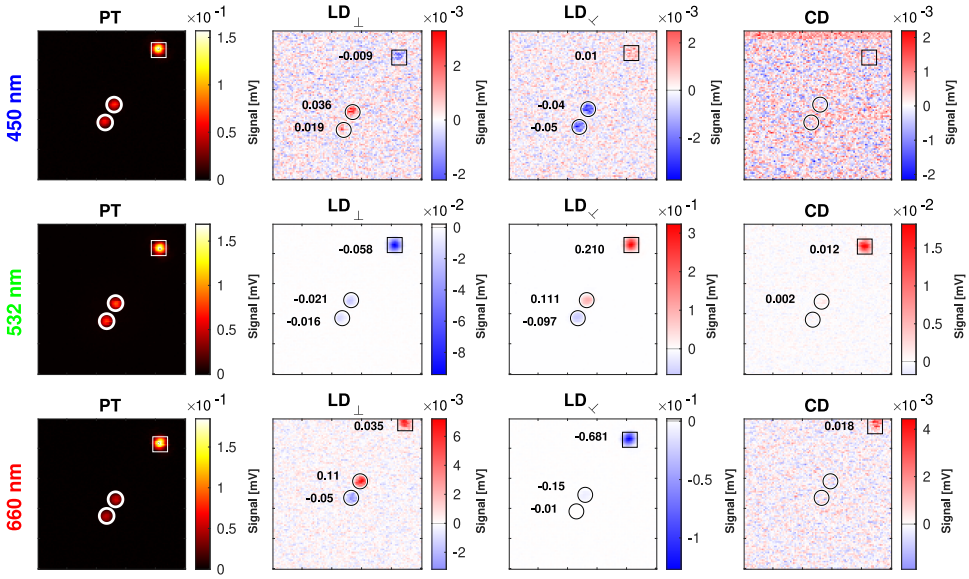

Figure 3.4: Photothermal (isotropic absorption), $\mathrm{LD}_{\perp}$, $\mathrm{LD}_{\swarrow}$ and CD measurements of spherical gold nanoparticles at three different wavelengths ($450\,\mathrm{nm}$, $532\,\mathrm{nm}$, $660\,\mathrm{nm}$) of the heating beam. The numbers indicated in $\mathrm{LD}_{\perp}$, $\mathrm{LD}_{\swarrow}$ and CD images are the averaged g-factors for each spot. A histogram of CD values for several particles is displayed in figure S3.6. The brightest particle in the PT image (square box in the upper right corner) is a dimer or trimer of nanoparticles (see figure S3.5 for more CD and LD measurements on such a dimer). The probe beam intensity was $6\,\mathrm{mW}$ throughout the entire experiment. The respective heating powers were $0.6\,\mathrm{mW}$ at $450\,\mathrm{nm}$, $5\,\mathrm{mW}$ at $532\,\mathrm{nm}$ and $8\,\mathrm{mW}$ at $660\,\mathrm{nm}$, measured at the entrance of the objective.

wavelength of $450\,\mathrm{nm}$ we find the particles to have both weak linear dichroism and weak

circular dichroism. This observation fits with our expectation that the interband transitions of gold strongly damp plasmonic behaviour at that wavelength, and therefore that polarization dependence is weak at this wavelength. We find relatively strong linear dichroism for both $532\,\mathrm{nm}$ and $660\,\mathrm{nm}$ heating wavelengths. This residual LD can be explained by small protrusions of the particle along one or more axes that may have formed during synthesis. Depending on the axis along which the particle is excited, one observes a different plasmon resonance wavelength and therefore linear dichroism. Notably, the particle with the strongest PT signal most likely corresponds to a dimer or trimer of nanoparticles. This cluster has a much stronger g-factor in LD than the single particles. If two nanoparticles are very close together they couple plasmonically and the degeneracy of the plasmons of the two nanoparticles may be lifted to yield two longitudinal modes, a symmetric and an antisymmetric mode, whereas the transverse plasmon resonances are not much affected. The symmetric longitudinal mode can be considerably red-shifted from the transverse mode [26]. This plasmon coupling can lead to the relatively strong LD in our measurements at both wavelengths.

The images of the single particles are barely visible in the CD scans, but the cluster shows a clear CD signal, which probably also arises from plasmonic coupling [27, 28]. The limited power of the $450\,\mathrm{nm}$ and the $660\,\mathrm{nm}$ lasers in these measurements prevented us from measuring g-factors smaller than 10^{-3}. From the strength of the PT signal at $450\,\mathrm{nm}$ and from the low CD value, we hypothesize that the cluster is composed of two or three particles. These results prove that our technique can in principle be extended to obtain the spectral dependence of CD, provided one has access to a tunable laser with sufficient power ($\sim 10\,\mathrm{mW}$ in the sample plane). The main factor that could hamper compatibility with spectral measurements in our technique is the wavelength dependence of the retarding elements. By using Koehler illumination for the heating beam we are relatively insensitive to chromatic aberrations of the lenses. However, to ensure good cancellation of cross talk between LD and CD, it is of utmost importance to ensure the correct retardance of the polarization optics. Both the EOM's and the PEM's retardance can be adjusted easily to deliver the required maximum modulation phase of $\pi/2$ for each wavelength. The QWP in use, although it is a superachromatic one, exhibits a slight dependence of its retardance on wavelength. One solution would be to compensate the wavelength dependence by making use of a liquid crystal retarder with adjustable retardance. We found that, by combining the aforementioned slight rotation of the QWP with an adjustment of the EOM bias retardation, it is possible to use a superachromatic or simply achromatic waveplate while achieving similar rejection of LD-to-CD cross talk.

Thanks to its good sensitivity and to its compatibility with spectral measurements, we foresee a great potential of our technique in the study of single plasmonic particles, including those having CD and LD bands in the near-IR range. A super-continuum laser or a Ti:Sapphire laser could conveniently provide a large spectral range while still delivering enough heating power for measuring CD g-factors down to the few 10^{-4} level. Heating in the near-IR would best be combined with a probe at even more red-shifted wavelength. We think that the technique is compatible with a transmission geometry [29, 30], which would allow one to probe in the mid-IR. In that case one can use near-IR optimized refractive objective for heating and a reflective objective for the probing. Compared to more conventional techniques based on scattering or extinction, our absorption-based detection can measure CD signals of single nanoparticles with excellent signal-to-noise ratio [5, 12, 31].

Gold nanoparticles immersed in a chiral liquid

We have characterized our setup's performance in terms of rejection of unwanted effects such as the leakage of linear dichroism or residual intensity modulation of the polarization modulators. These steps were necessary to make sure that we have the sensitivity to measure CD g-factors of single nanoparticles in the few 10^{-4} range, while at the same time avoiding cross talk induced by LD. In the experiments reported below, we wanted to investigate the very small circular dichroism of nominally achiral nanoparticles induced by a chiral liquid surrounding the particle [32]. The effect, referred to as PCCD (plasmon-coupled circular dichroism), may facilitate the detection of chirality of biomolecules in the visible, where most biomolecules have no absorption band [8]. According to the theoretical model presented in references [32, 33] PCCD has two components, one due to enhanced absorption of the molecule in the near field of the plasmonic particle, and the second one due to chiral currents induced in the nanoparticle by the molecular dipole. In the present case, the chiral liquid does not absorb in the visible, and only the latter component is left, which corresponds to heat dissipation by the particle (at the plasmon resonance, the particle's absorption dominates molecular absorption anyway).

In their more recent work, Yoo et al. [34] presented a solution of Maxwell's equations in circular bases, dubbed chiral Mie theory. They concluded that spherical gold nanoparticles, when immersed in a pure chiral liquid, can exhibit a measurable circular dichroism in the region of the particles' plasmon resonances. So far, none of the available experimental methods has been sensitive enough to detect the small PCCD signal of a single nanoparticle. Although Zhang et al. [5] have demonstrated CD measurements on single clusters of nanorods, the sensitivity limit of their technique could not resolve CD g-factors far below 10^{-1}. The sensitivity of photothermal CD, however, reaches down to g-factors of a few 10^{-4}, and might enable us to probe the magnitude of PCCD. To investigate the system proposed by Yoo et al., we spin-coated $100\,\mathrm{nm}$ spherical gold nanoparticles on a glass surface, and glued this sample onto a half-open channel to form a flow cell. We then performed measurements on the same single nanoparticles with two different liquids as photothermal media. These liquids were the pure enantiomers of carvone (pure S-carvone and pure R-carvone). For each liquid we performed isotropic absorption measurements.

Figure 3.5 shows absorption (a) and circular dichroism scans (b) of the same single nanoparticle surrounded by the pure enantiomers of opposite handedness and in (c) the corresponding calculated CD g-factors of each measurement. The measurements were carried out with a heating wavelength of $532\,\mathrm{nm}$. We find that the particle initially exhibits weak CD (see figure 3.5(c)) when immersed in S-carvone. To find out whether this initial CD is due to geometric distortions of the particle itself or due to CD induced by the chiral liquid (PCCD) we flush the sample cell with R-carvone which is of opposite handedness and perform another set of absorption measurements. The PT signal, which represents the isotropic absorption of the particle, remains practically unchanged (3.5(a) S1 and R1). If the initial CD signal was due to the chiral liquid then its sign should change upon reversal of the liquid's handedness. We find, however, (3.5(c)), that the change of CD is negligible within noise. That means that the measured CD is due to geometric chirality of the particle itself and, more importantly, that the chiral liquid does not alter the particle's CD by more than a g-factor of 3×10^{-4}. Repeating the experiment by measuring in both liquids again (measurements S2 and R2) reproduces our findings that the changes of CD signals are within noise.

We confirm the absence of residual leakage of LD into CD by performing LD reference measurements which are shown in figure S3.6. The residual leak of LD, considering our rejection ratio of 300 is one magnitude smaller than the measured CD signal and can therefore be safely neglected. We want to note here that the sensitivity of the measurements was limited due to heating-induced reshaping of the particles [35–37]. In order to avoid reshaping, we had to use heating powers below 20 mW. Higher powers cause long term changes of the PT signal as shown in figure S3.7. The results of Yoo et al. [34] predict a differential

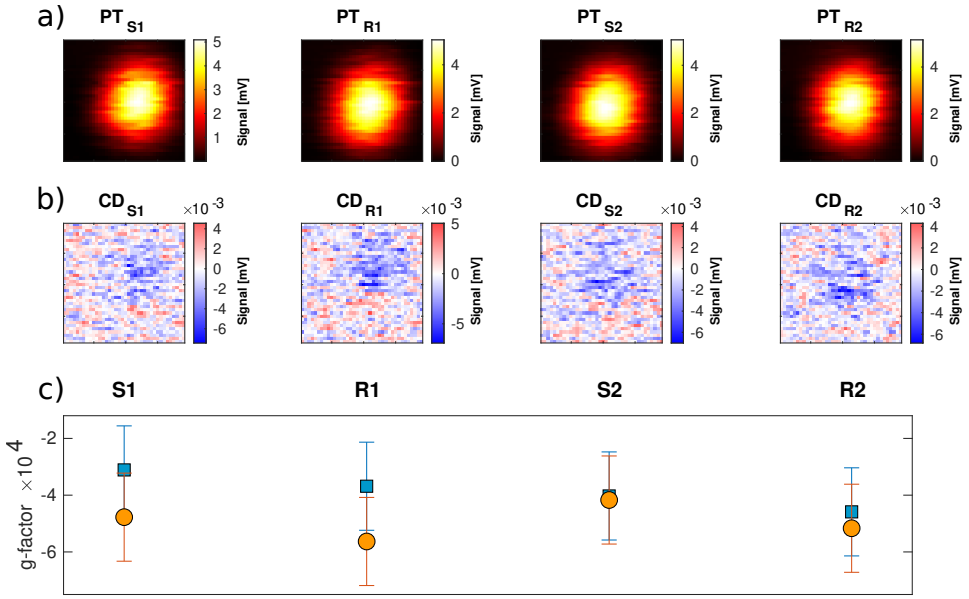

Figure 3.5: Photothermal (a) and photothermal circular dichroism (b) measurement of a single 100 nm diameter spherical gold nanoparticle immersed in the two pure enantiomers of the carvone molecule (S carvone and R carvone). (c) shows the corresponding g-factors of the scans. We employed two methods to calculate the g-factor. For the blue data points we use all pixels of the scan, for the orange data points we use a 20×20 pixel array around the centroid position of the corresponding PT scan. The heating beam intensity was 17 mW and the probe beam intensity was 2.5 mW

absorption of about 10^{-2} for a liquid with a large circular birefringence (CB) of 10^{-2}. The circular birefringence of carvone corresponds to a difference in refractive indices for circular polarization of about 10^{-4} [38, 39]. Scaling the results of Yoo et al. linearly with CB, we therefore expect an induced CD of about 10^{-4} in carvone, in good agreement with the estimations of reference [33]. This value is below, or close to our detection limit. Therefore, despite our improved sensitivity, we are not able to report any measurable PCCD effect for a gold nanoparticle in carvone heated with 532 nm. Reshaping of the particle, laser-induced chemical reactions [40] and instabilities or drifts of our optical setup set a limit to our detection sensitivity of PCCD (see SI, Sec. "Heat-induced reshaping"). To improve on this result, one could consider using other shapes of plasmonic particles, such as nanorods or nanocubes, which present a stronger dependence of absorption on the surrounding refractive index due to their sharper plasmon resonances. These particles, however, are even more

prone to reshaping than quasi-spherical particles [35]. The lower powers needed to avoid reshaping would lower the photothermal sensitivity. Another strategy would be to enhance PCCD by choosing a surrounding medium with a larger circular birefringence. Alternatively, we might be able to improve the measurement sensitivity further by employing more efficient contrast mechanisms, as recently demonstrated in refserences [41–43]. This would allow us to observe g-factors down to the 10^{-4} range while at the same time substantially decreasing the heating and therefore avoiding reshaping.

3.3. Conclusion

We have improved our previously reported PTCD microscope [15] by the addition of dual modulation of the polarization and of a QWP. We achieved CD measurements with excellent rejection of artefacts induced by vibrations, residual amplitude modulation, residual linear birefringence, and we removed leakage of linear dichroism into circular dichroism down to below our detection limit. Compared to our previous single square-wave modulation scheme [15], we suppressed these artefacts by nearly two orders of magnitude. Additionally, by means of a set of static birefringent elements, we can retrieve the full polarization dependence of a single particle's absorption. Our simulations provide a simple tool to understand how to optimize modulation parameters to avoid, or to compensate for, residual depolarizing effects of the optics. We have experimentally demonstrated the rejection of LD leakage into CD by more than a factor of 200 allowing us to measure weak CD signals of single quasi-spherical gold nanoparticles with a high sensitivity down to 3×10^{-4} in g-factors. Furthermore, we also show the capability of the method to perform spectral CD measurements. Studying nominally achiral plasmonic nanoparticles in a chiral liquid environment, we could not detect any significant plasmon-induced transfer of chirality from the liquid to the particle. We therefore find a PCCD upper bound of a 3×10^{-4} for our sample at $532\,\mathrm{nm}$. This g-factor sensitivity applies to $100\,\mathrm{nm}$ gold particles. We can translate it into a difference of absorption cross section of $\sim6\,\mathrm{nm}^2$, independent of particle size at a fixed heating power. Smaller gold particles, however, would allow higher heating intensities, giving rise to higher sensitivities. Plasmonic systems like single particles with more complex shapes or dimers of nanoparticles may turn out to be better candidates to investigate the weak PCCD effects.

3.4. Methods and experimental

3.4.1. Experimental setup

A schematic of the experimental setup is shown in Figure S3.1. More details about the setup can be found in chapter 2. In comparison to our previous setup (which contained a single modulator, electro-optic modulator (EOM)), a second polarization modulator (photo-elastic modulator (PEM)) was added to perform dual modulation of the polarization. The EOM and PEM were sinusoidally driven at modulation frequencies 23.5 kHz and 50 kHz, respectively. In addition we have used two circular birefringent plates, CB_{90} and CB_{45} which rotate the linear polarization by $90°$ and $45°$, respectively. The heating beam diameter was $\sim 1\,\mathrm{mm}$, when propagating through the polarization modulators

3.4.2. Data analysis

g-factors for each single gold nanopshere in figure 3.4 were calculated as ratios of mean values of photothermal and photothermal circular and linear dichroism signals averaged in an area of 7×7 pixels^2 around the centroid of each spot. g-factors for the gold nanosphere in figure 3.5 were caclulated in an area of 20×20 and 38×38 pixels^2 around the centroid position, respectively. The rejection ratio of the aluminium nanorod measurements was calculated taking the mean value of a 5×5 pixel area centered around the maximum values of the respective $LD_{\perp}$ and $LD_{\diagup}$ measurements and dividing it by the noise standard deviation of the same region in the CD image.

3.5. Supplementary information

3.5.1. Stokes representation of polarization

The Stokes parameters of polarized light are usually employed when describing partially polarized light and thus allow for a more general treatment than the Jones calculus representation of polarization. Here, even though we only deal with fully polarized light, we still introduce the Stokes definition of polarization as it provides a convenient expression of polarization states in terms of the four Stokes parameters, which are defined as

$$S_0 = \langle E_x^2 + E_y^2 \rangle$$
$$S_1 = \langle E_x^2 - E_y^2 \rangle / S_0$$
$$S_2 = \langle E_x E_y cos(\delta) \rangle / S_0$$
$$S_3 = \langle E_x E_y sin(\delta) \rangle / S_0$$

E_x and E_y are the respective x and y components of the electric field and δ is the phase difference of the two components. With this definition we have

- horizontal polarization if S_1 = 1
- vertical polarization if S_1 = -1
- linear 45° polarization if S_2 = 1
- linear -45° polarization if S_2 = -1
- right circular polarization if S_3 =1
- left circular polarization if S_3 = -1

3.5.2. Experimental alignment procedure

In this section we will give a description of the alignment procedure of the heating arm of our dual-modulation setup. The heating part of the setup, the one that is polarization-modulated, is illustrated in figure S3.1. It consists of two polarization modulators, an EOM and a PEM. A set of static birefringent elements, QWP, CB_{45} and CB_{90} changes the measurement mode

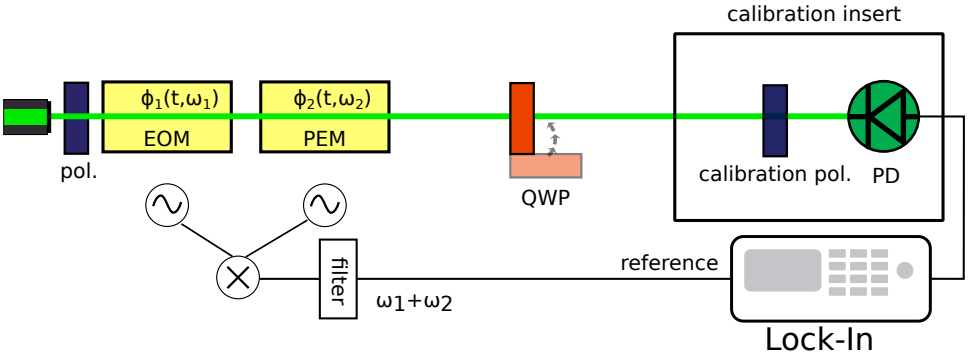

Figure S3.1: Heating arm of the dual modulation setup. The polarization modulation is performed by an EOM and a PEM, followed by a set of static retarders (QWP, CB_{45} and CB_{90}). A calibration unit composed of a rotatable polarizer and a fast photodiode is inserted for alignment of the polarization modulation. The configuration illustrated here, with the QWP inserted, corresponds to the mode sensitive to circular dichroism (CD-sensitive).

of the setup and allows us to measure different absorptive properties as explained in section 3.1. After the birefringent plates we add a calibration unit consisting of a rotatable polarizer and a fast photodiode. The photodiode's output is sent to a lock-in amplifier which is referenced to the sum frequency of the two modulators.

The purpose of the alignment procedure is to make the setup sensitive to one of the following absorptive properties, isotropic absorption, linear dichroism (LD), and circular dichroism (CD), while as much as possible reducing cross-talk between these properties. Plasmonic nanoparticles can in principle exhibit both linear dichroic and circular dichroic behaviour. In samples consisting of plasmonic nanoparticles, the LD is often much larger than the respective CD. When we aim to measure the CD of such particles, we should therefore take great care to avoid any leakage of the much stronger LD into the weak CD signal. In chapter 2 we used a single, square-modulation scheme of the polarization, performed by an EOM. We aimed to modulate between purely left and purely right circular polarization. In principle, a square wave modulation of the polarization is an ideal scheme to measure circular dichroism, as it completely avoids linear polarization states. However, this scheme requires a virtually perfect square-wave modulation of the polarization. This is practically not feasible when performing the modulation at high frequencies (>10 kHz), in particular due to bandwidth limitations of the electronics and piezoelectric behaviour of the EOM crystal. Any imperfection of the square-wave pattern can lead to a cross talk of LD and CD, thereby creating artefact signals. Secondly, the EOM, on top of the polarization modulation, also performs a slight modulation of the intensity. This effect is called residual amplitude modulation (RAM) [16] and it will induce an artefact signal for any absorbing particle.

To avoid both effects, the cross talk between LD and CD as well as the RAM, we exploited past developments in the field of CD spectroscopy [10, 22, 23], where two or more polarization modulators are used simultaneously to analyze different combinations of the driving frequencies of the two modulators, thereby giving access to various sample properties. We perform lock-in detection and thus only measure at a single frequency. But we still benefit of the two-modulator scheme if we perform our measurement at the sum (or

difference) frequency of the two modulators. We will describe in section 3.5.3 how to measure different absorptive properties at the sum frequency of the two modulators by using different static retarders placed after the modulators. At the sum frequency the modulators' individual residual amplitude modulation is of second order in these small effects, and can be neglected. In the following we will describe an alignment procedure that solves the problem of cross talk between LD and CD. Here we also benefit from the two-modulator scheme as it provides additional tuning parameters that allow us to remove cross talk better.

We concluded from the measurements in chapter 2, that a perfect square-wave modulation of the polarization by the EOM is not feasible and therefore we use a sinusoidal modulation of the polarization. Because of its mechanical resonance, the PEM only provides sinusoidal modulation. In both cases, the retardance created by each individual modulator varies sinusoidally with time and thereby not only creates circular but also elliptical and linear polarization states. One might think that this would inevitably cause cross talk between LD and CD. However, when we choose suitable modulation parameters and perform a thorough alignment of the components we can probe all absorptive properties of a sample with negligible cross talk between them. As illustrated in figure S3.1 the dual modulation of the polarization is performed using an EOM and a PEM. The laser beam first passes the EOM, then the PEM. We found that this arrangement order of the two modulators is convenient for the rejection of LD induced artefacts, because the static birefringence of the EOM can be more easily adjusted to compensate for imperfections of the polarization optics.

Alignment protocol

The alignment procedure we developed is composed of two steps. In the first step we align the fast axes of all components and make their optical axes collinear with the beam propagation. As the EOM contains a thick uniaxial crystal we must carefully align its crystal axis along the laser beam. In the first alignment step we make sure that the setup gives a CD response with the proper polarization optics. The second step is dedicated to ensure a pure CD measurement of the setup, free from cross talk. Later, we will also discuss how to probe other absorptive properties. The protocol that we developed is as follows:

First, we make sure that we have a well-defined and clean linear polarization state. To this purpose, we use a Glan-Thomson polarizer (extinction ratio 10^{-5}) oriented such that we have horizontally polarized light, or in terms of Stokes parameters: $S_1 = 1$. To measure the polarization state we use a Schaeffter & Kirchhoff polarization analyzer, which conveniently displays the polarization state in terms of the Stokes parameters. After the polarizer we send the laser beam through the EOM. For the rough alignment procedure the time-dependent retardation of both modulators is turned off.

EOM alignment: We first roughly align the EOM fast axis to 45° with respect to the initial polarization. Then we align the EOM's extraordinary axis along the propagation direction according to the alignment procedure described in [44]. Finally we align the EOM's fast axis precisely at 45° with respect to the initial polarization. Assuming that we have purely horizontal linearly polarized light $S_1 = 1$ and $S_2 = 0$, if the EOM's fast axis was aligned perfectly at 45° with respect to the initial polarization, when applying a retardation along the fast axis we would not create an S_2 component but only a S_3 component of the polarization. To align the fast axis we thus measure the polarization state while applying a large static retardation and rotate the EOM along its crystal axis, until the S_2 component vanishes.

PEM alignment: The alignment of the PEM is simpler, for it consists of fused silica instead

of a uniaxial crystal, thus there is no crystal axis the beam needs to be aligned to. However, the path length of the beam through the crystal defines the phase retardation and therefore we make sure we align the surface normal of the silica plate with the propagation axis of the laser beam. The retardation amplitude of the PEM is also slightly dependent on the position where the laser beam impinges on the quartz plate. To make sure that we exert the desired retardation amplitude we manually place the PEM such that we hit the center of the quartz plate. The PEM fast axis alignment is performed similar to the EOM fast axis alignment, but while applying a dynamic retardation instead.

Alignment of QWP: After the PEM, the laser beam passes through a number of static linear and circular birefringent components that allow us to set the operation mode of the setup. To be sensitive to CD, the differential absorption of left and right circularly polarized light, we need to insert a QWP after the two modulators. The achromatic QWP (Thorlabs) is mounted in a rotational optical mount to ensure precise alignment of the fast axis. To align it we measure the polarization state after the QWP while rotating the fast axis so that the polarization state is purely circular, $|S_3| = 1$.

Alignment of CB plates: The setup contains two circular birefringent components that can change the measurement mode in case we want to measure LD. Both of them are circularly birefringent plates, made from crystalline α-quartz, with a rotatory strength of either 45° or 90° (at $532\,\mathrm{nm}$). We will later come back to explain the purpose of these plates, for now we only explain their alignment. A purely circularly birefringent component does not possess a fast axis, but the path length of the laser beam through the component defines the rotatory strength of the plate. The path length can be adjusted by tilting the surface normal of the plate with respect to the propagation direction of the laser beam. We first measure the polarization state before we insert the plates. Assuming a perfect horizontal polarization, $S_1 = 1$, before the circular birefringent plates, we get $S_2 = -1$ for the CB_{45} plate and $S_1 = -1$ for the CB_{90} plate. The procedure that we discussed so far was the rough alignment procedure. If we chose suitable combinations of the static retarding elements we would already be able to measure different properties of an absorbing sample. However, these measurements might not be free from cross talk between LD and CD. A second step of alignment is required to make it exclusively sensitive to a single absorptive property, meaning that we suppress the cross talk between LD and CD. Up to now, the time-dependent retardation of the polarization modulators was turned off. For this second step, both modulators are set to perform a non-biased sinusoidal modulation with a retardation amplitude of $\pi/2$, the EOM at frequency ω_1 and the PEM at frequency ω_2. We insert a photodiode and a rotatable polarizer (calibration polarizer), as illustrated in figure S3.1. The polarizer represents a purely linear dichroic element. The photodiode is connected to a lock-in amplifier, which is referenced to the sum frequency of the two modulators. We bring the setup to the CD-sensitive mode, which corresponds to the configuration with two modulators plus the QWP. As we modulate the polarization with both modulators, the intensity transmitted through the calibration polarizer changes as a function of time. The lock-in compares the intensity transmitted through the polarizer with the external reference $(\omega_1 + \omega_2)$ while extracting modulations occurring only at this very frequency. We shall thus call the part of the transmitted intensity that is modulated at frequency $\omega_1 + \omega_2$ our signal. If we are in CD-sensitive mode, no signal is expected when the calibration polarizer is inserted, as it is only linearly but not circularly dichroic. However, due to slight imperfections in the modulation scheme, such as misalign-

ment of the fast axes of the EOM, PEM or QWP, bias retardation of the modulators, or deviation of the QWP's retardation strength, we have to anticipate a nonzero cross talk of LD and CD and therefore also a signal. The strength of the signal measured by the lock-in, while the polarizer is inserted, is a measure of the cross talk between LD and CD. We found that we can compensate the aforementioned imperfections of the components and the alignment, thereby we reduce the cross talk. To achieve this it is sufficient to adjust two parameters, the EOM bias retardation and the QWP's fast axis.

Fine alignment procedure: First we rotate the calibration polarizer such that it transmits S_1 = 1 and we minimize the lock-in signal at the sum frequency by adjusting the EOM's bias retardation. Then we rotate the calibration polarizer to transmit S_2 = 1 and minimize the signal by adjusting the fast axis of the QWP. To understand this second alignment procedure it is important to have a closer look at LD. Linear dichroism which is defined as the differential absorption of two orthogonal polarization states is, unlike CD, dependent on the in-plane orientation of the object under study. To retrieve the full linear dichroic behaviour of an object, two measurements are necessary, one where we probe the absorption difference of S_1=1 and S_1=-1, which we shall call $LD_{\perp}$, and one where we probe the absorption difference of S_2 =1 and S_2=-1, and which we call $LD_{\measuredangle}$. When we try to avoid cross talk of LD and CD we need to make sure to avoid cross talk of both $LD_{\perp}$ with CD and $LD_{\measuredangle}$ with CD. We found that the change of the EOM bias retardation affects exclusively the cross talk between $LD_{\measuredangle}$ and CD, while the rotation of the QWP's fast axis affects exclusively the cross talk between $LD_{\perp}$ and CD, at least within a reasonable range. This behaviour is represented in figure 3.2.

Quantification of the extinction ratio

With the calibration insert, shown in figure S3.1, which is composed of the rotatable polarizer and the photodiode, we can not only tune the setup for reducing the cross talk, but we are also able to quantify this cross talk. This is especially important when measuring particles that have strong LD compared to their CD, such as plasmonic nanorods, or plasmonically coupled metal nanospheres. [45–47]. Although we achieve very high rejection of cross talk we are not able to completely eliminate it. To quantify the residual cross talk we define a rejection ratio, that tells by which factor we suppress the leakage of LD into CD. The experimental extinction ratio is defined as:

$$R_{ext}(\alpha) = \frac{LD_{pol}}{CD_{pol}}. \tag{3.2}$$

To determine the rejection ratio we need to measure the two quantities CD_{pol} and LD_{pol}. Therefore we first put the setup in $LD_{\measuredangle}$ -sensitive mode and rotate the calibration polarizer to maximize the lock-in signal. The obtained maximum value is LD_{pol}. Then we switch to CD-sensitive mode by inserting the QWP and again measure the lock-in signal. The obtained value is CD_{pol}. CD_{pol} is in general dependent on the angle of the polarizer. This indicates that there is a different amount of cross talk from $LD_{\measuredangle}$ into CD, and from $LD_{\perp}$ into CD. We typically measure a rejection of 200 at polarizer positions of $n \cdot 90°$. For polarizer positions of $45° + n \cdot 90°$ we measure a rejection ratio of $6{\times}10^4$. For our measurements we assume the worst case corresponding to the lowest rejection ratio, 200. We want to note here that this rejection ratio is mutual. If we suppress the LD leakage into CD we also suppress the leakage of CD into LD.

In case we seek to have even stronger rejection of cross talk we make use of the aforementioned CB_{90} plate as described in [22]. The CB_{90} plate rotates all linear polarization states by 90° regardless of their orientation. This effectively flips the sign of LD, while maintaining its magnitude. On the other hand, as the CB_{90} plate does not affect circular polarization states, the circular dichroism measurement is not affected. Thus, in order to even further reduce the cross talk, we can perform two circular dichroism measurements, one with and one without the CB_{90} plate. If we then average these two measurements we remove the residual LD contribution.

3.5.3. Simulations

In a dual polarization modulation scheme, the time-dependent power absorbed by a sample can be composed of many different combinations of the frequencies driving the two modulators, ω_1 and ω_2, depending on the properties of the sample under study. In this section we want to simulate the time-dependent power absorbed by a given sample using Jones matrix calculus. We then extract the frequency spectrum by applying a FFT of the absorbed power. In principle one could also perform an analytical calculation of the frequency decomposition of an arbitrary sample as presented in [23]. However, our numerical approach allows us to conveniently explore a large space of parameters, which would be tedious to calculate with an analytical approach.

Jones matrix representation of the optical components
The matrix formalism developed by Jones [48–54] provides a convenient framework for analyzing the effects of optical components on fully polarized light. The matrix representations for the different optical components were taken from references [48, 51, 54].
Rotation Matrix:

$$\mathbf{R}_\Theta = \begin{bmatrix} cos(\Theta) & sin(\Theta) \\ -sin(\Theta) & cos(\Theta) \end{bmatrix}, \tag{3.3}$$

With the rotation matrix $\mathbf{R}_\Theta$ it is possible to calculate the matrix representation of axially rotated elements. Assuming that the optical component has a matrix representation of $\mathbf{M}$ in a certain reference frame, when the component is rotated by an angle Θ in clockwise sense, then the matrix of the rotated element can be expressed as $\mathbf{M}_\Theta = \mathbf{R}(-\Theta)M\mathbf{R}(\Theta)$.
Linearly birefringent plate:

$$\Phi(\eta, \Theta) = \mathbf{R}(-\Theta) \begin{bmatrix} 1 & 0 \\ 0 & e^{i\eta} \end{bmatrix} \mathbf{R}(\Theta). \tag{3.4}$$

In the simplest case of a static birefringent plate, η is a constant value. We can model a polarization modulator with a time-dependent retardance as $\eta(t) = \eta_0 sin(\omega t) + \phi_0$, where η_0 is the retardation amplitude, ω the modulation frequency and ϕ_0 an additional static linear birefringence.
Circularly birefringent plate:

$$\mathbf{CB}_\alpha = \begin{bmatrix} cos(\alpha) & sin(\alpha) \\ -sin(\alpha) & cos(\alpha) \end{bmatrix}, \tag{3.5}$$

with α being the rotatory strength (optical activity) of the CB plate. With the above defined Jones matrices and for horizontally polarized light as input, we can write the time-dependent electric field of the polarization modulator setup that is illustrated in figure S3.1 as

$$\begin{bmatrix} E_{x0} \\ E_{y0} \end{bmatrix}(t) = \mathbf{CB}_\alpha \, \Phi_0(\eta_0, \Theta_0) \, \Phi_2(\eta_2, \Theta_2, \omega_2, t) \, \Phi_1(\eta_1, \Theta_1, \omega_1, t) \begin{bmatrix} 1 \\ 0 \end{bmatrix}, \tag{3.6}$$

where $\Phi_{1,2}$ represent the matrices of the polarization modulators and Φ_0 a static linear retarder (QWP). Often, the Jones matrix approach is used to calculate the light transmitted

through a sample. This approach represents the CD measurements performed with commercial CD spectrometers well, as they measure the transmission of a dilute solution of molecules in a cuvette. The measurements that we perform, however, are true absorption measurements and therefore require a different matrix representation of the samples in terms of absorption. This representation has been described by Jones in [54]. The different absorptive properties of a sample can be modeled as follows:

Isotropic absorber:

$$\mathbf{u} = \kappa \begin{bmatrix} u & 0 \\ 0 & u \end{bmatrix}, \tag{3.7}$$

with κ being the amplitude absorption coefficient.

LD$_\perp$ absorber:

$$\mathbf{ld}_\perp = \mathbf{p}_\perp \begin{bmatrix} 1 & 0 \\ 0 & -1 \end{bmatrix}, \tag{3.8}$$

with p$_\perp$ being half the difference of the two principal absorption coefficients.

LD$_\measuredangle$ absorber:

$$\mathbf{ld}_\measuredangle = \mathbf{p}_\measuredangle \begin{bmatrix} 0 & 1 \\ 1 & 0 \end{bmatrix}, \tag{3.9}$$

with p$_\measuredangle$ being half the difference of the two principal absorption coefficients.

CD absorber:

$$\mathbf{cd} = \delta \begin{bmatrix} 0 & -i \\ i & 0 \end{bmatrix}, \tag{3.10}$$

with δ being half the difference of the absorption coefficients of left and right circular polarization. With the definitions for the samples given in equations 3.7-3.10 it is possible to represent an absorber exhibiting various absorptive properties by just adding the respective sample matrices. Assuming the particle under study behaves as a dipole, the time-averaged power absorbed by the particle can be expressed as

$$\langle \mathcal{P}_{abs} \rangle(\omega_1, \omega_2) = -\langle Im\big[\vec{p}^*(\omega_1, \omega_2) \cdot \vec{E}(\omega_1, \omega_2\big] \rangle \tag{3.11}$$

with

$$\vec{p} = \overset{\leftrightarrow}{\alpha} \vec{E} \tag{3.12}$$

where $\vec{p}$ is the dipole moment and $\overset{\leftrightarrow}{\alpha}$ the polarizability tensor of the absorbing dipole [55]. When we refer to the time average we imply time average over the optical frequencies, but not the frequencies of the polarization modulators, this is indicated by the (ω_1, ω_2) dependence. In general, when performing a transmission assay, one would measure the extinction and not the absorption, in which case one also would need to take the real part of the polarizability into account. In photothermal microscopy, as we perform a true absorption measurement, we must only take the imaginary part of the polarizability into account [56], which can be expressed by linear combinations of equations 3.7-3.10.

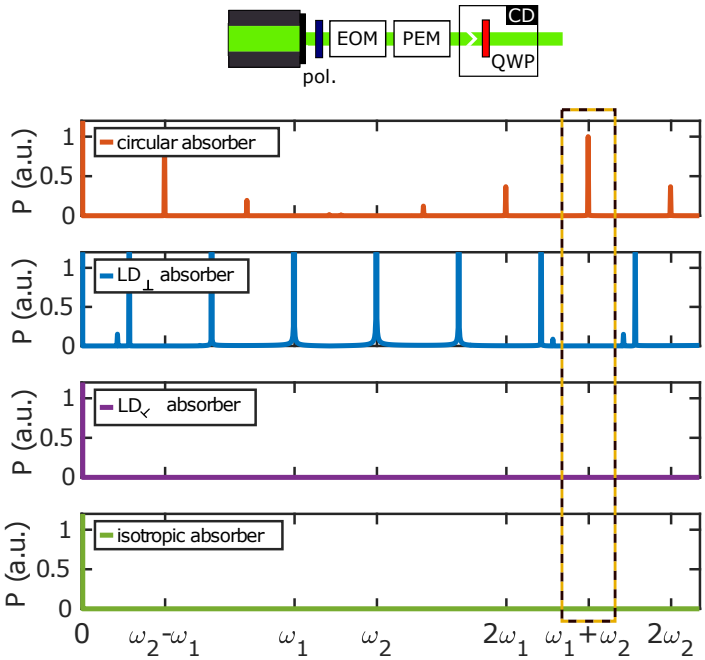

Figure S3.2: Spectrum of the absorbed power of the four different absorbers, exhibiting either only CD, $LD_{\perp}$, $LD_{\swarrow}$ or isotropic absorption, under dual polarization modulation in CD-sensitive mode. We normalize the power to 1 for the circular absorber at the sum frequency ω_1+ω_2.

Simulated FFT spectra of different absorbers

In our simulations we investigate the time-dependent absorbed power of samples exhibiting different absorptive properties. We first calculate the absorbed power, according to equation 3.11, for the four different absorptive properties defined in 3.7-3.10, and plot it in the frequency domain by applying a FFT. Figure S3.2 shows the frequency spectra of four absorbers exhibiting either pure CD, pure $LD_{\perp}$, pure $LD_{\swarrow}$ or pure isotropic absorption. The spectra are calculated for the CD - setup configuration. For the differential absorptivities we choose δ=10^{-3}, $p_{\perp}$ and $p_{\swarrow}$ =5×10^{-2} and κ=0.5. In CD mode, if we extract the signal at the sum frequency ω_1+ω_2, we only have a contribution from the circular dichroic sample. If we want to measure the other absorptive properties at the sum frequency we have to change the mode of the setup as discussed in section 3.5.2. In our computational model this is done by modifying the components of equation 3.6. Figure S3.3(a) shows the spectrum of the absorbed power of the same set of absorbers in $LD_{\perp}$ sensitive mode. We can indeed observe that the linear dichroic absorber $LD_{\perp}$ has a component at ω_1+ω_2. Likewise figure S3.3(b) shows the power spectrum of the same set of absorbers now in the $LD_{\swarrow}$ sensitive mode. As expected only the $LD_{\swarrow}$ absorber has a component at the sum frequency ω_1+ω_2. Note that in all three cases (figures S3.2 and 3.3), the isotropic absorber only shows constant absorption (at f = 0), which is also expected as we do not perform intensity but only polarization modulation. Until now we have only considered ideal conditions, in which we

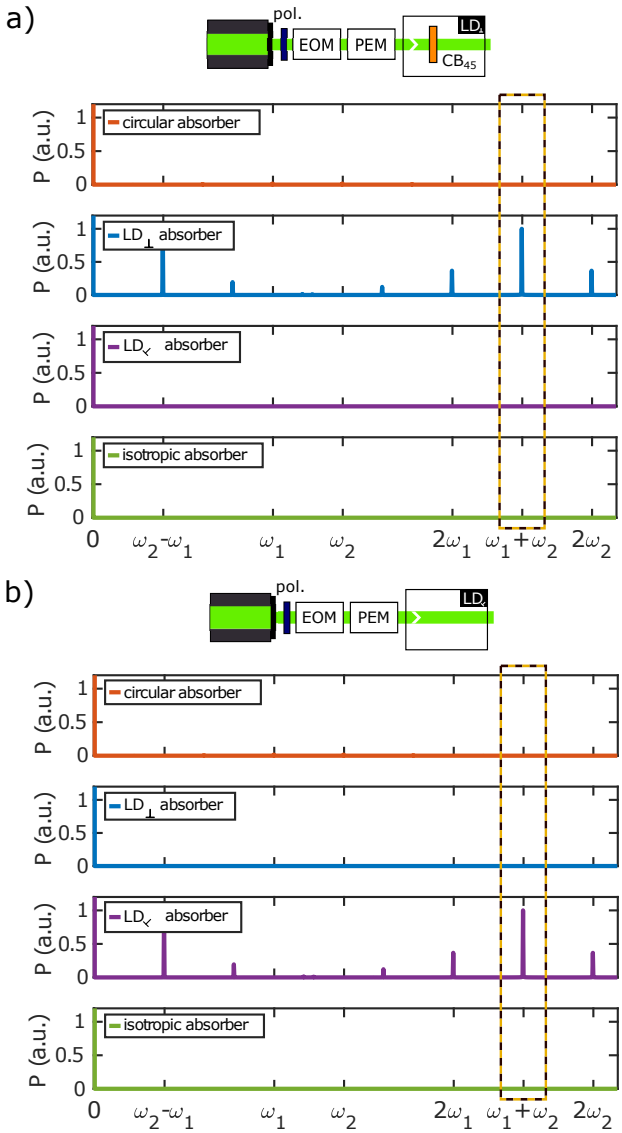

Figure S3.3: Spectrum of the absorbed power of the four different absorbers, exhibiting either CD, $LD_{\perp}$,$LD_{<}$ or isotropic absorption, under dual polarization modulation. In (a) for $LD_{\perp}$ sensitive and (b) $LD_{<}$ sensitive mode. We normalize the power to be 1 for (a) the $LD_{\perp}$ absorber and for (b) $LD_{<}$ the absorber, at the sum frequency $\omega_1+\omega_2$.

can easily ensure zero cross talk between LD and CD, and there is no artefact signal due to residual amplitude modulation. In a real setup we have to consider imperfections of the optical components themselves as well as slight misalignment of the various components.

Owing to our numerical approach we can easily simulate the effect of these imperfections. These imperfections will have an effect on the spectrum of the absorbed power and introduce a cross talk between the different absorptive properties. To illustrate the influence of one particular configuration we now introduce the following set of imperfections:

- EOM residual intensity modulation of 10^{-3}
- PEM residual intensity modulation of 10^{-3}
- PEM fast axis misalignment of 0.5°
- QWP deviation of $\pi/200$ from $\pi/2$ retardation

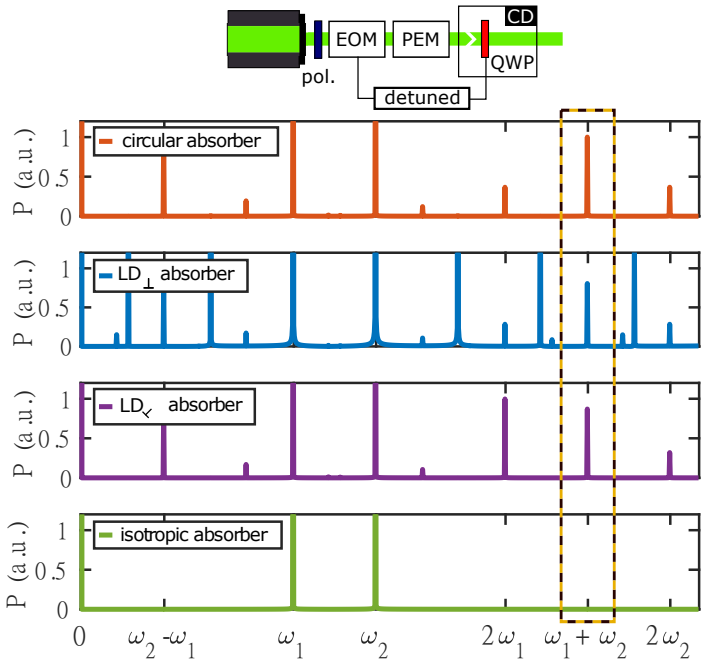

Figure S3.4: Spectrum of the absorbed power of the four different absorbers, under dual polarization modulation with additional imperfections of the modulation scheme, which lead to cross talk of linear and circular dichroism. We normalize the power to be 1 for the circular absorber at the sum frequency $\omega_1+\omega_2$.

In case the g-factor of CD and LD in a sample is of the same order of magnitude, small imperfections would not have a great impact on the CD measurement. However, when investigating the CD of plasmonic nanoparticles such as nanorods, the effect of LD can be much stronger. Therefore, in our simulations, we set the CD to be a factor of 50 weaker than the LD. Figure S3.4 shows the power spectrum in CD-sensitive mode under the aforementioned imperfections of the polarization modulation. In this case, also the $LD_{\perp}$ as well as the $LD_{\swarrow}$ show power absorption at the sum frequency, indicating a cross talk of LD into CD. As opposed to figures S3.2-S3.3 here the isotropic absorber shows a frequency

component at ω_1 and ω_2 which is due to the slight residual intensity modulation of the polarization modulators. The set of imperfections that we have used here is just one single example, other combinations are possible depending on the alignment and the individual components. In general there can also be more sources of imperfections induced by other optical components that we have not discussed so far for simplicity. These can be additional optical components in the beam path. We found that with the alignment protocol described in the above sections we can compensate also for small birefringent and dichroic effects on the polarization exhibited by these additional components.

3.5.4. CD of gold nanoparticle dimers

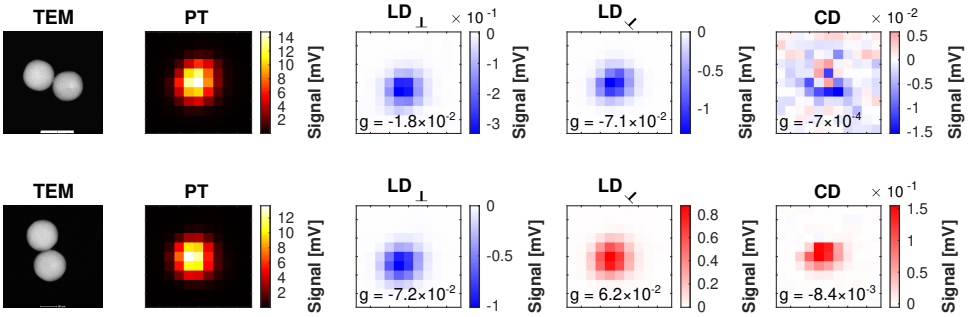

Figure S3.5: Correlated TEM images and optical measurements of two different 100 nm diameter gold nanoparticle dimers. One dimer is showing relatively strong PT CD signal, the other one shows weak CD signal. The measurements were performed at a heating wavelength of 532 nm. The scale bar in the TEM image is 100 nm.

Figure S3.5 shows correlated TEM and optical measurements of two dimer gold nanoparticles. The measurements are carried out in immersion oil as photothermal medium. One dimer exhibits relatively strong CD of 0.8%, the second particle exhibits a CD of 0.07% which is one magnitude lower. The $LD_{\perp}$ and $LD_{\swarrow}$ are both one or two orders of magnitude larger than the CD values, which probably is induced by plasmonic hybridization.

3.5.5. CD of a single gold nanoparticle in carvone with LD reference

Figure S3.6 shows absorption scans of a single gold nanoparticle. The particle was chosen such that it exhibits both weak CD and weak LD, to make sure that there is no residual leakage of LD into CD and that thermal induced reshaping does not decrease the CD over the course of the experiment shown in figure 3.5. The corresponding g-factors of LD and CD are indicated in the scans. If we take into account our previously shown LD rejection ratio of 300 we expect a residual leakage of LD into CD of not larger than 5×10^{-5} in g-factor which is one magnitude lower than the particles' actual CD g-factor.

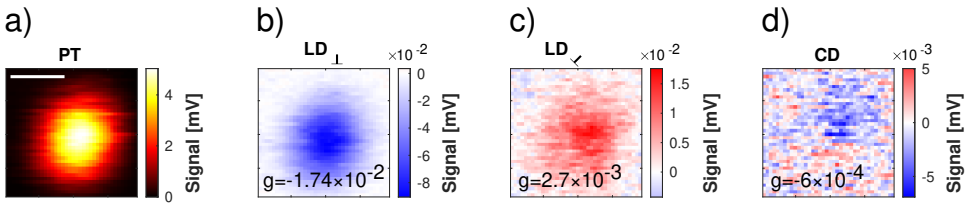

Figure S3.6: PT (a) $LD_{\perp}$ (b) $LD_{\swarrow}$ (c) and CD (d) scans of the single 100 nm diameter spherical gold nanoparticle in figure 3.5. All measurements here were carried out in R-carvone. The scale bar is 250 nm. The inserts of (b)-(d) show the respective g-factors.

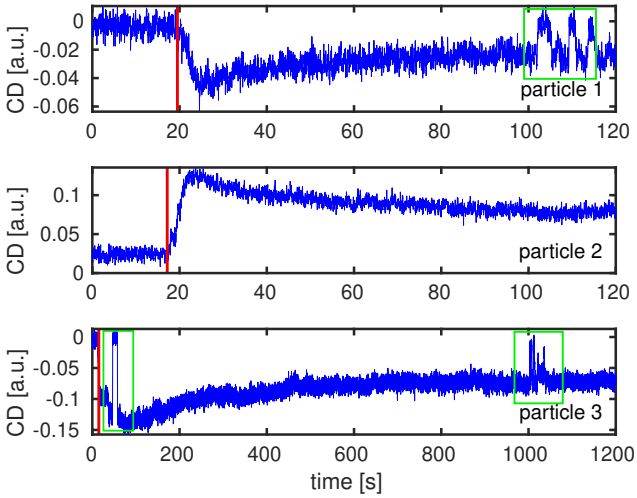

Figure S3.7: Time trace of CD measurements of three different 100 nm gold nanoparticles at high heating laser power indicating reshaping of the nanoparticles. At the beginning of each timetrace, the laser power is kept very low and after about 20 seconds, the laser power is slowly raised to the highest laser power. The highest laser power is about 30 mW, 30 mW and 40 mW for the first, second and third particle, respectively. The heating power (wavelength of 532 nm) is spread over an area of about 20 µm. We use 10 mW of probe power (laser wavelength of 815 nm) in confocal. The binning time is 30 ms. The red line indicates the time when we increase the heating laser power and green boxes indicate where we did manual refocusing to check that the decrease in signal is indeed due to the reshaping, but not due to any drift out of focus. The first green box in the timetrace for the third particle indicates when the heating laser was blocked for a short period of time.

3.5.6. Heat-induced reshaping

Figure S3.7 shows time traces of three different single gold nanoparticles. We first focus on a particle with a low laser power of few mW. After a given time, indicated by the red line in figure S3.7 we slowly increase the power of the heating beam by about 30 mW to 40 mW (Koehler illumination in the area of 20 μm^2). The green boxes indicate where we manually refocus to check that the decrease in signal is indeed due to the reshaping, but not due to the out-of-focus drifts. After the initial increase, which is due to the increase in heating power,

we observe a gradual decrease of CD signal, which is due to reshaping. Notably the CD signal does not vanish completely even after hundreds of seconds, but stabilizes at some finite value. This is probably because of the limited heating laser power in our experiments. We think that a further increase in heating laser power could induce further reshaping and lead to weaker and weaker CD signals over longer periods of laser exposure. However, the laser power cannot be increased indefinitely, as light-induced reactions were observed to take place in such complex liquids as carvone [40].

3.5.7. Nanofabrication of single aluminium nanorods

Aluminium nanostructures were fabricated in the Kavli Nanolab in Delft, using the following protocol in chronological order. Glass coverslips (borosilicate glass, diameter $25\,\mathrm{mm}$, thickness No.1) were used as substrate. First, they were cleaned by sonication in acetone and isopropanol. The substrate was dehydrated by a bake-off at $150\,^{\circ}\mathrm{C}$ for 10 minutes and in the same equipment it underwent priming with a monolayer of HMDS (Delta RC80 apparatus) to improve the hydrophobicity of the glass surface. The samples were transferred to a spin-coater and spun with CSAR positive e-beam resist (AR-P 6200.04) at $2000\,\mathrm{rpm}$ followed by a soft bake for $2\,\mathrm{min}$ on a hotplate at $150\,^{\circ}\mathrm{C}$. After that, the CSAR layer was covered with $11\,\mathrm{nm}$ of chromium through e-beam evaporation, to form a conducting layer on top of the samples and to prevent charging of the substrate during e-beam patterning. The samples were e-beam exposed with a pattern that contained arrays of aluminium rods. The dimensions of the rods were $40\times100\,\mathrm{nm}$. Each array was exposed at a different dose, ranging from 70 to $200\,\mu\mathrm{C/cm^2}$. Eventually the optimal dose was chosen by means of the optical experiment. Next, the samples were stripped of chromium by submerging them in a Cr01 TechniEtch solution for $15\,\mathrm{s}$ and rinsing them with DI water. The samples were first developed in pentyl acetate ($1\,\mathrm{min}$), then a mixture of isopropanol and methyl-isobutyl ketone (1:1) for $1\,\mathrm{min}$ and finally in isopropanol for $1\,\mathrm{min}$. The samples were dried and subsequently residues of the developed resist were removed through a descum process by oxygen plasma etching for $30\,\mathrm{s}$ at 100 Watt power and $200\,\mathrm{sccm}$ O_2 flow. The exposed, developed and oxygen etched glass samples were then e-beam evaporated with $3\,\mathrm{nm}$ of Cr for adhesion, directly followed by $60\,\mathrm{nm}$ of aluminium. Lift-off was performed in anisole at $80\,^{\circ}\mathrm{C}$ for at least 1 hour. Finally, the samples were rinsed of all residuals in a jet of acetone followed by rinsing in a beaker with isopropanol and drying in a N_2 stream.

References

[1] Lombardi, R. A.; Nafie, L. A. Observation and Calculation of Vibrational Circular Birefringence: A New Form of Vibrational Optical Activity. *Chirality* **2009**, *21*, E277–E286.

[2] Hendry, E.; Mikhaylovskiy, R.; Barron, L.; Kadodwala, M.; Davis, T. Chiral Electromagnetic Fields Generated by Arrays of Nanoslits. *Nano Letters* **2012**, *12*, 3640–3644.

[3] Tang, Y.; Cohen, A. E. Enhanced Enantioselectivity in Excitation of Chiral Molecules by Superchiral Light. *Science* **2011**, *332*, 333–336.

[4] Schaeferling, M.; Dregely, D.; Hentschel, M.; Giessen, H. Tailoring Enhanced Optical

Chirality: Design Principles for Chiral Plasmonic Nanostructures. *Physical Review X* **2012**, *2*, 031010.

[5] Zhang, Q.; Hernandez, T.; Smith, K. W.; Hosseini Jebeli, S. A.; Dai, A. X.; Warning, L.; Baiyasi, R.; McCarthy, L. A.; Guo, H.; Chen, D.-H.; Dionne, J. A.; Landes, C. F.; Link, S. Unraveling the Origin of Chirality from Plasmonic Nanoparticle-Protein Complexes. *Science* **2019**, *365*, 1475–1478.

[6] Raziman, T.; Godiksen, R. H.; Muller, M. A.; Curto, A. G. Conditions for Enhancing Chiral Nanophotonics near Achiral Nanoparticles. *ACS Photonics* **2019**, *6*, 2583–2589.

[7] Solomon, M. L.; Abendroth, J. M.; Poulikakos, L. V.; Hu, J.; Dionne, J. A. Fluorescence-Detected Circular Dichroism of a Chiral Molecular Monolayer with Dielectric Metasurfaces. *Journal of the American Chemical Society* **2020**, *142*, 18304–18309.

[8] Maoz, B. M.; Chaikin, Y.; Tesler, A. B.; Bar Elli, O.; Fan, Z.; Govorov, A. O.; Markovich, G. Amplification of Chiroptical Activity of Chiral Biomolecules by Surface Plasmons. *Nano Letters* **2013**, *13*, 1203–1209.

[9] García-Guirado, J.; Svedendahl, M.; Puigdollers, J.; Quidant, R. Enantiomer-Selective Molecular Sensing Using Racemic Nanoplasmonic Arrays. *Nano Letters* **2018**, *18*, 6279–6285.

[10] Jellison, G.; Modine, F. Two-Modulator Generalized Ellipsometry: Theory. *Applied Optics* **1997**, *36*, 8190–8198.

[11] Jellison, G.; Modine, F. Two-Modulator Generalized Ellipsometry: Experiment and Calibration. *Applied Optics* **1997**, *36*, 8184–8189.

[12] Vinegrad, E.; Vestler, D.; Ben-Moshe, A.; Barnea, A. R.; Markovich, G.; Cheshnovsky, O. Circular Dichroism of Single Particles. *ACS Photonics* **2018**, *5*, 2151–2159.

[13] Novotny, L.; Hecht, B. *Principles of Nano-Optics*; Cambridge University Press: Cambridge, 2012.

[14] Bauer, T. Probe-Based Nano-Interferometric Reconstruction of Tightly Focused Vectorial Light Fields. **2017**,

[15] Spaeth, P.; Adhikari, S.; Le, L.; Jollans, T.; Pud, S.; Albrecht, W.; Bauer, T.; Caldarola, M.; Kuipers, L.; Orrit, M. Circular Dichroism Measurement of Single Metal Nanoparticles Using Photothermal Imaging. *Nano Letters* **2019**, *19*, 8934–8940.

[16] Whittaker, E. A.; Gehrtz, M.; Bjorklund, G. C. Residual Amplitude Modulation in Laser Electro-Optic Phase Modulation. *JOSA B* **1985**, *2*, 1320–1326.

[17] Sathian, J.; Jaatinen, E. Intensity Dependent Residual Amplitude Modulation in Electro-Optic Phase Modulators. *Applied Optics* **2012**, *51*, 3684–3691.

[18] Shindo, Y.; Nakagawa, M. Circular Dichroism Measurements. I. Calibration of a Circular Dichroism Spectrometer. *Review of Scientific Instruments* **1985**, *56*, 32–39.

[19] Shindo, Y.; Nakagawa, M.; Ohmi, Y. On the Problems of CD Spectropolarimeters. II: Artifacts in CD Spectrometers. *Applied Spectroscopy* **1985**, *39*, 860–868.

[20] Shindo, Y. On the Problems of CD Spectropolarimeter (IV) Artifacts Due to the Light Scattering by Small Particles. *Applied Spectroscopy* **1985**, *39*, 713–715.

[21] Cheng, J.; Nafie, L.; Stephens, P. Polarization Scrambling Using a Photoelastic Modulator: Application to Circular Dichroism Measurement. *JOSA* **1975**, *65*, 1031–1035.

[22] Barriel, O. A. Mueller Matrix Polarimetry of Anisotropic Chiral Media. Ph.D. thesis, Universitat de Barcelona, Barcelona, 2010.

[23] Arteaga, O.; Freudenthal, J.; Wang, B.; Kahr, B. Mueller Matrix Polarimetry with Four Photoelastic Modulators: Theory and Calibration. *Applied Optics* **2012**, *51*, 6805–6817.

[24] Knight, M. W.; Liu, L.; Wang, Y.; Brown, L.; Mukherjee, S.; King, N. S.; Everitt, H. O.; Nordlander, P.; Halas, N. J. Aluminum Plasmonic Nanoantennas. *Nano Letters* **2012**, *12*, 6000–6004.

[25] Cheng, F.; Su, P.-H.; Choi, J.; Gwo, S.; Li, X.; Shih, C.-K. Epitaxial Growth of Atomically Smooth Aluminum on Silicon and Its Intrinsic Optical Properties. *ACS Nano* **2016**, *10*, 9852–9860.

[26] Jain, P. K.; El-Sayed, M. A. Plasmonic Coupling in Noble Metal Nanostructures. *Chemical Physics Letters* **2010**, *487*, 153–164.

[27] Shen, X.; Song, C.; Wang, J.; Shi, D.; Wang, Z.; Liu, N.; Ding, B. Rolling up Gold Nanoparticle-Dressed DNA Origami into Three-Dimensional Plasmonic Chiral Nanostructures. *Journal of the American Chemical Society* **2012**, *134*, 146–149.

[28] Kuzyk, A.; Schreiber, R.; Fan, Z.; Pardatscher, G.; Roller, E.-M.; Högele, A.; Simmel, F. C.; Govorov, A. O.; Liedl, T. DNA-Based Self-Assembly of Chiral Plasmonic Nanostructures with Tailored Optical Response. *Nature* **2012**, *483*, 311–314.

[29] Berciaud, S.; Lasne, D.; Blab, G. A.; Cognet, L.; Lounis, B. Photothermal Heterodyne Imaging of Individual Metallic Nanoparticles: Theory *versus* Experiment. *Physical Review B* **2006**, *73*, 045424.

[30] Selmke, M.; Braun, M.; Cichos, F. Photothermal Single-Particle Microscopy: Detection of a Nanolens. *ACS Nano* **2012**, *6*, 2741–2749.

[31] Narushima, T.; Okamoto, H. Circular Dichroism Microscopy Free from Commingling Linear Dichroism *via* Discretely Modulated Circular Polarization. *Scientific Reports* **2016**, *6*, 1–10.

[32] Govorov, A. O.; Fan, Z.; Hernandez, P.; Slocik, J. M.; Naik, R. R. Theory of Circular Dichroism of Nanomaterials Comprising Chiral Molecules and Nanocrystals: Plasmon Enhancement, Dipole Interactions, and Dielectric Effects. *Nano Letters* **2010**, *10*, 1374–1382.

[33] Govorov, A. O.; Fan, Z. Theory of Chiral Plasmonic Nanostructures Comprising Metal Nanocrystals and Chiral Molecular Media. *ChemPhysChem* **2012**, *13*, 2551–2560.

[34] Yoo, S.; Park, Q.-H. Enhancement of Chiroptical Signals by Circular Differential Mie Scattering of Nanoparticles. *Scientific Reports* **2015**, *5*, 1–8.

[35] Albrecht, W.; Deng, T.-S.; Goris, B.; van Huis, M. A.; Bals, S.; van Blaaderen, A. Single Particle Deformation and Analysis of Silica-Coated Gold Nanorods before and after Femtosecond Laser Pulse Excitation. *Nano Letters* **2016**, *16*, 1818–1825.

[36] Ruijgrok, P.; Verhart, N.; Zijlstra, P.; Tchebotareva, A.; Orrit, M. Brownian Fluctuations and Heating of an Optically Aligned Gold Nanorod. *Physical Review Letters* **2011**, *107*, 037401.

[37] Taylor, A. B.; Siddiquee, A. M.; Chon, J. W. Below Melting Point Photothermal Reshaping of Single Gold Nanorods Driven by Surface Diffusion. *ACS Nano* **2014**, *8*, 12071–12079.

[38] Lambert, J.; Compton, R.; Crawford, T. D. The Optical Activity of Carvone: A Theoretical and Experimental Investigation. *The Journal of Chemical Physics* **2012**, *136*, 114512.

[39] Reinscheid, F.; Reinscheid, U. Stereochemical Analysis of (+)-Limonene Using Theoretical and Experimental NMR and Chiroptical Data. *Journal of Molecular Structure* **2016**, *1106*, 141–153.

[40] Gaiduk, A.; Ruijgrok, P. V.; Yorulmaz, M.; Orrit, M. Making Gold Nanoparticles Fluorescent for Simultaneous Absorption and Fluorescence Detection on the Single Particle Level. *Physical Chemistry Chemical Physics* **2011**, *13*, 149–153.

[41] Li, M.; Razumtcev, A.; Yang, R.; Liu, Y.; Rong, J.; Geiger, A. C.; Blanchard, R.; Pfluegl, C.; Taylor, L. S.; Simpson, G. J. Fluorescence-Detected Mid-Infrared Photothermal Microscopy. *Journal of the American Chemical Society* **2021**, *143*, 10809–10815.

[42] Zhang, Y.; Zong, H.; Zong, C.; Tan, Y.; Zhang, M.; Zhan, Y.; Cheng, J.-X. Fluorescence-Detected Mid-Infrared Photothermal Microscopy. *Journal of the American Chemical Society* **2021**, *143*, 11490–11499.

[43] Ding, T. X.; Hou, L.; Meer, H. v. d.; Alivisatos, A. P.; Orrit, M. Hundreds-Fold Sensitivity Enhancement of Photothermal Microscopy in Near-Critical Xenon. *The Journal of Physical Chemistry Letters* **2016**, *7*, 2524–2529.

[44] Gooch & Housego, Pockels Cell Alignment in a Q-Switched Laser. 2017; `https://gandh.com/wp-content/uploads/2017/10/GH-PM-EO-Pockels-cell-alignment-for-single-pass-systems.pdf` accessed 17 March 2021.

[45] Besteiro, L. V.; Zhang, H.; Plain, J.; Markovich, G.; Wang, Z.; Govorov, A. O. Aluminum Nanoparticles with Hot Spots for Plasmon-Induced Circular Dichroism of Chiral Molecules in the UV Spectral Interval. *Advanced Optical Materials* **2017**, *5*, 1700069.

[46] Govorov, A. O. Plasmon-Induced Circular Dichroism of a Chiral Molecule in the Vicinity of Metal Nanocrystals. Application to Various Geometries. *The Journal of Physical Chemistry C* **2011**, *115*, 7914–7923.

[47] Nesterov, M. L.; Yin, X.; Schaferling, M.; Giessen, H.; Weiss, T. The Role of Plasmon-Generated Near Fields for Enhanced Circular Dichroism Spectroscopy. *ACS Photonics* **2016**, *3*, 578–583.

[48] Jones, R. C. A New Calculus for the Treatment of Optical Systems. I. Description and Discussion of the Calculus. *JOSA* **1941**, *31*, 488–493.

[49] Hurwitz, H.; Jones, R. C. A New Calculus for the Treatment of Optical Systems. II. Proof of Three General Equivalence Theorems. *JOSA* **1941**, *31*, 493–499.

[50] Jones, R. C. A New Calculus for the Treatment of Optical Systems. III. The Sohncke Theory of Optical Activity. *JOSA* **1941**, *31*, 500–503.

[51] Jones, R. C. A New Calculus for the Treatment of Optical Systems. IV. *JOSA* **1942**, *32*, 486–493.

[52] Jones, R. C. A New Calculus for the Treatment of Optical System.V. A More General Formulation, and Description of Another Calculus. *JOSA* **1947**, *37*, 107–110.

[53] Jones, R. C. A New Calculus for the Treatment of Optical Systems. VI. Experimental Determination of the Matrix. *JOSA* **1947**, *37*, 110–112.

[54] Jones, R. C. A New Calculus for the Treatment of Optical Systems. VII. Properties of the N-Matrices. *JOSA* **1948**, *38*, 671–685.

[55] Jackson, J. D. *Classical Electrodynamics*; Wiley: New York, 1999.

[56] Hugonin, J.-P.; Besbes, M.; Ben-Abdallah, P. Fundamental Limits for Light Absorption and Scattering Induced by Cooperative Electromagnetic Interactions. *Physical Review B* **2015**, *91*, 180202.

4

Correlated optical and TEM measurements of quasi achiral and "superchiral" gold nanoparticles

Chemically synthesized chiral nanoparticles have strong chiral features and show strong circular dichroism (CD). However, a chemical synthesis process typically goes along with nonuniformity of shape and size, thereby affecting the chiroptical properties of the individual particles in the ensemble of synthesized particles. To find a clear relation between geometrical chirality and their chiroptical response, a correlative structural and optical study is essential on a single-particle level. Most existing single-particle circular dichroism measurements based on transmission or dark-field microscopy do not allow for a highly sensitive detection of the chiroptical response. We have shown that our photothermal circular dichroism (PT-CD) microscope is capable of detecting CD signals of single chiral nanoparticles down to g-factors of 3×10^{-4}*. Here we combine PT-CD measurements with electron tomography (ET) to investigate the relation between geometrical chiral features and chiroptical response of wet-chemically synthesized chiral nanorods and quasi-spherical gold nanospheres at the single-particle level. By analyzing their 3D structures, obtained from ET, we find that the synthesized chiral particles indeed have geometric features that give rise to a biased chiroptical response which is also confirmed by single-particle optical measurements. In addition, single-particle optical measurements show that the particles have a broad distribution in their strength and handedness of the chiroptical response. Particles with strong chiral features of a certain handedness exhibit a clear bias in their CD signal, however, the strength of their CDs is not directly related to the strength of the geometric chirality. To study how plasmonic resonance effects could play a role, we performed boundary-element method (BEM) simulation considering the 3D structures of the particles directly obtained from tomography without smoothing structural features.*

4.1. Introduction

A molecule or nanoobject is chiral when it cannot be superimposed with its mirror image. The standard way of detecting chiral nanoobjects is by measuring their circular dichroism (CD) spectra using a commercial CD spectrometer. CD is the differential absorption of left and right circularly polarized light. A commercial CD spectrometer measures the CD spectra, via extinction, of an ensemble of molecules and particles averaging out heterogeneous single-molecule/particle information. Several research groups have developed single-particle circular dichroism techniques [1–4], however, they do not measure a true absorption signal and are lacking sensitivity. Photothermal circular dichroism microscopy (PT-CD) is capable of measuring the direct differential absorption, free from scattering contributions [5] and can measure CD on single nanoparticles with unprecedented sensitivity [6]. In PT-CD we use Koehler illumination for the heating beam, because it preserves the polarization state of light in the focal plane, while, we use a highly focused probe beam which keeps the spatial resolution to the diffraction limit. For measurements of single chiral metallic nanoparticles, the leakage of linear dichroism (LD) into CD needs to be rejected to obtain CD sensitivity down to g-factor of 10^{-3} and smaller. We have shown in chapter 3 that, by employing a dual modulation of the polarization, the leakage of LD into CD can be rejected with a rejection ratio of more than 300 [6], which allows us to investigate small CD values in rod-like particles. The high detection sensitivity and rejection of artefacts is promising to study various chiral nanoparticles at the single-particle level.

Chiral plasmonic nanoparticles have recently received much attention owing to their potential in light manipulation as for example in circular polarizers [7], enantiomeric sensing of biomolecules [8], chiral waveguides [9] or negative refractive index materials [10]. Bottom-up fabricated plasmonic nanoparticles can be tailor-made with specific optical properties [11], however, their fabrication process is difficult for up-scaling. In addition, the polycrsytallinity of nanofabricated structures can dampen their plasmonic properties [12]. Chemically synthesized plasmonic nanoparticles are single-crystalline and can also exhibit strong CD. Due to the wet-chemical synthetic process their production can be upscaled easily. However, precisely controlling their shape and hence their chiral features remains a difficult task. A recent study [13] could reveal the correlation between the shape and the chiroptical response in chemically synthesized particles. This study relied on the reconstruction of the 3D shape of the nanoparticles by performing ET. The reconstruction was used to detect features of geometric chirality that lead to the strong chiroptical response of the particles. By applying fast Fourier transformations (FFTs) on the reconstructed nanoparticles, González-Rubio and coworkers [13] identified that repetitive wrinkles, i.e. helical features, caused the strong chirality in these systems. However, the study of such complex particles not only requires the knowledge of the shape of the particles but also the chiroptical response at the single-particle level. Until now most studies of the optical properties of chiral nanoparticles are carried out in ensemble measurements for the lack of sensitive single-particle CD techniques. Here we combine optical PT-CD measurements with ET to correlate geometrical features of chiral nanoparticles to optical CD at the single-particle level. Two types of nanoparticles are used in this study - chemically synthesized chiral gold nanorods and quasi-spherical gold nanospheres. Chiral nanorods are prepared by micelle-directed growth on top of gold nanorods [13]. Chiral molecules in the nanorod's solution

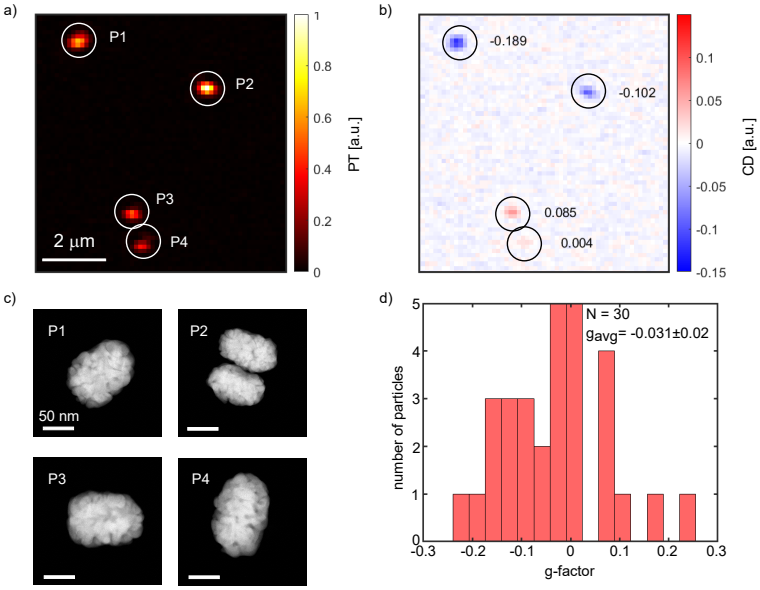

Figure 4.1: (a) Photothermal and (b) circular dichroism images of three single and one dimer of chiral gold nanorods. (c) TEM images of three single and one dimer of nanorods as labelled in (a). The scale bars are 50 nm. (d) Histogram of g-factors of 30 single chiral gold nanorods.

form worm-like micelles that can stick on top of the nanorods' surface and help in transferring chirality to the rod by further deposition of metal atoms. Gold nanospheres bought from Nanocomposix are single-crystalline nanoparticles with a truncated octahedral shape which is supported by transmission electron microscopy (TEM) measurements. To investigate the chiroptical properties of single nanoparticles, we dropcasted a solution of nanoparticles on a TEM grid where we can perform both, optical and TEM measurements.

4.2. Results and discussion

4.2.1. Chiral nanorods

Figure 4.1 (a) and (b) show photothermal (PT) and PT-CD images of four chiral nanoparticles. Correlated TEM measurements in (c) show that three of these particles are single nanorods and one is a dimer. The presence of a dimer is evidenced by the PT signal, which is about twice that of a single-particle. The absorption anisotropy (g-factor) of the ensemble was determined by means of commercial CD spectrometer as $g \sim$ -0.015 (see figure S4.1 in the SI) at the wavelength of the PT measurements (660 nm). The single-particle measurements in figure 4.1 reveal a striking difference with the ensemble measurements, namely that not only the strength of CD of individual particles varies strongly, also its sign can vary. We find that individual particles can have substantially stronger CD response as compared to the ensemble measurements, however, as the sign of CD also varies, the overall chiroptical

response of the ensemble is drastically reduced in magnitude. To check whether the PT-CD measurements resemble the chiroptical behaviour of the ensemble technique we performed more PT-CD measurements, all correlated with TEM measurements. Figure 4.1 (d) shows the histogram of g-factors of 30 chiral nanorods obtained by PT-CD at $660\,\mathrm{nm}$. Our single-particle measurements yield an average g-factor of -0.031$\pm$ 0.02, which is on the same order of magnitude as the ensemble measurements ($g \sim$ -0.016), however, the number of particles is not enough compared to the width of the histogram to allow a quantitative comparison of our single-particle measurements with the ensemble measurement. It should be noted here that at the moment the optical measurements were performed we did not realize, and therefore did not record, all the parameters that were necessary to determine an absolute sign of our CD measurements. That means that we cannot tell whether a negative/positive CD signal refers to more absorption of left- or more absorption of right-circularly polarized light. However, it should also be noted that the measurements are sign-consistent within themselves meaning that all particles that shows a certain sign in the CD measurement, all absorb either more left- or more right-circularly polarized light. Even though we cannot relate the sign of the CD measurements to whether the particles absorb more left or more right circularly polarized light, our first finding, that the particles' CD is broadly distributed with particles having both positive and negative chiroptical response still holds true. We chose the sign such that it is in agreement with the ensemble measurements in figure S4.1.

A direct comparison with the ensemble measurements is anyway only partially justified as the PT measurements are carried out for particles lying flat on the surface while the CD values obtained by the CD spectrometer, being measured in solution, averages the response of particle orientations. Different particle orientations can affect the chiroptical response. Furthermore, larger nanoparticles, especially rod-like ones, can have a scattering contribution to the extinction signal, that can be on the order of the absorption [2] contribution. Therefore we cannot neglect possible contributions due to circular dichroism scattering of the ensemble measurements which measures a combination of scattering and absorption.

We then take a closer look at the 7 nanorods on which we performed ET measurements to reconstruct their 3D shape. The left sides in figure 4.2 (a), (d), (g) show the 3D visualization of ET results of three nanorods with significantly different g-factors, from a highly chiral nanorod with a positive g-factor (a) to a nanorod with an one order of magnitude lower g-factor (d) and a nanorod with negative g-factor (g). González-Rubio et al. [13], who performed ET studies on particles grown by the same method, concluded that the chiroptical signal of these nanorods stem from helical features in their morphology. Consequently, we tracked local helical features for our correlated morphologies based on the geometrical shape obtained from the reconstruction. Details about the procedure can be found in section 4.4. In short, after converting the reconstruction to cylindrical coordinates, all pixels in the corresponding FFT with the same orientation are binned. The quantification of the directionality can then be used to quantify the helicity. The right sides of figure 4.2 (a), (d), (g) shows the calculated helical features overlaid with the thresholded reconstructions. Interestingly, it becomes immediately clear that each particle contains both, left- and right-handed features.

To further quantify the helicity, we projected the reconstructions in cylindrical coordinates along the radius. The results are shown in figure 4.2 (b), (e), (h). Based on the projections, we created helicity maps as shown in (c), (f) and (i). The mix of helicities within each particle becomes immediately clear in the projected maps as well. Yet, there are also clear

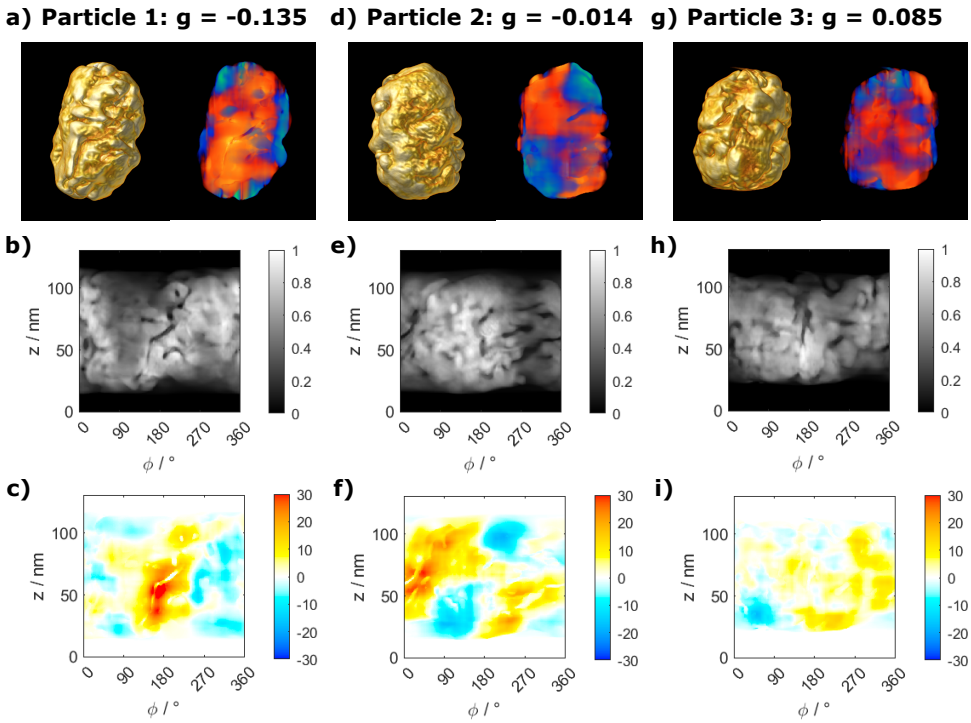

Figure 4.2: Correlation of measured g-factors and electron tomography on single chiral nanorods. (a), (d), (g) show 3D visualizations (left) of three nanorods with different g-factors, which were measured by single-particle PT-CD. The right images show local geometrical helicities of the same nanorods. Red and blue colors correspond to positive and negative helicities. (b), (e), (h) display the radially projected and unwrapped nanorods. (c), (f), (i) show the radially projected helicity maps.

differences between the three particles. The nanorod in (a) with a strong positive g-factor exhibits a prominent area of strong positive geometrical handedness as shown in red in figure (c). This strong chiral feature is related to the big groove around 200° in (b), and is also visible in the 3D visualization in (a). It seems to dominate the overall optical response leading to the high positive g-factor. For the nanorod with one order of magnitude lower g-factor, the projected helicity map in (f) shows areas of relatively strong positive handedness but also large regions of opposite handedness. It seems that the areas of different handedness average out the optical chirality to some extent leading to a much lower g-factor compared to particle 1. Particle 3, for which we measured a strong negative g-factor, displays only areas with weak positive and weak negative geometrical helicity (figure 4.2(i)). From the "helical-like" geometrical features, that were assigned by González-Rubio et al. [13] to be responsible for the chiroptical response, it is thus not conclusive where the negative g-factor stems from.

Figure 4.3 presents the average of the projected helicity maps as a function of the measured g-factor for 7 particles including the ones from figure 4.2. For 6 out of the 7 nanorods that we measured, a positive g-factor correlated to a positive average helicity. This corre-

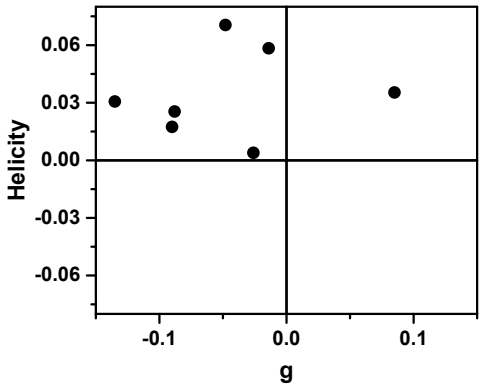

Figure 4.3: Average of helicity maps as a function of measured g-factor for 7 single nanorods.

lation indicates that the average geometrical chirality is indeed influencing the chiroptical properties.

The important conclusion from figure 4.3 is that the strength of the CD signal cannot be directly connected to the average helicity, meaning that stronger geometrical chiral features do not necessarily lead to a stronger chiroptical response. Consequently, additional factors must significantly influence the optical response. On the one hand, of course, plasmonic effects play a role. Due to the differences in shape, each nanorod has a different plasmonic resonance. However, it is quite challenging to perform simulations to understand the plasmonic effect on the chiroptical behavior of a chiral nanorods because of its complex structure. We rather chose a much simpler geometry such as quasi-spherical gold nanoparticles to get a better understanding of the relation between geometrical features and plasmonic influence with their optical CD properties, which we discuss in the following section.

4.2.2. Nominally achiral nanoparticles

To elucidate what other effects play a role, we looked at quasi-spherical gold nanoparticles. We chose for Au truncated octahedra as they are known to be single-crystalline, which avoids any influences from crystalline defects. These gold nanoparticles are often considered as being "achiral". However, due to their wet-chemical synthesis they are heterogeneous in size and shape. Like with the chiral nanorods we performed correlated optical and ET measurements to obtain the optical CD g-factors as well as the structural information of the quasi-achiral particles. Figure 4.4 shows correlative optical and tomography images of four single gold nanoparticles. Figure 4.4 (a) and (b) show PT and PT-CD images and figure (c) shows tomography images of the same four particles. The PT signal, which scales linearly with the absorption, shows different absorption strength, which is normally related to different sizes of the particles. In this case, however, the topology of the substrate surface of the TEM grid-window causes some particles to be either in- and others to be out-of-focus within one scan area. To determine the CD of the particles we calculate their g-factor, which is defined as the differential absorption divided by the total (isotropic) absorption. As we

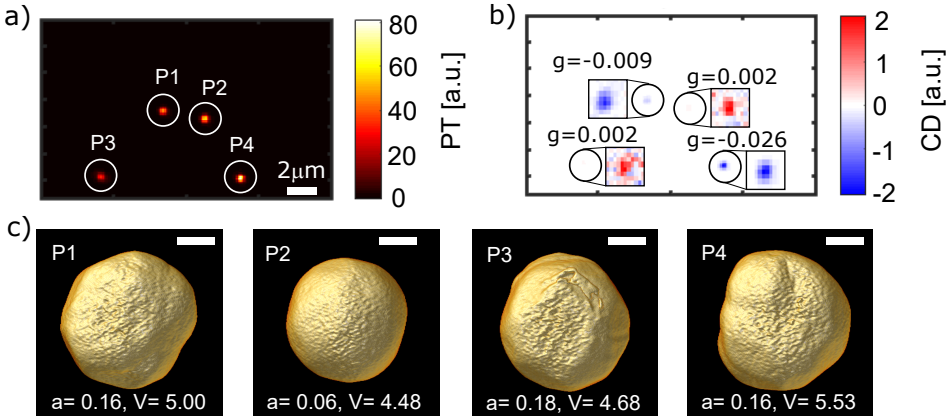

Figure 4.4: (a) PT and (b) PT-CD images of four single gold nanoparticles. Solid circles are drawn to show correlation between the two images. To show the contrast of the weak signals in CD, each particle's image in (b) is shown with an adjusted contrast as marked with square boxes. The numbers in (b) correspond to the particle's g-factor. The scale bar in (a) is $2\,\mu\mathrm{m}$. (c) Electron tomography of the four single-particles as labelled in (a). The scale bar is $30\,\mathrm{nm}$. In (c) a is the asphericity and V is the volume of the particle in nm^3 divided by factor of 10^5.

show in figure S4.2, defocusing affects both the PT and the CD measurements alike and therefore the g-factor is independent of the focus position.

The 3D reconstructed images of the single-particles, displayed in figure 4.4 (c), show that the particles are heterogeneous in shape. We use the reconstructed images to calculate the particles' asphericity. The asphericity is as a measure of the deviation from a spherical shape. An asphericity equal to 0 corresponds to a perfect sphere and for a non-spherical shape asphericity is greater than 0. The inset in figure 4.4 (c) indicates the respective asphericity of the particles. Particle P2 has a low asphericity and exhibits a weak g-factor of 0.002, on the other hand, particles with large asphericity (P1, P3 and P4) can exhibit both strong and weak CD signals. In the optical measurements we only probe one specific orientation of the geometry and therefore are not sensitive to deviations from the spherical shape along the optical axis. When we calculate the asphericity from the shape we therefore have to neglect protrusions of the particle along the optical axis, this is indicated by the "2D".

In total we have measured 25 single gold nanoparticles correlated with tomography measurements. Figure 4.5 (a) shows the correlation between asphericity and measured g-factors. We find that particles with low asphericity mostly exhibit weak CD signals while particles with higher asphericity can exhibit both, strong and weak CD signals. We conclude that asphericity is needed to create CD but asphericity does not inevitably lead to CD. A nanorod for example would have nonzero asphericity but clearly is not chiral. A more meaningful measure to represent geometric chirality than asphericity is the Hausdorff chirality which is a measure of the lack of congruence of an object with its mirror image [14]. It measures the missing volumetric overlap of an object with its mirror image. A rod-shaped object, which is achiral, will have zero Hausdorff chirality, whereas it will have nonzero asphericity. Figure 4.5 (b) shows the correlation between Hausdorff chirality and the optical CD measurements. As we probe only a specific orientation of the particle we must calculate the Hausdorff chi-

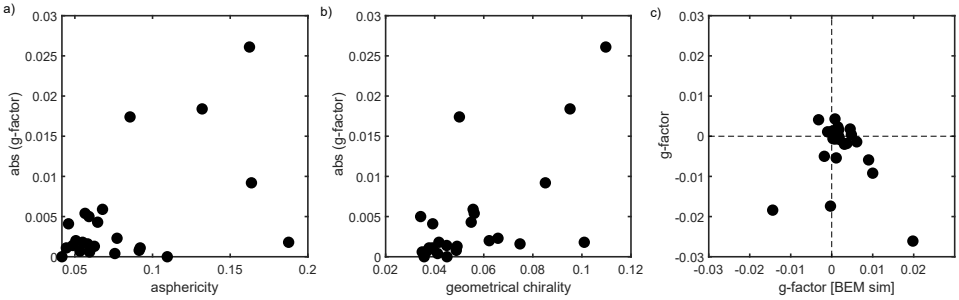

Figure 4.5: Correlation plots of g-factor obtained from the experiment with (a) 2D-asphericity, (b) 2D Hausdorff and (b) g-factor calculated with the boundary element method (BEM) simulation at $532\,\mathrm{nm}$. None of the correlation plots show a direct correlation between the corresponding parameters for all particles.

rality using only rotations along the optical axis and translations perpendicular to it which is indicated by the "2D". We find that smaller 2D Hausdorff chirality values correlate with smaller g-factors, and that larger Hausdorff values allows for but do not guarantee large g-factors. Compared to the asphericity measure we find a better correlation for the Hausdorff chirality with the optical measurements, but from our purely geometric considerations we again can conclude that there is a fundamental difference between the geometric-chirality of an object and its optical manifestation at a given wavelength (here the CD at $532\,\mathrm{nm}$).

Besides the fact that the wavelength plays an important role, plasmonic effects can also enhance CD. Such behaviour cannot be predicted by geometric considerations alone. We therefore also performed BEM simulations of the same 25 ET-reconstructed particles. Figure 4.5 (c) shows the correlation between optical measurements and BEM simulations using the Matlab MNPBEM toolbox. As opposed to asphericity and Hausdorff chirality we can also take into account the sign of the CD signal. Most of the particles that have weak CD values (below a g-factor of 0.01) also exhibit a weak CD in the optical measurements and simulations. However, for particles with larger optical CD values we also find cases with substantial deviations from the BEM simulations. One particle for example has strong negative CD for both optical measurements and BEM, other particles though have strong CD effects with opposite sign in experiment and simulations. Here we must note again that we missed to record all the necessary parameters to be able to tell whether a positive/negative sign in the CD measurements corresponds to more absorption of left or right circularly polarized light. The correlation plot in figure 4.4 (c) therefore shows an arbitrarily chosen sign for the CD measurements. However, the absence of a clear correlation of BEM calculations and CD measurements persists in both cases.

We think that there might be additional effects, which contribute to the particles' CD signal but that are not related to the particles' shape, and therefore lead to the mismatch of optical measurements and the simulations based on the reconstructed geometry. We hypothesize several sources that could contribute to the CD signal. First of all the substrate will have an influence on the chiroptical response as has been shown earlier [15, 16]. Even though we use immersion-oil for the optical measurements, which should match the substrate's refractive index, as we heat the oil during the measurement we effectively decrease its refractive index. Additionally, the substrate (silica) on which the particles reside is only

$18\,\mathrm{nm}$ thick and we cannot exclude the presence of an air cavity behind the substrate's surface. An air cavity behind a very thin substrate could additionally introduce a symmetry break [15], due to the refractive index mismatch. Furthermore, we imagine that ligands on the nanoparticle's surface could play a role as well as they have been reported to alter the particle's plasmonic response [17].

4.3. Conclusion

The synthesis process of chiral nanorods creates a weak bias towards a certain geometric handedness as well as the chiroptical response of the particles, when measurements are performed on a large ensemble of particles in solution. However, the study of individual particles revealed that the strength of the chiroptical response is not directly related to the helicity as particles with a large helicity can have weak chiroptical response and vice versa. This may be related to plasmonic effects, however, as we show with our simple model-system of quasi achiral particles, even plasmonic effects cannot satisfactorily explain the relation between shape and chiroptical response. That means that, even if we knew the shape of a nanoparticle and were able to simulate its chiroptical response, thereby taking into account also its plasmonic behaviour (and wavelength dependence), we find only a weak correlation between measurement and simulations and thus the geometry. Other effects that we have not taken into account may add a residual CD signal that do not allow us to determine the optical response if we consider only the geometry of the particle. Such effects might be related to surface ligands, or the substrate which can cause an additional symmetry break and therefore alter the chiroptical response of nanoparticles. Due to the broad distribution of g-factors in chemically-synthesized nanoparticles, more measurements would be necessary to draw concrete conclusions. Furthermore we should make sure to determine the global sign of the optically measured CD signal to allow for a direct comparison of BEM simulations and optical measurements.

4.4. Experimental

4.4.1. Sample preparation

For the correlative transmission electron microscopy and optical measurement, single gold nanospheres (diameter of $100\,\mathrm{nm}$, purchased from nanoComposix) or single chiral gold nanorods (wet chemically-synthesized according to reference [13]) were drop-casted on a TEM grid which contains silicon dioxide support film of thickness $18\,\mathrm{nm}$ and aperture of $70\times70\,\mu\mathrm{m}^2$ (product no.: 21532-10, purchased from Ted Pella). The TEM grid was then sandwiched with a second glass slide (thickness of about $170\,\mu\mathrm{m}$). An immersion oil was used as a photothermal medium because of its high viscosity and hydrophobicity which was essential for the sandwiched TEM grid sample. For measurements of single gold nanospheres, immersion oil of refractive index of 1.51 and for measurements of single chiral gold nanorods, an immersion liquid of refractive index of 1.33 were used. First optical measurements were performed and thereafter the TEM grid was cleaned with toluene to remove the immersion oil. The cleaned TEM grid containing single gold nanospheres was used for TEM measurements. For optical measurements only the nanospheres or nanorods which

were deposited on the marked silicon dioxide windows, were chosen. TEM measurements were performed on the same nanospheres or nanorods. For nanorods and nanospheres measurements, the heating laser powers were $25.6\,\mathrm{mW}$ and $8\,\mathrm{mW}$, respectively illuminated in an area of about $20\,\mu\mathrm{m}^2$ and the probe laser powers were $0.8\,\mathrm{mW}$ and $2\,\mathrm{mW}$, respectively in a diffraction-limited focus area.

4.4.2. g-factor analysis of optical measurements

g-factors were calculated as the ratio of mean values of photothermal and photothermal circular dichroism signal averaging in an area of 7×7 pixels^2 around the centroid position of each individual particle.

4.4.3. Transmission electron microscopy and tomography

HAADF-STEM images and electron tomography tilt series were acquired using a FEI-Osiris electron microscope operated at $200\,\mathrm{kV}$. Tilt series were acquired for the maximal possible tilt range for the SiO_2 TEM grids, which was generally around $\pm65°$. The tilt increment was $3°$. The tilt series for the achiral nanoparticles were reconstructed in the following manner: After aligning the tilt series images by cross-correlation, the stacks of aligned projection images served as inputs for 100 iterations of the expectation maximization implemented in the ASTRA toolbox [18, 19]. The reconstructions were furthermore thresholded using the Otsu method and the thresholded reconstructions were used for determining the volume. The tilt series for the more complex chiral nanorods were reconstructed in the following manner: After distortion corrections with the help of a convolutional neural network, 3D reconstructions were performed by the simultaneous iterative reconstruction technique and the application of constraints in real and Fourier space, following previous work [13].

4.4.4. Quantification of asphericity

The asphericity is a metric used to determine how much a given shape differs from a sphere. To calculate this metric, we segmented the 3D ET reconstructions to retrieve a binary volume. We then calculated the volume of the reconstructed shape and created a new binary volume containing a perfect sphere with the same volume. The asphericity was then calculated as the minimal shape error between the reconstructed volume and the sphere.

4.4.5. Hausdorff chirality quantification

The Hausdorff chirality measure is a measure to quantify the chirality of a set of points which typically describe a molecule. This chirality measure is determined by calculating the minimum Hausdorff distance between a set of points and the mirror image of that set of points. To make the measure scale-invariant, the result is then divided by the diameter of this set of points, which is calculated as the maximum distance between any two points of the set. However, since our data is stored as a 3D volume, we adapted the Hausdorff method as follows and call it as geometrical chirality. First the 3D ET reconstructions were segmented into binary volumes. Next, analogously to the Hausdorff chirality measure, we

define a chirality measure as the minimum shape error between the binary reconstruction and its mirror image. The shape error is defined as the number of mismatching voxels divided by the number of voxels included in the volume and is therefore already scale-invariant. The chirality measure is found by minimizing the shape error for rigid transformations of the mirrored volume.

4.4.6. Boundary element method simulations

The discretized Otsu thresholded tomography reconstructions of the Au nanoparticles served as an input for BEM calculations, which were performed solving the full Maxwell equations at 100 points in the wavelength range from 500 to $700\,\mathrm{nm}$ using left and right circularly polarized light using the MNPBEM Matlab toolbox v17. The g-factor was then determined as defined in chapter 2.

4.4.7. Quantification of helicity

Helicity can be quantified by investigating the directionality of features in a three-dimensional volume in cylindrical coordinates. Namely, features that are oriented parallel with the (x, y)-plane (horizontal) or with the z-axis (vertical) can be labeled as being "achiral", while other features are oriented such that they wrap around the z-axis and are therefore helical. To quantify this, we calculated the local helicity for each voxel in cylindrical coordinates by investigating the directionality of a small region around that voxel in the (ϕ, z)-plane according to the method described in [20], which uses the gradient to quantify the local helicity in a region. More specifically, features of a particle will show a strong change in intensity in the direction orthogonal to the inclination angle. For example, horizontal features correspond to a wavevector parallel to $\vec{g} = (0, g_z)$ and vertical features correspond to a wavevector parallel to $\vec{g} = (g_\phi, 0)$. Right-handed features will be represented by $\vec{g} = (g_\phi, g_z)$ with $g_z \cdot g_\phi < 0$ and left-handed features analogously by $\vec{g} = (g_\phi, g_z)$ with $g_z \cdot g_\phi > 0$. This insight leads to a filter that can be used for the quantification of helicity:

$$H(g_\phi, g_z) = -sign(g_\phi \cdot g_z) \tag{4.1}$$

with

$$sign(x) = \begin{cases} -1, x < 0 \\ 1, x > 0 \\ 0, x = 0 \end{cases} \tag{4.2}$$

The local helicity in a voxel at location (ρ_i, ϕ_i, z_k) is then given by

$$H(\rho_i, \phi_i, z_k) = \iint dk_\phi dk_z \|\vec{g}\| \cdot H, \tag{4.3}$$

where $\vec{g}$ is the magnitude of the gradient at a given location and the integral goes over a small two-dimensional window around the (ρ_i, ϕ_i, z_k) voxel in the (ϕ, z)-plane. The magnitude of the gradient is taken as a metric that indicates the "amount" of features oriented in a certain direction. For our experiments, we used windows of 64×64 pixels. This method results

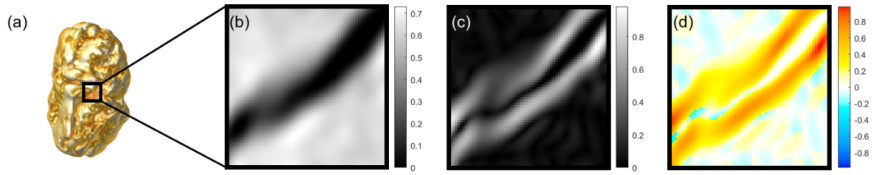

Figure 4.6: The procedure to calculate the helicity measure in a small region of the volume. A 3D rendering of one of the chiral nanorods is shown in (a), a small region around a voxel is selected in (b), the magnitude of the gradient is shown in (c), and the orientation of the gradient is used to assign the correct sign indicating the handedness to each pixel as shown in (d).

in a single value for each voxel in cylindrical coordinates that indicates the helicity of the particle in that region. Positive values correspond to right-handed helicity and negative values to left-handed helicity. Figure 4.6 illustrates this procedure: (a, b) select a region in a slice around a voxel from the 3D volume, (c) calculate the gradient of this region and (d) apply the H filter. The helicity value for the selected voxel is the sum over the result in (d), which is in this case positive and therefore indicates that the feature is right-handed.

4.5. Supplementary information

4.5.1. Ensemble CD spectra of the S-enantiomer of chiral nanorods

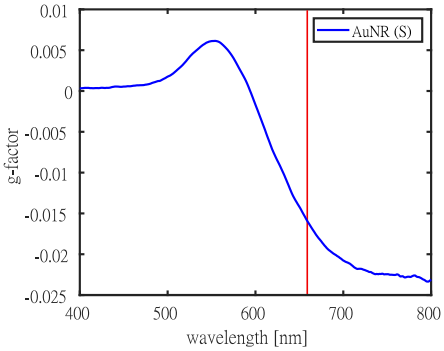

Figure S4.1: Ensemble circular dichroism (CD) spectra of an aqueous solution of chiral gold nanorods with S enantiomers. The g-factor at 660 nm indicated by the vertical red line is about -0.016.

Figure S4.1 shows a CD spectrum of a diluted stock solution of the chiral nanorods obtained by a commercial CD spectrometer. Our optical single-particle CD measurements were carried out at 660 nm as indicated by the vertical red line. At that wavelength the ensemble measurements yields a g-factor of -0.016.

4.5.2. Effect of defocusing on the CD g-factor

Because of the non-flat surface of the TEM grid window, some particles are in-focus and others are slightly out-of-focus in our optical measurements. Therefore, we checked if the slight defocusing may have an influence on the CD g-factor. We measured a single 100 nm gold nanoparticle in-focus and out-of-focus as shown in figure S4.2. Slight defocusing decreases both photothermal (PT) and circular dichroism (CD) signals alike and therefore the calculated g-factor (i.e. the ratio of CD and PT) remains nearly unchanged.

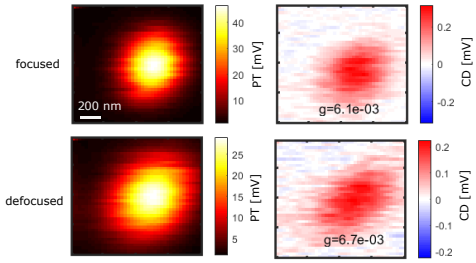

Figure S4.2: Photothermal (PT) and circular dichroism (CD) image of a single gold nanoparticle in (a) focused and (b) slightly defocused conditions showing slight defocusing has nearly no influence in the value of g-factor.

References

[1] Vinegrad, E.; Vestler, D.; Ben-Moshe, A.; Barnea, A. R.; Markovich, G.; Cheshnovsky, O. Circular Dichroism of Single Particles. *ACS Photonics* **2018**, *5*, 2151–2159.

[2] Wang, L. Y.; Smith, K. W.; Dominguez-Medina, S.; Moody, N.; Olson, J. M.; Zhang, H.; Chang, W. S.; Kotov, N.; Link, S. Circular Differential Scattering of Single Chiral Self-Assembled Gold Nanorod Dimers. *ACS Photonics* **2015**, *2*, 1602–1610.

[3] Lu, X.; Wu, J.; Zhu, Q.; Zhao, J.; Wang, Q.; Zhan, L.; Ni, W. Circular Dichroism From Single Plasmonic Nanostructures With Extrinsic Chirality. *Nanoscale* **2014**, *6*, 14244–14253.

[4] Zhang, Q.; Hernandez, T.; Smith, K. W.; Jebeli, S. A. H.; Dai, A. X.; Warning, L.; Baiyasi, R.; McCarthy, L. A.; Guo, H.; Chen, D.-H., et al. Unraveling the Origin of Chirality From Plasmonic Nanoparticle-Protein Complexes. *Science* **2019**, *365*, 1475–1478.

[5] Spaeth, P.; Adhikari, S.; Le, L.; Jollans, T.; Pud, S.; Albrecht, W.; Bauer, T.; Caldarola, M.; Kuipers, L.; Orrit, M. Circular dichroism measurement of single metal nanoparticles using photothermal imaging. *Nano Letters* **2019**, *19*, 8934–8940.

[6] Spaeth, P.; Adhikari, S.; Baaske, M. D.; Pud, S.; Ton, J.; Orrit, M. Photothermal Circular Dichroism of Single Nanoparticles Rejecting Linear Dichroism by Dual Modulation. *ACS Nano* **2021**,

[7] Gansel, J. K.; Thiel, M.; Rill, M. S.; Decker, M.; Bade, K.; Saile, V.; von Freymann, G.; Linden, S.; Wegener, M. Gold Helix Photonic Metamaterial as Broadband Circular Polarizer. *Science* **2009**, *325*, 1513–1515.

[8] Hendry, E.; Carpy, T.; Johnston, J.; Popland, M.; Mikhaylovskiy, R.; Lapthorn, A.; Kelly, S.; Barron, L.; Gadegaard, N.; Kadodwala, M. Ultrasensitive Detection and Characterization of Biomolecules Using Superchiral Fields. *Nature Nanotechnology* **2010**, *5*, 783–787.

[9] Coles, R.; Price, D.; Dixon, J.; Royall, B.; Clarke, E.; Kok, P.; Skolnick, M.; Fox, A.; Makhonin, M. Chirality of Nanophotonic Waveguide With Embedded Quantum Emitter for Unidirectional Spin Transfer. *Nature Communications* **2016**, *7*, 1–7.

[10] Pendry, J. A Chiral Route to Negative Refraction. *Science* **2004**, *306*, 1353–1355.

[11] Hentschel, M.; Schäferling, M.; Duan, X.; Giessen, H.; Liu, N. Chiral Plasmonics. *Science Advances* **2017**, *3*, e1602735.

[12] Kusar, P.; Gruber, C.; Hohenau, A.; Krenn, J. R. Measurement and Reduction of Damping in Plasmonic Nanowires. *Nano Letters* **2012**, *12*, 661–665.

[13] González-Rubio, G.; Mosquera, J.; Kumar, V.; Pedrazo-Tardajos, A.; Llombart, P.; Solís, D. M.; Lobato, I.; Noya, E. G.; Guerrero-Martínez, A.; Taboada, J. M.; Obelleiro, F.; MacDowell, L. G.; Bals, S.; Liz-Marzán, L. M. Micelle-Directed Chiral Seeded Growth on Anisotropic Gold Nanocrystals. *Science* **2020**, *368*, 1472–1477.

[14] Buda, A. B.; Mislow, K. A Hausdorff Chirality Measure. *Journal of the American Chemical Society* **1992**, *114*, 6006–6012.

[15] Nechayev, S.; Barczyk, R.; Mick, U.; Banzer, P. Substrate-Induced Chirality in an Individual Nanostructure. *ACS Photonics* **2019**, *6*, 1876–1881.

[16] Arteaga, O.; Sancho-Parramon, J.; Nichols, S.; Maoz, B. M.; Canillas, A.; Bosch, S.; Markovich, G.; Kahr, B. Relation Between 2D/3D Chirality and the Appearance of Chiroptical Effects in Real Nanostructures. *Optics Express* **2016**, *24*, 2242.

[17] Ghosh, S. K.; Nath, S.; Kundu, S.; Esumi, K.; Pal, T. Solvent and Ligand Effects on the Localized Surface Plasmon Resonance (LSPR) of Gold Colloids. *The Journal of Physical Chemistry B* **2004**, *108*, 13963–13971.

[18] Moon, T. K. The Expectation-Maximization Algorithm. *IEEE Signal Processing Magazine* **1996**, *13*, 47–60.

[19] Van Aarle, W.; Palenstijn, W. J.; De Beenhouwer, J.; Altantzis, T.; Bals, S.; Batenburg, K. J.; Sijbers, J. The ASTRA Toolbox: A Platform for Advanced Algorithm Development in Electron Tomography. *Ultramicroscopy* **2015**, *157*, 35–47.

[20] Heyvaert, W.; Pedrazo-Tardajos, A.; Kadu, A.; Claes, N.; González-Rubio, G.; Liz-Marzán, L. M.; Albrecht, W.; Bals, S. Quantification of the helical morphology of chiral Au nanorods. 2022.

5

Magnetic circular dichroism of superparamagnetic nanoparticles

Magnetic imaging is a versatile tool in biological and condensed-matter physics. Existing magnetic imaging techniques either require demanding experimental conditions which restrict the range of their applications or lack the spatial resolution required for single-particle measurements. Here, we combine photothermal (PT) microscopy with magnetic circular dichroism (MCD) to develop a versatile magnetic imaging technique using visible light. Unlike most magnetic imaging techniques, photothermal magnetic circular dichroism (PT MCD) microscopy works particularly well for single nanoparticles immersed in liquids. As a proof of principle, we demonstrate magnetic CD imaging of superparamagnetic magnetite nanoparticles immersed in microscope immersion oil. The sensitivity of our method allowed us to probe the magnetization curve of single $\sim$*400* nm*-diameter magnetite nanoparticles.*

5.1. Introduction

Light-matter interaction in magnetic materials gives rise to unique magneto-optical phenomena like the Faraday and Kerr effects. Ultrafast spectroscopy with femtosecond pulsed lasers enables manipulation of magnetic properties such as magnetization reversal [1] or demagnetization of ferromagnetic metallic thin films [2]. Magnetic nanoparticles are promising candidates for applications in biomedicine, spintronics and data storage [3, 4]. Magnetite (Fe_3O_4) nanoparticles, because of their size-dependent magnetic properties and biocompatibility, have been used for bioimaging, for photothermal [5] and magnetothermal cancer treatment [6]. For magnetic data storage, the minimum size of a magnetic bit is limited by the so-called *superparamagnetic limit* [7, 8]. Superparamagnetism occurs in ferromagnetic and ferrimagnetic materials. Bulk magnetite shows ferrimagnetic behaviour. Single-domain magnetite nanoparticles of sufficiently small size randomly flip their magnetization direction, on the timescale of laboratory experiments (s-hrs), when the magnetic energy barrier is on the order of, or smaller than the thermal energy [9]. When the measurement time is longer than the average time between two magnetization flips, the particle appears to carry no average magnetic moment. Just as paramagnetic particles, superparamagnetic ones can be magnetized under an external magnetic field, but typically exhibit much larger susceptibility. To study magnetic phenomena of single nanoparticles one can use non-optical devices such as SQUIDs (superconducting quantum interference devices) and MFMs (magnetic force-microscopes), or X-ray beam techniques such as XMCD (X-ray magnetic circular dichroism). Conventional SQUID magnetometers detect the net signal from large ensembles of nanoparticles, averaging out the size-dependent magnetic properties of the nanoparticles. For imaging purposes, scanning-SQUID microscopy can be used to image the magnetic flux from individual particles - in some cases with sub-$100\,\mathrm{nm}$ resolution [10]. Owing to their exceptional sensitivity, down to individual single-molecule magnets [11], SQUIDs are therefore widely used in the study of magnetic nanostructures [12], however, they require a cryogenic environment, complex probes and electronics, which can be difficult to implement for many applications. MFM is a considerably simpler technique with excellent spatial resolution and can operate at ambient conditions. However, MFM also faces drawbacks such as topographic cross talk and the magnetic distortions caused by the strong stray fields of the probe [13]. Furthermore, when studying samples in external magnetic fields, not only the sample but also the probing tip is influenced by the field [14]. XMCD provides high spatial resolution and sensitivity in the study of single nanoparticles [15], but it requires access to a beam line.

Magnetic circular dichroism (MCD) spectroscopy [16, 17] is an optical technique that exploits the polar Kerr effect [18]. Until now conventional visible-light MCD spectroscopy has only been used to investigate magnetic nanoparticles [16] or (bio-) molecules [17] in solutions containing an ensemble of many nanoparticles. The investigation of size- and shape-dependent magnetic properties, however, demands single-particle resolution. XMCD and electron holography measurements of single particles show that the magnetic properties not only depend on their size, but also on their shape, and on temperature [15, 19]. For instance, cobalt and iron particles in the range of $8\,\mathrm{nm}$ to $20\,\mathrm{nm}$ can exhibit both ferromagnetic and superparamagnetic behaviors at room temperature [20]. Distinctions in magnetic behaviour due to shape and size cannot be made by measuring an ensemble of nanoparti-

cles, and yet, they are of vital importance to their applications in biomedical sciences and spintronic devices. Here, we overcome the limitation of visible-light MCD to ensemble measurements by implementing our newly developed Photothermal circular dichroism (PT CD) microscopy [21, 22] for magnetic imaging of single nanoparticles. To image the magnetization of nanoparticles, PT MCD is considerably simpler as, for example, XMCD or scanning SQUID, making it far more accessible. Our method directly measures the absorption of individual particles via their PT response. As the absorption linearly scales with the particle's volume we can access the particle's size. The MCD signal, which we can determine separately via PT MCD measurements, displays a linear dependence on the particle's magnetization [18, 23]. Our measurements therefore allow us to simultaneously access the size and the magnetization of individual particles.

Figure 5.1 shows a scheme of our PT MCD setup. The setup is a photothermal microscope [24] augmented with polarization modulation optics in the heating arm to facilitate photothermal circular dichroism measurements [21]. We use a dual modulation of the polarization because it offers excellent rejection of cross talk between linear and circular dichroism as discussed in chapter 3. By modulating either the intensity or the polarization of the heating beam, we can access absorption signals such as the total absorption (PT) as well as LD (linear dichroism) and CD. We use a Koehler configuration for the heating beam illumination but we strongly focus the probe beam. Thereby, the optical resolution at the probing wavelength ($780\,\mathrm{nm}$) remains diffraction-limited while the polarization state of the heating light ($532\,\mathrm{nm}$) remains well preserved. In circular dichroism mode our technique measures the differential absorption between left- and right-circularly polarized light and therefore is most sensitive to magnetic moments that are parallel (or anti parallel) to the propagation direction of the light. To measure PT CD in the presence of an external magnetic field (PT MCD), a long cylindrical permanent magnet (NdFeB, $3\,\mathrm{mm}$ diameter, $10\,\mathrm{cm}$ length) is used to provide an out-of-plane magnetic field at the sample such that the light propagation is parallel to the magnetization direction (optical z-axis). The magnetic field strength and sign can be varied by altering the distance and by flipping the orientation of the magnet relative to the sample.

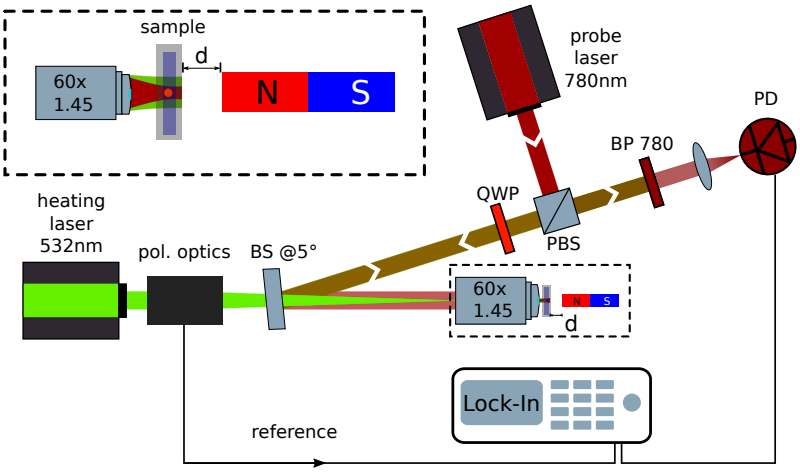

Figure 5.1: Schematic setup of the photothermal circular dichroism microscope. The 532 nm continuous wave (CW) heating laser beam is passed through a combination of polarization optics which modulates the polarization of the light between left- and right- circularly polarized at ∼100 kHz. The 780 nm CW probe laser is passed through a combination of a polarizing beam-splitter (PBS) and a quarter-wave plate (QWP) and combined with the heating beam at the 50/50 beam-splitter (BS) at an angle of about 5°. The sample is illuminated with the heating beam in a Koehler configuration, whereas the probe beam is focused at the sample through an oil-immersion objective (NA = 1.45). The collected probe light is filtered from the heating light with a band-pass filter (BP 780). The photothermal signal is isolated by a lock-in amplifier. A long cylindrical permanent magnet is placed perpendicular to the sample plane at a variable distance *d* to apply a magnetic field to the sample. The inset shows an enlarged view of the heating and probe beam illumination and the position of the magnet relative to the sample. To flip the magnetic field direction, the magnet's poles are flipped. A polarization optics unit consists of two polarization modulators, driven at two different frequencies ω_1 and ω_2. An additional set of static birefringent plates and a polarizer enable polarization and amplitude modulation of the heating beam as described in chapter 3. A reference signal at the sum frequency ω_1+ω_2 of the two modulators is sent to the lock-in amplifier.

5.2. Results and discussion

Here we study nominally 200 nm-diameter magnetite nanoparticles (Chemicell GmbH) in a variable magnetic field. The tunable magnetic field enables us to discern MCD from geometric CD. Geometric CD is induced by the chiral structure of an object [25]. In contrast to geometric CD, MCD in ferro- and ferrimagnetic materials results from the polar magneto-optic Kerr effect [18, 23]. The Kerr effect is induced by magnetic perturbations of the electronic states involved in optical transitions. It results from the interaction between electrons that provide magnetic moments and those that have large spin-orbit coupling [18, 26].

A single-crystalline magnetite particle of 200 nm-diameter is expected to have multiple magnetic domains and, moreover, it will exhibit magnetic remanence. The particles used

here, however, are clusters of sub-15-nm single crystals. At room temperature, magnetite particles of such size show superparamagnetic behavior. When they form clusters in a wet chemical process they can maintain their superparamagnetic behaviour due to weak magnetic coupling between the individual subunits [19, 27, 28].

To show that PT MCD can indeed provide images of single nanoparticles with magnetic contrast and to discern magnetic effects from shape effects (geometric chirality) we spin-coated the nominally $200\,\mathrm{nm}$-diameter magnetite particles on a glass surface at very low surface coverage ($\sim$1 NP/10 $\mu\mathrm{m}^2$). We then obtain a series of four images as displayed on a selected example in figure 5.2 (a-d):

(a) A photothermal image, which allows us to estimate the particles' volume due to the linear relationship between absorption cross section and volume. (b) A photothermal CD image in the absence of an external magnetic field, which allows us to determine the geometric CD of individual particles. (c) and (d) PT CD images obtained with axial magnetic fields of positive (c) and negative sign (d). The axial magnetic field gives rise to a polar Kerr effect which can be detected by our setup via PT MCD.

The PT scan (figure 5.2 a) indicates a broad size distribution of the particles. Based on the correlated SEM images, (see figure S5.1) we estimate the size of the three bright particles to be about $400\,\mathrm{nm}$. Upon application of an external magnetic field we find a strong contrast in the CD images (figure 5.2 (c-d)), indicating the presence of a net magnetic moment in the particles, which generates a strong MCD signal. We find that all particles exhibit the same sign of CD and that, upon inversion of the magnetic field, we invert the sign of the CD signal, corroborating the MCD nature of the signal. We then compare the relative magnetic susceptibility of the individual magnetite particles by calculating their g-factor, which is defined as

$$g = 2 \cdot \frac{A_{lcp} - A_{rcp}}{A_{lcp} + A_{rcp}}, \tag{5.1}$$

where A_{lcp} and A_{rcp} are the absorptivities for left- and right-handed circular polarized light, respectively. We can simply retrieve the g-factor by calculating the ratio of CD over PT signals. The MCD signal is proportional to the magnetic moment while the PT signal is proportional to the volume of the particle and thus to its number of unit cells. By taking their ratio we obtain a value that scales with the magnetic moments per unit cell. We find that all particles have similar g-factors, close to 1% at a magnetic field of $0.4\,\mathrm{T}$, indicating a similar magnetic susceptibility. Figure 5.2(b) shows a CD scan in the absence of a magnetic field. We find that even in the absence of a magnetic field some particles exhibit CD. We assign this offset CD to geometric chirality that can occur in quasi-spherical particles [21, 29] and is different from particle to particle (see figure S5.5 and S5.6).

Thanks to the excellent SNR of the measurements in figure 5.2, we are not limited to measurements of the MCD close to the saturation magnetization of the magnetite particles. This motivated us to obtain the magnetization curve of a single $\sim$400 nm magnetite particle. We did this by focusing on a single $400\,\mathrm{nm}$-diameter particle and measuring its MCD signal while the magnetic field's strength and sign were varied by altering the magnet's distance to the sample and flipping its orientation. In order to obtain the magnetic field strength as a function of distance we performed a calibration measurement (see figure S5.4) using a Gaussmeter (Hirst Magnetic Instruments GM08). The resulting magnetisation curve of

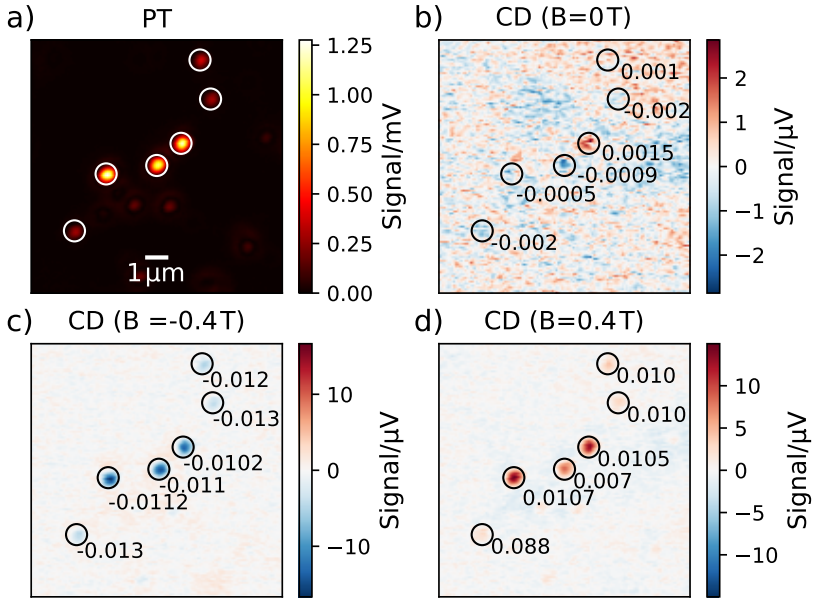

Figure 5.2: Photothermal (a) and circular dichroism measurements (b-d) of nominally 200 nm-diameter magnetite particles exposed to different external magnetic fields. The actual size of the three brighter particles in the center is measured by correlative SEM imaging and falls into the range of 300-400 nm (see figure S5.1 and S5.2). For details about the sizing see figure S5.1-S5.2. The integration time is 20 ms per pixel. The magnetic field strength for b), c) and d) is 0 T, −0.4 T and 0.4 T, respectively. Individual particles exhibiting considerable MCD are marked with circles and numbers indicate their g-factors. At an external field of 0.4 T the g-factors are close to 1% for most particles.

a single magnetite particle is displayed in figure 5.3. The shape of the curve displays superparamagnetic behaviour, as evident from the absence of a remanent magnetization. The field we apply here (∼0.43 T) is larger than the saturation field of our nanoparticles (subunit size of 8-13 nm) [31] and below the saturation field of bulk magnetite [32]. To exclude possible effects of the external magnetic field on the optical elements that may induce an artificial CD, we performed a reference measurement on a 100 nm-diameter gold nanoparticle (see orange data points in figure 5.3). Gold is diamagnetic and therefore has a very small magnetic susceptibility [33]. The small susceptibility should result in a negligible MCD response, compared to magnetite. If the CD signal of the magnetic particles was due to the external magnetic field affecting the setup (i.e. the objective) we would also expect a response of the gold nanoparticles upon application of an external magnetic field. The shape of the gold nanoparticle's PT CD curve shows that this particle had no significant response to the external magnetic field, within experimental noise. Together, these observations provide strong evidence that the observed strong MCD response of our magnetite particles is

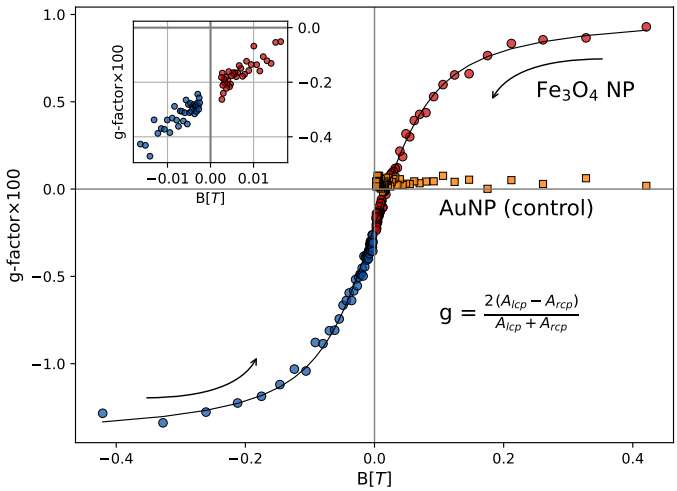

Figure 5.3: Magnetization curve of a single $\sim$400 nm-diameter magnetite particle measured by PT CD in hexadecane. The shape displays superparamagnetic behaviour. The integration time is 1 s per point. The inset shows a magnified view of the magnetite nanoparticle's magnetization curve at small fields. Arrows indicate the sweep direction of the magnetic field (strong-to-weak). The orange data points show a reference measurement on a 100 nm-diameter gold nanoparticle, here only for positive magnetic fields. The solid line is a fit with a Langevin function: ($\coth(x)$-1/x, where x = μ_B/k_BT) [30]. The resulting magnetic moment of the composing nanoparticles is about 10,000 Bohr magnetons.

indeed induced by their magnetic moment. The shape of the curve and the saturation magnetization that we find are in reasonable agreement with ensemble measurements for other magnetite nanoparticles [34], however, the strength of the MCD effect (g-factor) that we observe is one order of magnitude larger than found elsewhere in ensemble measurements [35, 36]. One reason for the difference in g-factor could be a different subunit size of the particles used in these studies which were between 3.4 and 6.9 nm, compared to 8-13 nm for our particles. Nanocrystals of smaller size exhibit a smaller saturation magnetization due to a magnetic dead layer [31]. Another possible reason for the difference could be the different measurement modality. While refs [35, 36] measure in a transmission geometry thereby probing extinction we employ PT contrast, probing absorption. Extinction measurements and absorption are not in general equivalent as the extinction measurement also entails a considerable scattering contribution.

5.3. Conclusion and outlook

We have demonstrated a PT-based optical imaging method that enables the study of single-particle magnetization via PT MCD. The excellent sensitivity of PT imaging allowed us to obtain single-particle magnetization curves. Our single-particle and absorption based measurements revealed g-factors that are one order of magnitude higher than the ones found

by ensemble extinction-based studies [35, 36]. The images presented in figure 5.2 were obtained by scanning the sample with a piezo-stage and thus require long image acquisition times. Recent advances in the field of wide-field PT imaging [37–39], that use cameras instead of confocal scanning, could open the possibility for faster image acquisition with magnetic contrast. PT imaging is particularly well suited for studying the absorption of small particles, since the absorption scales with the volume. From our signal-to-noise ratios and the available laser powers of probe and heating lasers we estimate that the magnetic moments of single-domain magnetite particles with sizes down to $20\,\mathrm{nm}$ can be studied with our technique. We believe that photothermal magnetic circular dichroism (PT MCD) is a promising technique for future studies of magnetic nanoparticles as it is easy to implement in existing PT setups and does not suffer from the drawbacks of complex instrumentation and restrictive demands on experimental environments imposed by other methods like XMCD, MFM or scanning SQUIDs.

5.4. Supplementary information

5.4.1. Correlated SEM images of nominally 200 nm particles.

Figure S5.1 shows a SEM image of the same area as the images of figure 5.2. The sample surface is partially sullied with glass debris that probably came during the manufacturing process of markers on the glass slide (ibidi Gridded Glass Coverslips). The diameter of the encircled particles is significantly larger than $200\,\mathrm{nm}$. However, the SEM scan, which was performed under 30° of the sample, also reveals that the particles are not spherical in shape. In fact they are rather flat. The three marked particles on the top right, for example, have the similar strength in PT signal and therefore should have the same volume. From the SEM images the particle looks smaller in diameter than the lower ones but appears significantly higher. From the tilted SEM images and the estimated height we estimate the volume of the particles to be equivalent to a sphere of $\sim 400\,\mathrm{nm}$ in diameter.

5.4.2. PT of 20 nm magnetite particles

Due to the small tilt of the SEM scans in figure S5.1 (30°) and the crude shape of the particles we wanted to recheck the particle's size by comparing their absorption with well characterized $20\,\mathrm{nm}$-diameter (Nanocomposix) magnetite particles. Based on the PT signal of the $20\,\mathrm{nm}$-diameter magnetite particles, assuming that the absorption scales linearly with the volume, we can extrapolate the size of the supposedly $200\,\mathrm{nm}$ particles. The PT scans of three areas of a sample of spin-coated $20\,\mathrm{nm}$-diameter magnetite particles are shown in figure S5.2. Note the presence of a weak background PT signal that probably occurs due to weak absorption in the glass slide. This is only visible due to the weak absorption of the magnetite nanoparticles and the relatively large heating power ($\sim 60\,\mathrm{mW}/\mu\mathrm{m}^2$). Figure S5.3 (c) shows a histogram of the PT signals of 193 magnetite nanoparticles and (d) a TEM micrograph, provided by the manufacturer. The absorption scales linearly with the particle's volume. Accordingly the histogram of the cubic root of PT signals scales linearly with the particle size. Figure S5.3 (a) and (b) show the histogram of the cubic root of PT signals and the histogram of diameters measured by the manufacturer via TEM, respectively. The

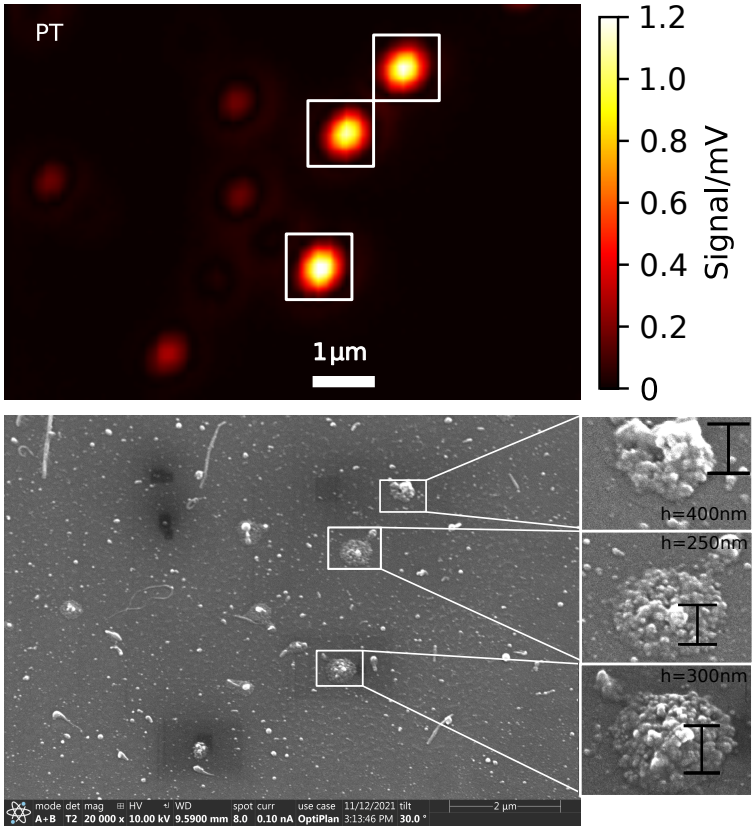

Figure S5.1: Correlated SEM images of the scanned area in figure 5.2. The top panel shows the PT image of the same sample region, which was rotated and mirrored compared to figure 5.2 to fit with the SEM micrograph in the lower panel. The square boxes are guides for the eye. The particles diameter is much larger than the 200 nm given by the manufacturer, however, the tilted SEM scan (30°) indicates that the particles are rather flat. The black bar indicates the estimated heights of the particles.

shape of the histogram of particle sizes based on the PT measurements agrees well with the histogram based on the manufacturer's TEM measurements (c,d). We can therefore assume that the center of the histogram in (a) corresponds to the center of the histogram in (b).

Based on the ratio of optical powers ($\times$48) and the ratio of the respective PT signals ($\times$1/52) we estimate the size of the supposedly 200 nm particles to be $\sim$300 nm. We therefore believe that the size of 400 nm that we found by SEM imaging is reasonable.

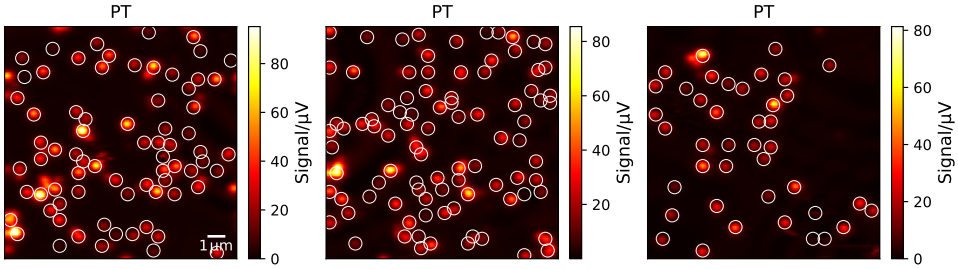

Figure S5.2: PT scans of 193 20 nm-diameter particles from 3 different areas on the sample. The white circles are guides for the eye.

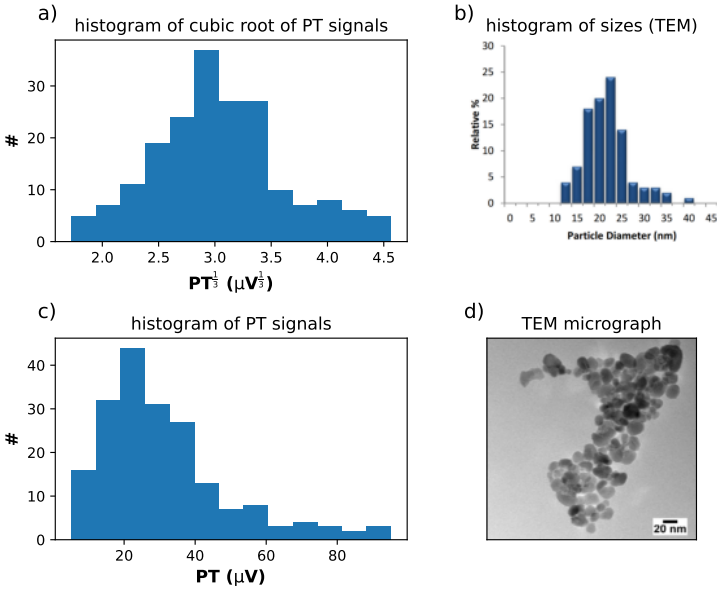

Figure S5.3: (a) and (c) histogram of PT signals of 193 20 nm-diameter nanoparticles. b) size histogram from the manufacturer (NanoComposix) based on TEM imaging from the same particle batch. (d) TEM micrograph of the particles.

5.4.3. Calibration of magnetic field vs distance

Figure S5.4 shows the magnetic field dependence on distance of the permanent magnet we used to vary the magnetic field, measured with a Gaussmeter (Hirst Magnetic Instruments GM08) and the fitted data that is used to interpolate the field values at the positions relevant for the measurements of figure 5.3. We fit the data with the following phenomenological

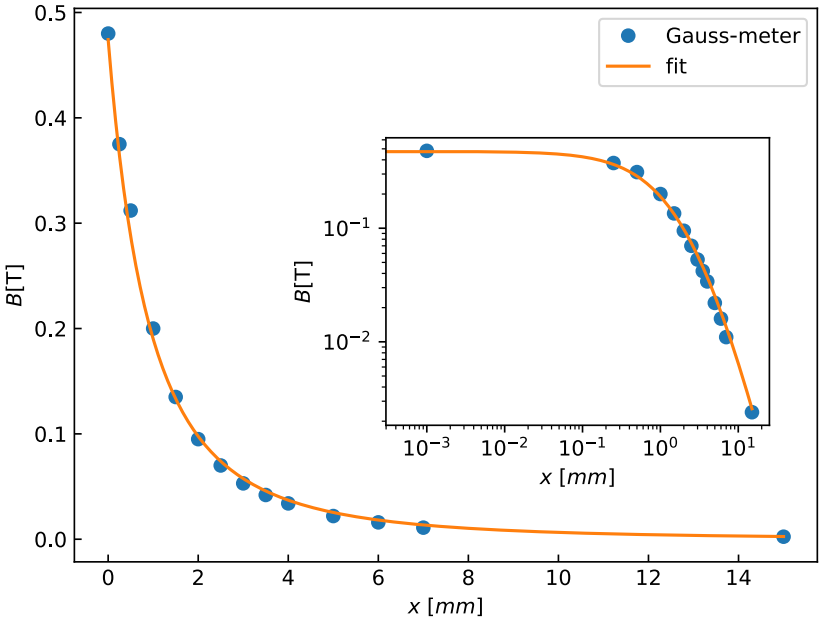

Figure S5.4: Measured dependence of magnetic field on distance (blue) and a phenomenological fit (orange). The magnetic field was measured wit a Gaussmeter. The insert shows a double logarithmic plot of the measured and fitted field dependence on distance.

function:

$$B(x) = \frac{a}{(x+b)^2} \cdot \frac{1}{(1+x/c)} \tag{5.2}$$

For small distances we assume a a/(x+b)^2 dependence of the field, since the magnet is very long (monopole limit) with respect to its diameter. To improve the fit for larger distances where dipole effects come into play, we multiply by a factor of 1/(1+x/c). The respective values of a,b and c are: $1.85\,\mathrm{T{\cdot}mm^2}$,$1.97\,\mathrm{mm}$ and $10.04\,\mathrm{mm}$.

5.4.4. Magnetic-field-dependent PT-CD curves

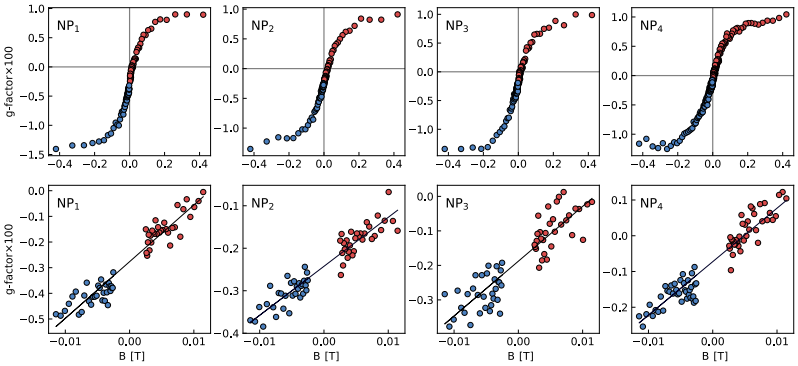

Figure S5.5: Magnetic-field-dependent circular dichroism curves of four different magnetite particles of ∼400 nm in diameter. The lower row shows a magnified view of the magnetization curve at smaller magnetic fields with a linear fit.

Figure S5.5 shows the magnetic field dependent PT-CD curves of four magnetite particles (NP1-NP4). All particles show similar g-factors indicating similar magnetic susceptibility. We can observe that the two parts of the magnetization curve (red and blue) seem to meet at zero magnetic field, within noise. This indicates the absence of a remanence magnetization. The offset values all have the same sign. This might give rise to the assumption of a bias in the the CD measurements, due to the particles themselves or due to the method. We have shown in chapter 3 that our optical method is not subject to artificial bias signals. To rule out biasing effects of the particles we used the same sample as for the magnetization-curve measurements, and performed a MCD scan including many particles.

Figure S5.6 (a) shows a PT and three CD images with (b) zero, (c) positive and (d) negative magnetic fields applied. When the magnetic field is turned off (figure S5.6 (b)) we still observe some residual CD signal that we relate to geometric chirality. We observe both positive and negative CD signals at zero external field. We therefore conclude that the four negative offset signals in figure S5.5 are not systematic.

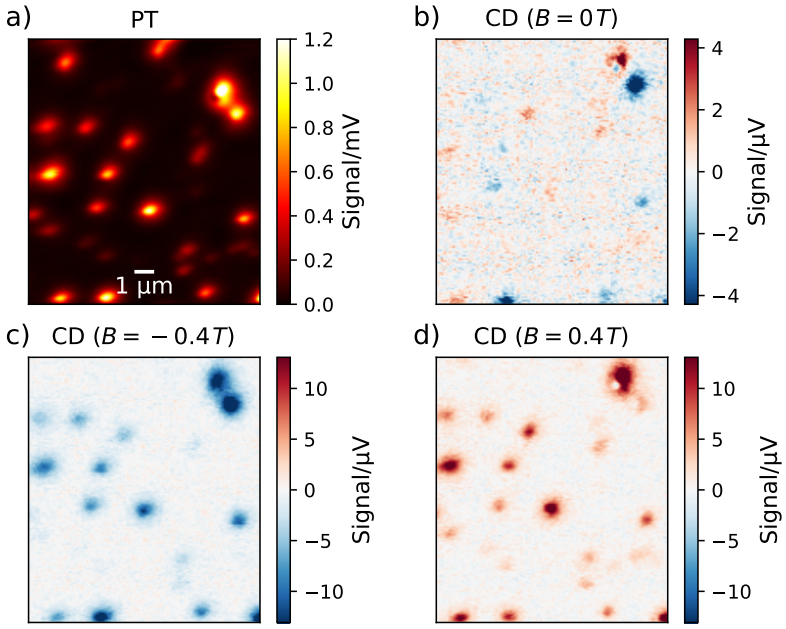

Figure S5.6: Photothermal (a) and photothermal CD images (b-d) a of nominally 200 nm superparamagnetic magnetite particles at different external magnetic fields.

References

[1] Stanciu, C.; Hansteen, F.; Kimel, A.; Kirilyuk, A.; Tsukamoto, A.; Itoh, A.; Rasing, T. All-Optical Magnetic Recording With Circularly Polarized Light. *Physical Review Letters* **2007**, *99*, 047601.

[2] Bigot, J.-Y.; Vomir, M.; Beaurepaire, E. Coherent Ultrafast Magnetism Induced by Femtosecond Laser Pulses. *Nature Physics* **2009**, *5*, 515–520.

[3] Mahmoudi, M.; Sant, S.; Wang, B.; Laurent, S.; Sen, T. Superparamagnetic Iron Oxide Nanoparticles (SPIONs): Development, Surface Modification and Applications in Chemotherapy. *Advanced Drug Delivery Reviews* **2011**, *63*, 24–46.

[4] Reiss, G.; Hütten, A. Magnetic Nanoparticles: Applications Beyond Data Storage. *Nature Materials* **2005**, *4*, 725–726.

[5] Shen, S.; Wang, S.; Zheng, R.; Zhu, X.; Jiang, X.; Fu, D.; Yang, W. Magnetic Nanoparticle Clusters for Photothermal Therapy With Near-Infrared Irradiation. *Biomaterials* **2015**, *39*, 67–74.

[6] Kobayashi, T. Cancer hyperthermia using magnetic nanoparticles. *Biotechnology journal* **2011**, *6*, 1342–1347.

[7] Skumryev, V.; Stoyanov, S.; Zhang, Y.; Hadjipanayis, G.; Givord, D.; Nogués, J. Beating the Superparamagnetic Limit With Exchange Bias. *Nature* **2003**, *423*, 850–853.

[8] Weller, D.; Moser, A. Thermal Effect Limits in Ultrahigh-Density Magnetic Recording. *IEEE Transactions on Magnetics* **1999**, *35*, 4423–4439.

[9] Néel, L. Théorie du traînage magnétique des ferromagnétiques en grains fins avec applications aux terres cuites. *Ann. Géophys.* **1949**, *5*, 99–136.

[10] Vasyukov, D.; Anahory, Y.; Embon, L.; Halbertal, D.; Cuppens, J.; Neeman, L.; Finkler, A.; Segev, Y.; Myasoedov, Y.; Rappaport, M. L., et al. A Scanning Superconducting Quantum Interference Device With Single Electron Spin Sensitivity. *Nature Nanotechnology* **2013**, *8*, 639–644.

[11] Wernsdorfer, W.; Sessoli, R. Quantum phase interference and parity effects in magnetic molecular clusters. *Science* **1999**, *284*, 133–135.

[12] Buchner, M.; Höfler, K.; Henne, B.; Ney, V.; Ney, A. Tutorial: Basic Principles, Limits of Detection, and Pitfalls of Highly Sensitive SQUID Magnetometry for Nanomagnetism and Spintronics. *Journal of Applied Physics* **2018**, *124*, 161101.

[13] Kazakova, O.; Puttock, R.; Barton, C.; Corte-León, H.; Jaafar, M.; Neu, V.; Asenjo, A. Frontiers of Magnetic Force Microscopy. *Journal of Applied Physics* **2019**, *125*, 060901.

[14] Weis, T.; Krug, I.; Engel, D.; Ehresmann, A.; Hoeink, V.; Schmalhorst, J.; Reiss, G. Characterization of Magnetic Force Microscopy Probe Tip Remagnetization for Measurements in External In-Plane Magnetic Fields. *Journal of Applied Physics* **2008**, *104*, 123503.

[15] Balan, A.; Derlet, P. M.; Rodríguez, A. F.; Bansmann, J.; Yanes, R.; Nowak, U.; Kleibert, A.; Nolting, F. Direct Observation of Magnetic Metastability in Individual Iron Nanoparticles. *Physical Review Letters* **2014**, *112*, 107201.

[16] Han, B.; Gao, X.; Lv, J.; Tang, Z. Magnetic Circular Dichroism in Nanomaterials: New Opportunity in Understanding and Modulation of Excitonic and Plasmonic Resonances. *Advanced Materials* **2020**, *32*, 1801491.

[17] Mason, R. W. *A Practical Guide to Magnetic Circular Dichroism Spectroscopy*; Wiley: New Jersey, 2007.

[18] Coey, J. M. D. *Magnetism and Magnetic Materials*; Cambridge University Press: Cambridge, 2010; Chapter 5.

[19] Reichel, V.; Kovács, A.; Kumari, M.; Bereczk-Tompa, É.; Schneck, E.; Diehle, P.; Pósfai, M.; Hirt, A. M.; Duchamp, M.; Dunin-Borkowski, R. E., et al. Single Crystalline Superstructured Stable Single Domain Magnetite Nanoparticles. *Scientific Reports* **2017**, *7*, 1–8.

[20] Kleibert, A.; Balan, A.; Yanes, R.; Derlet, P. M.; Vaz, C. A.; Timm, M.; Rodríguez, A. F.; Béché, A.; Verbeeck, J.; Dhaka, R. S., et al. Direct Observation of Enhanced Magnetism in Individual Size and Shape-Selected 3 D Transition Metal Nanoparticles. *Physical Review B* **2017**, *95*, 195404.

[21] Spaeth, P.; Adhikari, S.; Le, L.; Jollans, T.; Pud, S.; Albrecht, W.; Bauer, T.; Caldarola, M.; Kuipers, L.; Orrit, M. Circular Dichroism Measurement of Single Metal Nanoparticles Using Photothermal Imaging. *Nano Letters* **2019**, *19*, 8934–8940.

[22] Spaeth, P.; Adhikari, S.; Baaske, M. D.; Pud, S.; Ton, J.; Orrit, M. Photothermal Circular Dichroism of Single Nanoparticles Rejecting Linear Dichroism by Dual Modulation. *ACS nano* **2021**, *15*, 16277–16285.

[23] Fontijn, W. F. J.; van der Zaag, P. J.; Devillers, M. A. C.; Brabers, V. A. M.; Metselaar, R. Optical and magneto-optical polar Kerr spectra of Fe_3O_4 and Mg^{2+}- or Al^{3+}-substituted Fe_3O_4. *Phys. Rev. B* **1997**, *56*, 5432–5442.

[24] Adhikari, S.; Spaeth, P.; Kar, A.; Baaske, M. D.; Khatua, S.; Orrit, M. Photothermal Microscopy: Imaging the Optical Absorption of Single Nanoparticles and Single Molecules. *ACS Nano* **2020**, *14*, 16414–16445.

[25] Berova, N.; Nakanishi, K.; Woody, R. W. *Circular Dichroism: Principles and Applications*; Wiley: New Jersey, 2000.

[26] Oppeneer, P. M. Theory of the Magneto-Optical Kerr Effect in Ferromagnetic Compounds. Habilitation, Technische Universität Dresden, Dresden, 1999.

[27] Ge, J.; Hu, Y.; Biasini, M.; Beyermann, W. P.; Yin, Y. Superparamagnetic Magnetite Colloidal Nanocrystal Clusters. *Angewandte Chemie International Edition* **2007**, *46*, 4342–4345.

[28] Maqbool, Q.; Jung, A.; Won, S.; Cho, J.; Son, J. G.; Yeom, B. Chiral Magneto-Optical Properties of Supra-Assembled Fe3O4 Nanoparticles. *ACS Applied Materials & Interfaces* **2021**,

[29] Fan, Z.; Govorov, A. O. Chiral Nanocrystals: Plasmonic Spectra and Circular Dichroism. *Nano Netters* **2012**, *12*, 3283–3289.

[30] Chen, D.-X.; Sanchez, A.; Taboada, E.; Roig, A.; Sun, N.; Gu, H.-C. Size determination of superparamagnetic nanoparticles from magnetization curve. *Journal of Applied Physics* **2009**, *105*, 083924.

[31] Safronov, A.; Beketov, I.; Komogortsev, S.; Kurlyandskaya, G.; Medvedev, A.; Leiman, D.; Larrañaga, A.; Bhagat, S. Spherical Magnetic Nanoparticles Fabricated by Laser Target Evaporation. *AIP Advances* **2013**, *3*, 052135.

[32] Cornell, R. M.; Schwertmann, U. *The Iron Oxides: Structure, Properties, Reactions, Occurrences and Uses*; Wiley: New Jersey, 2003.

[33] Zaitoun, M.; Mason, W. R.; Lin, C. Magnetic Circular Dichroism Spectra for Colloidal Gold Nanoparticles in Xerogels at 5.5 K. *The Journal of Physical Chemistry B* **2001**, *105*, 6780–6784.

[34] Yuan, Y.; Rende, D.; Altan, C. L.; Bucak, S.; Ozisik, R.; Borca-Tasciuc, D.-A. Effect of Surface Modification on Magnetization of Iron Oxide Nanoparticle Colloids. *Langmuir* **2012**, *28*, 13051–13059.

[35] Yao, H.; Ishikawa, Y. Finite Size Effect on Magneto-Optical Responses of Chemically Modified Fe3O4 Nanoparticles Studied by MCD Spectroscopy. *The Journal of Physical Chemistry C* **2015**, *119*, 13224–13230.

[36] Ito, D.; Yao, H. Dominant Role of Iron Oxides in Magnetic Circular Dichroism of Plasmonic-Magnetic Au-$Fe_{3-x}O_4$ Heterodimer Nanostructure. *Journal of Magnetism and Magnetic Materials* **2020**, *500*, 166385.

[37] Bai, Y.; Zhang, D.; Lan, L.; Huang, Y.; Maize, K.; Shakouri, A.; Cheng, J. X. Ultrafast Chemical Imaging by Widefield Photothermal Sensing of Infrared Absorption. *Science Advances* **2019**, *5*.

[38] Li, M.; Razumtcev, A.; Yang, R.; Liu, Y.; Rong, J.; Geiger, A. C.; Blanchard, R.; Pfluegl, C.; Taylor, L. S.; Simpson, G. J. Fluorescence-Detected Mid-Infrared Photothermal Microscopy. *Journal of the American Chemical Society* **2021**, *143*, 10809–10815.

[39] Liebel, M.; Camargo, F. V. A.; Cerullo, G.; van Hulst, N. F. Widefield Phototransient Imaging for Visualizing 3D Motion of Resonant Particles in Scattering Environments. 2021; `https://arxiv.org/abs/2108.05124v1`, accessed 13 September 2021.

6

Conclusion and outlook

In this thesis we focus on the design of an optical setup based on photothermal imaging to measure the circular dichroism (CD) of single nanoparticles. Chapters 2 and 3 describe the development of the optical technique and how to avoid pitfalls that may create artefact signals. We show by performing proof-of-principle experiments that the technique is indeed sensitive to CD of single nanoparticles, with sensitivities down to g-factors of 3×10^{-4}, and can in principle be extended for spectral measurements. In the following chapter we apply photothermal circular dichroism (PT CD) to study the CD of chiral plasmonic nanoparticles and try to find a relation between the chiral geometric features and the measured CD signal. In chapter 5 we show that PT CD facilitates optical studies of magneto-optic phenomena at the single-particle level.

Photothermal circular dichroism When we perform a modulation of polarization to study the minute dichroism effects of a nanoparticle residing in a focused laser beam, we are prone to artefacts due to even the slightest beam misalignments, because of the strong focusing conditions. To avoid these artefacts it therefore judicious to use weakly focused light. On the other hand when we are interested in imaging applications of nanometer-sized objects we seek for diffraction-limited optical resolution and therefore require a tightly focused beam. Photothermal imaging provides a simple solution to that problem as it is a two-laser technique. We can use a strongly focused probe laser, which provides diffraction-limited resolution, and we can choose to focus the heating beam only weakly to avoid artefacts linked to strongly focused polarized light. Photothermal imaging comes with another benefit for the measurement of the CD of single nanoparticles as it measures, to first approximation, the effect of a thermal lens and is therefore a true absorption signal free from scattering contributions. We show, by employing a simple square-wave modulation of the polarization, that we can indeed tell apart the two enantiomers of lithographically manufactured chiral nanostructures. However, such a simple square-wave modulation scheme has severe restrictions when it comes to measurements of either weak CD g-factors or particles with substantially larger linear dichroism (LD) compared to their CD values. This restrictions are linked to the polarization modulator itself as it gives rise to a residual intensity modulation on top of the polarization modulation and, additionally, the single-modulation scheme may lead to

leakage of LD into the CD signal. We show that this leakage of LD into CD and the effect of residual intensity modulation can drastically be reduced when performing a polarization modulation based on two polarization modulators in series. This dual-modulation scheme allows us to perform reliable CD measurements even on rod-like nanoparticles which naturally exhibit strong LD effects. We achieved measurements of small CD g-factors of only a few 10^{-4} on single gold nanoparticles, which are only one order-of-magnitude away from ensemble techniques that average the signal over millions of particles. On the other hand, single-particle measurements of such high sensitivity require large heating powers and might lead to thermally-induced reshaping effects that alter the particles' shape and properties. Better contrast mechanisms such as fluorescence-detected PT or measurements performed in super-critical xenon could allow for comparable sensitivity at much reduced heating powers. We envisage that, when augmented with a suitable tunable heating laser, PT CD would also facilitate studies of the spectral chiroptical properties of plasmonic nanoparticles on the single-nanoparticle level.

Plasmon-coupled circular dichroism PCCD Circular birefringence (CB) is the refractive counterpart of CD and can occur in molecules even at wavelength where they do not absorb. A liquid exhibiting CB has different refractive indices for left- and right-circularly polarized light. Consequently, when a plasmonic nanoparticle is placed in this liquid, as its resonance condition is dependent on the surrounding liquid's refractive index, we expect to observe two shifted plasmon resonances depending on whether we shine left- or right-circular polarized light on the particle. The shifted resonance gives rise to a circular polarization-dependent differential absorption - i.e. to CD. So in a sense the liquid's CB gets transferred to CD in the presence of the plasmonic nanoparticle. Our measurements on the PCCD of a $100\,\mathrm{nm}$ gold nanoparticle immersed in the chiral molecule carvone, despite our good sensitivity of g-factors down to 3×10^{-4}, did not deliver any measurable CD signal. We conclude that spherical nanoparticles, due to their broad plasmon resonance, are not ideal to measure PCCD induced by differences in refractive index $n_{LCP} - n_{RCP} = \Delta n$ which are typically on the order of 10^{-4}. We propose to use plasmonic particles which are more sensitive to minute refractive index changes. Such a system could for example be a nanorod or a pair of nanospheres at close distance. The near field at the tip of the nanorod, or in the gap in between the nanoparticles should be much more sensitive to minute changes of the refractive index. However, in this case great care must be taken to avoid heat induced reshaping that would result in a broadened resonance and therefore in a loss of sensitivity.

Correlation of shape chirality and CD In chapter 4 we looked at the chiroptical response of wet chemically synthesized particles and found that the single-particle measurements display a striking difference in the chiroptical behaviour compared to the ensemble measurements. Not only did we find that the strength of the CD signal varies strongly between the particles, we also find CD signals of opposite sign. The wet chemical synthesis process of chiral nanoparticles, assisted by chiral molecules, aims at creating geometric chiral features of a certain handedness. However, when we look at the geometric chirality (here the helicity) on the single-particle level, by performing electron tomography measurements, we find regions of opposite handedness even within one particle. When we compare the single-particle optical signal to the geometric chirality we find a weak correlation between the average helicity and the chiroptical signal. That means that the shape alone does not allow for a straightforward prediction of the chiroptical signal. To investigate the influence

of plasmonic resonances and wavelength dependence, we perform similar measurements on quasi-achiral gold nanoparticles and found that even if we take into account plasmonic effects and simulate the optical response, based on the shape of the particle, we find no clear link between the measured optical signal and the one retrieved from BEM simulations. We therefore conclude that there must be other contributions as for example surface ligands on the particles or the presence of the substrate, that induce an additional symmetry-breaking and therefore affect the particles' chiroptical response. Additionally, the ensemble measurements are performed with the particles in solution, allowing for arbitrary orientations and therefore the ensemble measurement not only averages different particles it also averages different particle orientations. One possible way to test the influence of substrate and the different orientations in our single-particle measurements would be to trap the particles optically with an NIR beam and then perform a CD measurements. Trapping the particles by a third NIR beam inside a liquid, by for example using two microscope objectives facing each other like in 4Pi microscopy, would allow the particle to freely rotate and also remove the substrate-induced symmetry break and maybe allow for a better comparison of ensemble and single-particle measurements.

Measuring the magnetization of single nanoparticles Circular dichroism occurs in chiral molecules or nanoparticles due to a lack of mirror symmetry. However, CD also occurs in magnetic materials irrespective of shape due to Faraday or Kerr effects. Magnetic moments on nano-sized objects are typically measured by MFM or scanning SQUID's due to their high sensitivity and resolution. Optical techniques in the visible regime, like Kerr microscopy or conventional magnetic circular dichroism spectrometers based on a transmission geometry are restricted to bulk or ensemble measurements. In a proof-of-principle experiment, we show that PT CD is sensitive to the polar Kerr effect in single magnetite nanoparticles. By applying a tunable external magnetic field and simultaneously following the CD signal, we recorded a magnetization curve and confirm the superparamagnetic behaviour of these particles, due to absence of a remanent magnetization. If combined with a suitable heating and probing laser and if the measurements are performed in super-critical conditions, we envisage to perform studies of the random flipping of the magnetization of single-domain superparamagnetic particles.

Samenvatting

Circulair dichroïsme (CD), het verschil in absorptie tussen links en rechts circulair gepolariseerd licht, komt voor in chirale moleculen en deeltjes met gebroken spiegelsymmetrie. Het is van belang dit te bestuderen in de biologische context, aangezien veel moleculen die in de natuur voorkomen, chiraal zijn en de chiraliteit van een molecuul van invloed is op hoe de interactie met andere chirale moleculen uitziet. Onlangs kreeg de studie van CD steeds meer aandacht op het gebied van plasmonica. Aan de ene kant wordt voorgesteld plasmonische nanodeeltjes te gebruiken als sensoren om de zwakke CD van biomoleculen te versterken en aan de andere kant kwamen chirale plasmonische deeltjes in de focus van onderzoek vanwege hun exotische optische eigenschappen. Tot nu toe bestond er, voor zover wij weten, geen techniek die CD meet in een echte absorptiemeting. Ons streven begon dus met het ontwerp van een optische techniek om CD te bestuderen, waarbij absorptie als contrastmechanisme wordt gebruikt. Daarom hebben we gebruik gemaakt van fotothermische beeldvorming. Fotothermische beeldvorming meet rechtstreeks de absorptie van nanodeeltjes via een thermische lens. Dankzij de hoge gevoeligheid die de techniek biedt, kunnen metaaldeeltjes met een diameter tot enkele nm of zelfs enkele moleculen via fotothermische beeldvorming worden gedetecteerd. Om dichroïsme-effecten te bestuderen, hebben we eerst een polarisatie-modulatieschema gebruikt met behulp van een EOM, die de polarisatie tussen links- en rechtshandig circulair gepolariseerd licht moduleert op een blokgolfwijze. We vermijden artefacten als gevolg van sterk gefocust gepolariseerd licht door gebruik te maken van Koehler-verlichting voor de verwarmingsstraal en we hebben desondanks diffractie-beperkte resolutie vanwege de sterk gefocuste sondestraal.

Tijdens het bouwen van de opstelling realiseerden we ons dat we optische componenten zoals dichroïsche elementen, spiegels of bundelsplitsers onder grote hoeken koste wat kost moeten vermijden. In een proof-of-principle-experiment van nano-gefabriceerde chirale goudstructuren van verschillende chiraliteit, konden wij laten zien dat onze microscoop inderdaad gevoelig was voor CD. De hoge gevoeligheid die fotothermische beeldvorming biedt stelde ons zelfs in staat om de minieme CD-effecten te meten die in quasi sferische nanodeeltjes voorkomen. We realiseerden ons echter al gauw dat onze methode niet vrij was van artefacten. We identificeerden twee artefacten, residuele intensiteitsmodulatie van de modulatoren en lekkage van lineair dichroïsme naar circulair dichroisme, wat onze metingen zou kunnen beïnvloeden. We hebben beide artefacten kunnen verwijderen door een dubbele polarisatie-modulatie toe te passen met twee modulatoren in serie maar met verschillende modulatiefrequenties. Door zorgvuldige optische uitlijning en door te meten op de som van beide modulatiefrequenties, konden we de artefacten onderdrukken. Dit stelde ons in staat om differentiële absorptie-anisotropieën (g-factor) van afzonderlijke nanodeeltjes te bestuderen tot op de enkele 10^{-4} schaal.

Het nieuwe modulatieschema, dat nu vrij was van artefacten, stelde ons in staat om het circulaire dichroïsme van langwerpige, schroefachtige colloïdale plasmonische nanodeeltjes te bestuderen. We waren vooral geïnteresseerd in de correlatie tussen hun geometrische

kenmerken en de chiroptische eigenschappen van deze deeltjes. Daarom hebben we gecorreleerde elektronentomografie en fotothermische CD onderzoeken uitgevoerd. Uit de optische studies hebben we gevonden dat de chiroptische handigheid van deeltje tot deeltje kan variëren. Uit de gereconstrueerde morfologie ontdekten we, dat een enkel deeltje tegelijkertijd zowel links- als rechtshandige geometrische kenmerken kan bevatten. We konden echter alleen een kwalitatieve correlatie vinden tussen de algemene geometrische chiraliteit en het optische, circulaire dichroïsme-signaal. Een puur geometrische beschouwing is dan zeker ook niet geschikt voor plasmonische effecten.

Daarom gebruikten we in een tweede experiment van gecorreleerde optische en elektronentomografie quasi achirale deeltjes met sferische geometrie, waardoor we in staat waren om elektromagnetische simulaties uit te voeren. We ontdekten, dat kwalitatief, deeltjes, die in de simulaties kleine CD-signalen opleverden ook zwakke CD vertoonden in de optische metingen. We vonden echter ook verschillende deeltjes met een ernstige discrepantie tussen het optische experiment en de simulaties op basis van de geometrie van de deeltjes. We kwamen daarom tot de conclusie dat er nog andere effecten, zoals het substraat waarop de deeltjes zich bevinden of liganden op de oppervlakte van de nanodeeltjes het CD-signaal kunnen beïnvloeden.

In hoofdstuk 5 hebben we vervolgens het circulaire dichroïsme-signaal bestudeerd, dat wordt vertoond, door magnetische nanodeeltjes via het magneto-optische Kerr-effect. We kozen voor superparamagnetische deeltjes omdat we hun magnetisatie kunnen afstemmen met een relatief zwak extern magnetisch veld. Superparamagnetisme is een fenomeen dat wordt aangetroffen in kleine deeltjes van ferro- of ferrimagnetisch materiaal. Bij een gegeven temperatuur, wanneer de grootte van het magnetische domein onder een bepaalde drempel ligt, is de thermische energie groot genoeg om de oriëntatie van het magnetische domein om te draaien. Hoewel het deeltje een magnetisch moment draagt, aangezien dit moment erg snel kan omslaan, lijkt het deeltje tijdgemiddeld geen magnetisch moment te dragen. Superparamagnetische deeltjes waren daarnaast een perfect testmonster omdat onze optische techniek geen onderscheid kan maken tussen door geometrie geïnduceerde CD en magnetische CD. Bij afwezigheid van een extern magnetisch veld hebben superparamagnetische deeltjes geen magnetisch moment. Wanneer ze echter worden blootgesteld aan een extern magnetisch veld, krijgen ze een sterke magnetisatie. De CD-meting bij afwezigheid van een magnetisch veld dient daarom als een nulmeting om de geometrische bijdrage van het CD-signaal te corrigeren. Door de CD van magnetiet deeltjes van $\sim$400 nm te meten, konden we aantonen dat we het magnetische contrast van deze deeltjes kunnen identificeren wanneer ze worden blootgesteld aan een extern magnetisch veld. Onze gevoeligheid stelde ons in staat om een magnetisatiecurve van een enkel deeltje te meten, die het superparamagnetisme bewees door de afwezigheid van een remanent CD-signaal aan te tonen. Verder toonden we ook aan door een Langevin-functie toe te passen dat het optisch signaal lineair schaalt met de magnetisatie.

Curriculum Vitæ

I was born on 20th July 1990 in Aalen, Germany. I received my Bachelor in Physics at the University of Ulm in 2015, where I also followed a Master program in Physics. During my Master project I joined an exchange program to spend half a year at Southeast University in Nanjing (China), where I used a nanoprinter to develop materials for the study of cellular forces. In January 2018, I joined the single molecule optics group with Prof. dr. Michel Orrit at Leiden University where I developed an optical technique to study the minute circular dichroism effects of plasmonic and magnetic nanoparticles via photothermal imaging. From 2018 to 2021 I assisted in teaching the 1st year's physics Bachelor course 'Elektrische en Magnetische Velden', taught by Prof. dr. Jan van Ruitbenbeek and Dr. Jelmer Wagenaar. From 2020 to 2021 I served the LION institute's council.

List of Publications

1. Martin Dieter Baaske, Nasrin Asgari, Patrick Spaeth, Subhasis Adhikari, Deep Punj, Michel Orrit. *Photothermal Spectro-Microscopy as Benchmark for Optoplasmonic Bio-Detection Assays, The Journal of Physical Chemistry C* ***2021****, 125(45), 25087-25093.*

2. Patrick Spaeth, Subhasis Adhikari, Martin Dieter Baaske, Sergii Pud, Jacco Ton, Michel Orrit. *Photothermal Circular Dichroism of Single Nanoparticles Rejecting Linear Dichroism by Dual Modulation.* ACS Nano **2021**, 15(10), 16277-16285.

3. Subhasis Adhikari, Patrick Spaeth, Ashish Kar, Martin Dieter Baaske, Saumyakanti Khatua, Michel Orrit. *Photothermal Microscopy: Imaging the Optical Absorption of Single Nanoparticles and Single Molecules.* ACS Nano **2020**, 14(12), 16414-16445.

4. Patrick Spaeth, Subhasis Adhikari, Laurent Le, Thomas Jollans, Sergii Pud, Wiebke Albrecht, Thomas Bauer, Martín Caldarola, L Kuipers, Michel Orrit, *Circular Dichroism Measurement of Single Metal Nanoparticles Using Photothermal Imaging.* Nano Letters **2019**, 19(12), 8934-8940.

Acknowledgements

I count myself very lucky for the support and guidance that I have received throughout the four years of my PhD on a professional and personal level.

I would like to start to express my deep gratitude to my supervisor Prof. Michel Orrit who I believe is not only an exceptional and passionate scientist but also a patient teacher. I would like to thank you for your support, for always taking time for me and all the freedom I was given in my research.

Many thanks also go to my second supervisor Prof. Marco Beijersbergen for his critical eye, for the open discussions, and for providing me always with a different view on my progress and results.

I owe a big thank to my daily supervisors Dr. Martin Baaske who helped me from the beginning with all optics related questions and whose ideas considerably contributed to this work, and to Dr. Subhasis Adhikari who helped me with all experiments and data analysis. I also like to thank Dr. Thomas Jollans and Dr. Martín Caldarola who introduced me to optical microscopy and in particular to photothermal imaging and who supervised me in the first months of my PhD. Thanks to Dr. Wiebke Albrecht and Wouter Heyvaert who performed the TEM measurements in chapter 2 and 4 and the associated data analysis and thereby also made a considerable contribution to this work. Thanks to Dr. Kaveh Lahabi for introducing me to the field of magnetism and for helping me with chapter 5.

I like to express my gratefulness to Henriëtte van Leeuwen for carefully handling administrative work and for practising Dutch with me. Thanks to Prof. Gerard Canters who kindly pointed out to me the PhD position in Leiden and without whom I probably wouldn't have come here. My thanks also go to Harmen van der Meer for the excellent and swift mechanical support, to Peter van Veldhuizen, René Overgauw and Dr. Christopher Engelhard for support with the electronics. Thanks to Dr. Wolfgang Löffler who kindly lent to me the photo-elastic modulator, which was an essential piece of equipment in my research. I also would like to thank all the members of MoNOS for a great time in the lab and at the coffee table and for a constructive work environment. In particular, I would like to mention a few group members by name who made a direct contribution to my work: Amin Moradi, Deep Punj, Jacco Ton, Laurent Le, Sergii Pud, Xuxing Lu and Zoran Ristanovic.

Finally, I would like to thank my parents for their constant love and support, you were always there for me. Nancy, thank you for your love and encouragement and for going with me through thick and thin.